

The Pennsylvania State University

The Graduate School

Intercollege Program in Materials Science and Engineering

**PHASE-FIELD STUDY ON FERROELECTRIC OXIDE COMPOSITES AND
HETEROSTRUCTURES**

A Dissertation in

Materials Science and Engineering

by

Tiannan Yang

Submitted in Partial Fulfillment
of the Requirements
for the Degree of

Doctor of Philosophy

May 2018

The dissertation of Tiannan Yang was reviewed and approved* by the following:

Long-Qing Chen
Donald W. Hamer Professor of Materials Science and Engineering
Professor of Engineering Science and Mechanics, and Mathematics
Dissertation Advisor
Chair of Committee

Venkatraman Gopalan
Professor of Materials Science and Engineering

Michael Lanagan
Professor of Engineering Science and Mechanics

Shujun Zhang
Professor of Institute for Superconducting & Electronic Materials, and Australian
Institute of Innovative Materials, University of Wollongong, Australia

Sulin Zhang
Professor of Engineering Science and Mechanics

Suzanne Mohney
Professor of Materials Science and Engineering and Electric Engineering
Chair, Intercollege Graduate Degree Program in Materials Science and
Engineering

*Signatures are on file in the Graduate School

ABSTRACT

Ferroelectric materials are a class of materials possessing a spontaneous electric polarization that is switchable by an external field. A composite approach can either greatly enhance the performance of ferroelectric materials or induce emerging properties and phenomena which expands the range of its applicability. Through microstructure design, performances of ferroelectric composites and heterostructures can be optimized for multiple applications. This dissertation focuses on theoretical understandings of various properties of ferroelectric composites and heterostructures by employing a phase-field model.

Magnetolectric coupling is a phenomenon in which a material exhibits a polarization response to an applied magnetic field. We formulate a phase-field model coupled with constitutive equations to investigate the magnetolectric cross-coupling in magnetic/ferroelectric composites. The model allows us to obtain static piezoelectric, piezomagnetic, dielectric, and magnetolectric properties under a given magnetic or electric field, from the local distributions of polarization, magnetization, and strain in the composites. As an example, effective magnetolectric coupling coefficient, i.e., magnetic-field-induced voltage output (or changes in polarization), of the $\text{CoFe}_2\text{O}_4\text{-BaTiO}_3$ composites is numerically calculated. Influences of the phase connectivity and the phase fraction of the composites on the magnetolectric coupling coefficient are discussed.

We further develop a phase-field model to study the local elastic coupling between magnetic and ferroelectric domains that show one-to-one pattern match. A multiferroic layered heterostructure of $\text{Co}_{0.4}\text{Fe}_{0.6}/\text{BaTiO}_3$ is considered. Kinetics of the local elastic coupling is investigated by simulating the time-dependent electric-field-driven changes in local magnetization/polarization/strain distributions and by comparing the associated velocities of the magnetic and ferroelectric domain walls. It is found that the electric-field-driven magnetic

domain evolution manifests itself as an alternating occurrence of local magnetization rotation and coupled motion of magnetic and ferroelectric domain walls with almost identical velocities.

The electrocaloric effect is a phenomenon in which a dielectric material absorbs or releases heat in response to an applied electric field. An anomalous negative electrocaloric effect in ferroelectric/relaxor composites showing cooling upon applying an electric-field pulse without subsequent heating, is studied by applying a phase-field model. Evolution of domain structure and changes in dipole ordering upon applying the electric field pulse is simulated. It is revealed that coexistence of the normal ferroelectric phase and the ferroelectric relaxor phase in the composite enables stability of two distinct remnant states with ordered and disordered dipoles, respectively. Application of an electric field switches the composite between ordered and disordered states and induces the anomalous electrocaloric effect. The dependence of the electrocaloric cooling temperature and overshooting phenomena on operating temperature is simulated and discussed.

Applying an ultrafast stimulus to a ferroelectric material allows one to explore possible new transient phenomena or new metastable domain patterns that may emerge during the relaxation from its excited state to its original or a new equilibrium state. In this work, we develop a phase-field model for understanding and predicting the dynamical responses of both ferroelectric and ferroelastic domain patterns under ultrafast electrical, thermal, mechanical, and optical stimuli, with advanced numerical algorithms for solving the governing dynamical equations. As an example, the nanoscale and mesoscale domain dynamics of BaTiO₃ crystals under certain types of ultrafast stimuli were investigated. We demonstrate domain dynamics under an external local heat pulse with a combined characteristic of thermal conduction and polarization dynamics under pyroelectric effect. We predict possible deterministic 180° ferroelectric domain switching through the application of ultrashort mechanical stimuli. We further reproduce experimentally observed laser-pulse-induced domain dynamics with distinct

responses determined by both the orientation and the location of the domains. Mesoscale mechanisms of ferroelectric domain and domain wall responses, as well as intrinsic lattice vibrations, are revealed. The theoretical insights on ultrafast domain dynamics will provide useful guidance for manipulating dynamic functionalities of ferroelectric materials.

TABLE OF CONTENTS

List of Figures	viii
List of Tables	xiii
List of Symbols	xiv
Acknowledgements.....	xvii
Chapter 1 Introduction	1
1.1 Brief introduction to ferroelectric oxide composites and heterostructures	1
1.1.1 Ferroelectric oxide.....	1
1.1.2 Ferroelectric composites and heterostructures	5
1.2 Brief introduction to the phase-field model of ferroelectric materials and composites.....	7
1.2.1 Phase-field model of ferroelectric materials.....	7
1.2.2 Phase-field model of ferroelectric composites	11
1.3 Research Objectives	11
1.4 Dissertation structure	12
Chapter 2 Predicting effective magnetoelectric response in magnetic/ferroelectric composites via phase-field modeling	15
2.1 Introduction	15
2.2 Phase-field model for magnetoelectric composites with linear properties.....	16
2.2.1 Phase-field description of magnetoelectric coupling based on constitutive equations.....	17
2.2.2 Simulation setup	21
2.3 Results and discussion	22
2.3.1 Elasticity-mediated polarization response to an external magnetic field	22
2.3.2 Influence of the aspect ratio of inclusions	26
2.3.3 Influence of phase fractions	29
2.3.4 Magnetoelectric coupling in thin film nanocomposites	31
Conclusion	32
Chapter 3 Phase-field study on kinetic properties of elastically coupled magnetic and ferroelectric domains.....	34
3.1 Introduction	34
3.2 Phase-field model.....	35
3.2.1 Phase-field model on the ferroelectric domains	36
3.2.2 Phase-field model on the magnetic domains	38
3.3 Results and discussion	41
3.3.1 Pattern copy between elastically coupled magnetic and ferroelectric domains	41

3.3.2 Electric field-manipulation of magnetic domain pattern	44
3.3.3 Domain evolution kinetics	46
3.4 Conclusion	49
Chapter 4 Phase-field study on an anomalous negative electrocaloric effect in a ferroelectric/relaxor composite	51
4.1 Introduction	51
4.2 Model and simulation method.....	53
4.2.1 Phase-field model on the ferroelectric domain evolution.....	53
4.2.2 Calculation of electrocaloric effect	55
4.2.3 Simulation setup	58
4.3 Results and discussion	59
4.3.1 Ferroelectric properties of the composite	59
4.3.2 Anomalous electrocaloric effect.....	60
4.3.3 Dependence of the electrocaloric effect on temperature and electric field	64
4.4 Conclusion	65
Chapter 5 Phase-field study on inhomogeneous ferroelectric domain dynamics under ultrafast stimuli	67
5.1 Introduction	67
5.1.1 Background	67
5.1.2 Research Objectives	69
5.2 Phase-field model on ultrafast dynamics of ferroelectric materials	71
5.2.1 Polarization dynamics	71
5.2.2 Elastodynamics.....	75
5.3 Domain wall dynamics under ultrafast electric field stimuli	80
5.4 Ultrafast domain dynamics under thermal stimuli	81
5.5 Domain dynamics under ultrafast mechanical stimuli	84
5.6 Domain dynamics of a BaTiO ₃ crystal under an ultrashort laser pulse.....	89
5.7 Conclusion	94
Chapter 6 Conclusions and future work.....	96
6.1 Summary and conclusions.....	96
6.2 Directions for future work.....	99
6.2.1 Microstructure design of piezoelectric composites	99
6.2.2 Phase-field study on ultrafast dynamics in magnetic/ferroelectric heterostructures	101
6.2.3 Phase-field study on ultrafast dynamics in electronic phase transitions	101
Bibliography	103

LIST OF FIGURES

- Figure 1-1. The unit cell of the tetragonal phase ferroelectric BaTiO₃ at room temperature. An electric dipole arises in the unit cell from the spontaneous displacement of the center of the Ba²⁺ and Ti⁴⁺ cations with respect to the center of the O²⁻ anions.2
- Figure 1-2. Schematics of a typical ferroelectric *a/c* multidomain structure in a BaTiO₃ single crystal at room temperature. The right part shows the spatial profile of polarization vector in a region across three ferroelectric domains. The domain structure and spatial distribution of polarization are from phase-field simulations [6]. The left parts are crystal structures with different cation displacements in (top) *a*- and (bottom) *c*-domains.3
- Figure 1-3. (a) Schematics of the energy path during the process of domain switching between energetically degenerate states in a ferroelectric oxide, where the energy barrier is overcome by an applied external field. (b) Typical polarization response in a ferroelectric material upon applying an electric field loop, showing switching of polarization between two energetically degenerate states.....4
- Figure 1-4. Schematics of composites with 0-3, 1-3, and 2-2 connectivities.6
- Figure 2-1. (a) Schematic illustration of the chosen simulation zone of the phase-field model, where a cuboid CoFe₂O₄ inclusion with a dimension of $a \times a \times c$ is embedded in a BaTiO₃ matrix. The composite is described by periodically aligning CoFe₂O₄ particles with a uniform separation distance d within all three directions. Composites of different phase connectivities including (b) 2-2, (c) 0-3 and (d) 1-3 types are obtained by varying the aspect ratios $r = c/a$ of the CoFe₂O₄ inclusions. The CoFe₂O₄ and BaTiO₃ phases are assumed to be intimately contacted at their interface region, with no gas phase (porosity) incorporated in the model.17
- Figure 2-2. Equilibrium distributions of the lateral strain ε_2 , longitudinal strain ε_3 , and the longitudinal polarization P_3 responsive to a longitudinally applied magnetic field $H_3 = 100 \text{ A/m}$, in composites of (a) 0-3 ($r = 1$), (b) 2-2 ($r = 0.02$) and (c) 1-3 ($r = 10$) connectivities, with the CoFe₂O₄ phase fraction V_f taken as 0.5. For clarity, only 1/8 (half length in each dimension) of one building block is shown. Dashed lines indicate the CoFe₂O₄/BaTiO₃ phase boundaries and the partition of lateral and longitudinal regions in the BaTiO₃ phase.24
- Figure 2-3. Effective (a) magnetoelectric coefficients (enlarged scale of the red rectangle part shown as inset), (b) magnetoelectric voltage coefficients (relative dielectric permittivity shown as inset), (c) piezoelectric coefficients and (d) piezomagnetic coefficients of the CoFe₂O₄/BaTiO₃ composites as a function of the aspect ratio r . The volume fraction of the CoFe₂O₄ phase is set to be 0.5.....27
- Figure 2-4. Effective (a) magnetoelectric coefficients, (c) relative dielectric permittivity and (d) magnetoelectric voltage coefficients of the CoFe₂O₄/BaTiO₃ composite with different aspect ratios r as a function of the phase-fraction V_f . (b) $V_f^m \varepsilon_1$ of the

- composite with different aspect ratios r upon applying a magnetic field $H_3^{\text{ext}} = 100\text{A/m}$, as a function of the phase-fraction V_f30
- Figure 2-5. 1-3 type $\text{CoFe}_2\text{O}_4/\text{BaTiO}_3$ composites with thin film and island nanostructures show an enhanced magnetoelectric coupling property compared with 1-3 bulk composites with the same phase fraction. (a)~(c) Schematics of 1-3 type $\text{CoFe}_2\text{O}_4/\text{BaTiO}_3$ (a) bulk composites and composites with (b) thin film nanostructure and (c) island nanostructure. (d) Equilibrium polarization response P_3 as a function of the aspect ratio $r = h/a$ of the CoFe_2O_4 rods in 1-3 type island nanostructure and thin film nanostructure, respectively, compared with the polarization response in a 1-3 bulk composite, on applying an external magnetic field. Volume fraction of the CoFe_2O_4 phase is fixed at $V_f = 0.35$ for all composite structures.32
- Figure 3-1. (a) Schematics of the simulation system in Step 1 of the phase-field model: determining ferroelectric domain structures in a fully electroded BaTiO_3 crystal substrate with uncompensated bound charges (see the circle) (b) Step 2: determining magnetic domain structures in the CoFe film in a film-substrate system. The simulation zone is marked by dashed lines, where a unique displacement boundary condition relating to polarization distribution (Equation 3-10) is applied at the bottom of the substrate at $x_3 = -h_s$36
- Figure 3-2. (a) Initial ferroelectric domain configuration of the BaTiO_3 substrate and magnetic domain configuration of the as grown CoFe film. The arrows indicate the directions of local polarization/magnetization vectors. Domain definitions and the corresponding polarizations/magnetizations: a_1 : $(P_1, 0, 0)$ or $(m_1, 0, 0)$; a_2 : $(0, P_2, 0)$ or $(0, m_2, 0)$; c : $(0, 0, P_3)$ or $(0, 0, m_3)$. (b) Corresponding distributions of the in-plane strain difference $\varepsilon_{11} - \varepsilon_{22}$ at the top surfaces of the original BaTiO_3 substrate and the CoFe film. The dashed lines indicate boundaries of the ferroelectric domains. The double-headed arrows indicate the elongated in-plane axes.42
- Figure 3-3. (a) Polar plot of the remnant magnetization M_R in regions on top of ferroelectric a_1 domains and regions on top of ferroelectric a_2 domains, respectively, on applying a magnetic field along in-plane direction. (b) (Left column) average magnetization response on applying a magnetic field loop along in-plane directions with angles $\theta = 0^\circ$, $\theta = 45^\circ$, and $\theta = -45^\circ$ with respect to the x_1 axis, respectively, and (right column) corresponding remnant magnetization configurations.44
- Figure 3-4. (a) Ferroelectric domain configuration of the BaTiO_3 substrate and magnetic domain configuration of the CoFe film upon increasing E_3 from 0 (first column) to 600kV/m (second column), followed by reducing E_3 to 240kV/m (third column) and then to 0 (fourth column). The arrows indicate the directions of local polarization/magnetization vectors. Domain definitions and the corresponding polarizations/magnetizations: a_1 : $(P_1, 0, 0)$ or $(m_1, 0, 0)$; a_2 : $(0, P_2, 0)$ or $(0, m_2, 0)$; c : $(0, 0, P_3)$ or $(0, 0, m_3)$. Corresponding distributions of the in-plane strain difference $\varepsilon_{11} - \varepsilon_{22}$ at (b) the top surfaces of the original BaTiO_3 substrate and (c) the CoFe film. The dashed lines indicate boundaries of the ferroelectric domains. The double-headed arrows indicate the elongated in-plane axes.45

- Figure 3-5. Magnetic and ferroelectric domain structures at (a) $E_3 = 280\text{kV/m}$ and (b) $E_3 = 110\text{kV/m}$ in a downhill electric-field cycle. (Right columns) close-up vector plots of the polarization and magnetization configuration within the selected areas; the white dashed lines and the hollow arrows indicate the domain wall and the direction of the domain wall motion, respectively; the white solid circles indicate the regions undergoing magnetization rotation.47
- Figure 3-6. (a) (Top) time sequence of the applied out-of-plane electric field E_3 , and the velocities of (middle) ferroelectric and (bottom) magnetic domain wall motion, in ferroelectric a_1/c domain and mixed a_1 and a_1/a_2 magnetic domain configurations, respectively. The regions encircled by dash-dotted lines indicate the coupled domain wall motion, and the background colors indicate the dominant ferroelectric or magnetic domains at various stages. (b) (Top) polarization and (bottom) magnetization configurations across the selected ferroelectric and magnetic domain walls, respectively, at $E_3 = 240\text{kV/m}$ in the downhill cycle. The dashed lines indicate the domain wall positions.49
- Figure 4-1. Dipole ordering and electrocaloric heat upon applying and removing an electric field for the normal electrocaloric effect, negative electrocaloric effect, and the anomalous negative electrocaloric effect.52
- Figure 4-2. P-E loops of pure P(VDF-TrFE) at temperatures $15^\circ\text{C} \leq T \leq 70^\circ\text{C}$, from the phase-field simulation.55
- Figure 4-3. Spatial distribution of the two-phase structure of the P(VDF-TrFE)/P(VDF-TrFE-CFE) composite with a 50/50vol% phase fraction. P(VDF-TrFE) is shown by the white regions, while P(VDF-TrFE-CFE) is shown by the black regions.59
- Figure 4-4. Simulated P-E loops of the P(VDF-TrFE)/P(VDF-TrFE-CFE) 50/50vol% with a $E = 100\text{MV/m}$ poling field, at (a) 15°C , (b) 25°C , (c) 40°C , and (d) 70°C , respectively, showing the transition from a normal ferroelectric material with strong remnant polarization and coercive field in the P-E loop, to a relaxor (or dielectric material) with smaller hysteresis upon increasing the temperature.60
- Figure 4-5. Simulated spatial map of the polarization vectors in the room temperature P(VDF-TrFE)/P(VDF-TrFE-CFE) 50/50vol% composite, at remnant states (top panel) after poling with $E_3 = 100\text{MV/m}$, and (bottom panel) after subsequent depoling with $E_3 = -35\text{MV/m}$, respectively. The light and dark backgrounds indicate regions of the P(VDF-TrFE) and P(VDF-TrFE-CFE) phases, respectively.61
- Figure 4-6. Simulated probability distribution of the orientation θ of polarization vectors inside the P(VDF-TrFE-CFE) relaxor phase, (a) at remnant states after poling with $E_3 = 100\text{MV/m}$, and after subsequent depoling with (b) $E_3 = -35\text{MV/m}$ and (c) $E_3 = -40\text{MV/m}$, respectively, of the room temperature P(VDF-TrFE)/P(VDF-TrFE-CFE) 50/50vol% composite.62
- Figure 4-7. Simulated electrocaloric-induced cooling temperature ΔT in the P(VDF-TrFE)/P(VDF-TrFE-CFE) 50/50vol% composite as a function of the applied depoling field, at different operating temperatures $T = 25^\circ\text{C}$, 30°C , and 40°C . With

- an increasing temperature, the overshooting threshold field decreases, resulting in a decreased maximum cooling temperature.....65
- Figure 5-1. Experimentally measured oscillations of local surface strain ε_{33} in c -type domains (top-left plot) with an out-of-plane polarization direction (indicated by the blue arrow) and in a -type domains (top-right plot) with an in-plane polarization direction (indicated by the red arrow), upon applying an ultrashort laser pulse to the surface of a BaTiO_3 crystal. The figure is adapted from Ref. [130].68
- Figure 5-2. Schematic illustration of dielectric responses of a solid subject at different frequencies. The figure is adapted from [155].70
- Figure 5-3. Numerical solution to the elastodynamics equation with our own solver based on the Fourier-spectral method (Equation 5-18), as compared with the elastodynamic solver in COMSOL Multiphysics[®] based on finite-element method (a) Initial displacement field u_2 , set as a Gaussian function of distance to the center of the simulation region. Initial velocity is set as 0. (b) Displacement field along the central line (indicated by the dashed line in (a)) at different times.....79
- Figure 5-4. Dynamics of ferroelectric domain wall and vortex upon applying an AC electric field. (a) A multi-domain structure in BaTiO_3 with 90° domain walls and (b) the change in the width of the domain stripe responsive to an AC electric field. (c) A vortex domain structure in a BaTiO_3 island and (d) the displacement of the vortex core responsive to an AC electric field.81
- Figure 5-5. Ferroelectric domain dynamics upon applying a local heat pulse. (a) At $t=0$, a heat pulse is applied in a circular region (in orange) in a BaTiO_3 single domain, which raises the local temperature instantaneously by $\Delta T=100\text{K}$. (b) The spatial-temporal map of the polarization change ΔP_1 along the vertical line across the center of the heated region (as indicated by the dashed line in (a)), after applying the laser pulse. The vertical axis indicates the distance Δx_3 from the center of the heated region. (c) Temperature T and (d) polarization P_1 in the first 2.5ns after heating, at different points below the heated region (along the dashed line in (a)), at distances $\Delta x_3=0$ (Point A), $\Delta x_3=0.5\mu\text{m}$ (Point B), $\Delta x_3=1.0\mu\text{m}$ (Point C), $\Delta x_3=1.5\mu\text{m}$ (Point D), $\Delta x_3=2.0\mu\text{m}$ (Point E), respectively.82
- Figure 5-6. Evolution of (upper row) the strain field and (lower row) ferroelectric domain structure after applying a local body force with $f_{V3}=2.5\text{nN/nm}^3$ and a duration of 10ps within a circular region (with radius $R=320\text{nm}$) in a ferroelectric a_1 single domain. Local 180° domain switching is observed.....84
- Figure 5-7. The profile of polarization \mathbf{P} at time delay $t=0.5\text{ns}$, and the profile of strain change $\Delta\varepsilon_{33}$, $\Delta\varepsilon_{11}$, and $\Delta\varepsilon_{13}$ at time delay $t=0.25\text{ns}$, after applying the external force....86
- Figure 5-8. Time sequence of (a) rotation angle of polarization and (b) strain change $\Delta\varepsilon_{13}$ at Point D (as indicated in Fig. 5-7), after applying the external force.88

- Figure 5-9. (First panel) schematics of domain structure in the subsurface region. (Other panels) simulated strain map $\Delta\epsilon_{33}$ at time delays $t=0\text{ns}$, $t=0.7\text{ns}$, and $t=3.2\text{ns}$, respectively, in the subsurface region.89
- Figure 5-10. (a) Evolution of polarization change ΔP_3 in subsurface c -domain from the dynamical phase-field simulation. (b) Evolution of strain change $\Delta\epsilon_{33}$ in subsurface a - and c -domains from experimental measurement (dots) [130] and dynamical phase-field simulation (solid lines).91
- Figure 5-11. (First panel) schematics of domain structure in the surface region. The a/c domain wall (DW) moves towards a domain, while polarization inside a domain rotates towards the out-of-plane direction. (Other panels) simulated strain map $\Delta\epsilon_{33}$ at time delays $t=0\text{ns}$, $t=0.7\text{ns}$, and $t=3.2\text{ns}$, respectively, in the surface region.92
- Figure 5-12. (a) Temporal evolution of displacement Δr_{wall} of the surface a/c domain walls and rotation angle $\Delta\theta_p$ of the polarization vector in surface a domains from the dynamical phase-field simulation. (b) Evolution of strain change $\Delta\epsilon_{33}$ in the surface a - and c -domains from experimental measurement (dots) [130] and dynamical phase-field simulation (solid lines).93
- Figure 6-1. Comparison of the structure of piezoelectric composites (left panel) with ferroelectric oxide particles in a dielectric polymer matrix, and (right panel) with a porous ferroelectric ceramic forming interconnected networks in a dielectric polymer matrix. The silver phases indicate the ferroelectric oxide, while the rest of the space in the composite is filled with the polymer phase which is not drawn for clarity. The geometry of the network structure is generated with a grain growth simulation code.100

LIST OF TABLES

Table 2-1. Material constants of CoFe_2O_4 and BaTiO_3	18
Table 4-1. Material constants of P(VDF-TrFE) and P(VDF-TrFE-CFE).	54
Table 5-1. Material constants of BaTiO_3 in the dynamical phase-field model	73

LIST OF SYMBOLS

Symbols	Physical Quantities
$a_i, a_{ij}, a_{ijk},$ and a_{ijkl}	Landau energy coefficients for polarization
B_i	Magnetic induction
c_{ijkl} or c_{IJ}	Elastic stiffness tensor
C_P	Heat capacity at constant pressure
D_i	Dielectric displacement
E_i	Electric field
e_{ijk} or e_{iJ}	Piezoelectric stress coefficient
E_C	Coercive electric field
E_i^d	Depolarization field
E_i^{ext}	External electric field
F	Free energy
f	Volumetric free energy density
f_{int}	Volumetric internal energy density
f_{Pi}	Driving force of polarization evolution
f_{vi}	Volumetric external body force density
g_{ijkl} or g_{IJ}	Gradient energy coefficients for polarization
H_i	Magnetic field
H_i^d	Demagnetization (or demagnetizing) field
H_i^{ext}	External magnetic field
h_f	Thickness of film
h_s	Thickness of substrate
$H_{\text{Eff}i}$	Effective field of magnetization evolution
I	Imaginary unit
l_i	Linear size of a system
L_{Pij}	Kinetic coefficient of polarization evolution
M_i	Magnetization
m_i	Reduced magnetization
M_{Ri}	Remnant magnetization

M_S	Saturation magnetization
n_i	Number of grid points in each direction
P_i	Polarization
P_{Ri}	Remnant polarization
P_S	Spontaneous polarization
Q	Heat
Q_{irr}	Heat produced during irreversible processes
Q_{ijkl} or Q_{IJ}	Electrostrictive coefficients
q_i	Position in Fourier space
q_{ijk} or q_{ij}	Piezomagnetic coefficient
r	Aspect ratio of a particle
S	Volumetric entropy density
s_{ijkl} or s_{IJ}	Elastic compliance tensor
T	Temperature
t	Time
T_C	Curie-Weiss Temperature
u_i	Displacement
V	Volume
v_i	Velocity
x_i	Position
α_{ij}	Magnetoelectric coupling coefficient
α_{Dij}	Mass damping coefficient
α_{Eij}	Magnetoelectric voltage coefficient
α_L	Linear thermal expansion coefficient
α_M	Damping constant of magnetization evolution
β_D	Stiffness damping coefficient
γ_0	Gyromagnetic ratio of electrons
γ_{Pij}	Effective mass coefficient of polarization
Δl_i or Δl	Linear size of a grid point
$\delta \epsilon_{ij}$ or $\delta \epsilon_I$	Heterogeneous strain

ε_{ij} or ε_I	Strain
ε_{ij}^0 or ε_I^0	Eigenstrain
η	Local concentration of a phase
κ_{ij}	Dielectric permittivity
κ_0	Vacuum permittivity
κ_b	Relative background dielectric permittivity
κ_{rij}	Relative dielectric permittivity
$\lambda_S, \lambda_{100},$ or λ_{111}	Saturation magnetostriction
μ_{ij}	Magnetic permeability
μ_0	Vacuum permeability
μ_{Pij}	Damping coefficient of polarization
μ_{rij}	Relative magnetic permeability
ρ	Density
σ_{ij} or σ_I	Stress
τ	Time per evolution step

In the table above, subscripts $i,j,k,l = 1,2,3$ are indices for vectors and tensors, etc. in an x_1 - x_2 - x_3 3-dimensional Cartesian coordinate; subscripts $I,J = 1,2,3,4,5,6$ are indices of tensors following a Voigt notation.

ACKNOWLEDGEMENTS

First, I would like to thank my research advisor, Dr. Long-Qing Chen, for the advice and help he provided me. His excellent guidance, kind encouragement, and support on my research have been invaluable to me. I deeply admire his enthusiasm for science, amazing knowledge of materials modeling, and rigorous attitude towards scientific research, which motivate my research and will forever benefit me in my future career working with science. He also opened for me vast opportunities to collaborate with other scientists and researchers around the world. Without his help, none of my successes would have been possible.

I would like to thank Dr. Venkatraman Gopalan, Dr. Michael Lanagan, Dr. Shujun Zhang, and Dr. Sulin Zhang, for serving on my Ph.D. committees and providing deep discussions and insightful suggestions on my research. I'm also grateful to our collaborators, Dr. Ying-Hao Chu at National Chiao Tung University, Dr. Venkatraman Gopalan at Penn State, Dr. Ce-Wen Nan at Tsinghua University, Dr. Sang Ho Oh at Pohang University of Science and Technology, Dr. Dwight Viehland at Virginia Tech, Dr. Qing Wang at Penn State, and Dr. Qiming Zhang at Penn State, that provide great opportunities for me to apply my computation models to their latest cutting-edge experimental findings.

I would like to thank all my labmates for their kind help and encouragement. I would especially like to thank Dr. Jiamian Hu for insightful ideas, detailed suggestions and close help in my research; Dr. Ye Cao, Dr. Yijia Gu, and Dr. Fei Xue for deep discussions that introduced to me the phase-field model and knowledge of ferroelectric materials; Dr. Jason Britson and Dr. Tae-Wook Heo for kindly providing modeling tools and helping with understanding and developing computation models and algorithms. I would also like to thank Dr. Jianjun Wang, Dr. Houbing Huang, Dr. Linyun Liang, Dr. Liang Hong, Dr. Lei Chen, Dr. Fei Li, Dr. Zijian Hong,

Mr. Yanzhou Ji, Ms. Wenting Xing, Mr. Xiaoxing Cheng, and many others for their generous help and encouragement throughout my research work.

Last and importantly, I would like to give my sincere thanks to my amazing parents, Mr. Guoqing Yang and Mrs. Guohua Zhang, for their love and support.

Financial support for this research was through National Science Foundation, Division of Materials Research, under Award # DMR-1006541 and # DMR-1410714. Computational support was through the Penn State Institute for CyberScience and calculations were performed on the Lion-X, Cyberstar, and ACI servers.

Chapter 1

Introduction

1.1 Brief introduction to ferroelectric oxide composites and heterostructures

1.1.1 Ferroelectric oxide

Ferroelectric materials are a class of materials possessing a spontaneous electric polarization that can be reoriented by an external electric field [1-3]. The word ferro- originates from the analogy to ferromagnetic material with similar behaviors of spontaneous orders and hysteresis responses to external fields (discussed below). Dating back to 1920, Rochelle salt is the first ferroelectric material reported [4]. Later discovery of ferroelectricity in multiple materials including barium titanate (BaTiO_3), lead titanate (PbTiO_3), etc., belonging to a class of perovskite oxides, have long attracted major experimental and theoretical interest due to their improved properties and design flexibility.

Take BaTiO_3 for example, which is one of the first known ferroelectric perovskite oxides, dating back to 1940s [5]. It shows a typical perovskite structure with a cubic lattice at high temperatures. Upon cooling, the crystal lattice undergoes a spontaneous deformation at $T \sim 400\text{K}$ to a tetragonal lattice with elongated c axes, in which Ti^{4+} cations are displaced from the cubic center of the unit cell and the center of the octahedron formed by neighboring O^{2-} anions, as shown by the room temperature crystal structure of BaTiO_3 in Fig. 1-1. The displaced cation center and anion center generates an electric dipole in the unit cell, and ordering of the dipoles at each unit cell in the crystal further results in a net polarization P_S in the material, which is called a spontaneous polarization. The transformation temperature between the high-temperature cubic

phase (paraelectric phase) and the low-temperature phase with spontaneous polarization (ferroelectric phase), T_C , is called the Curie temperature.

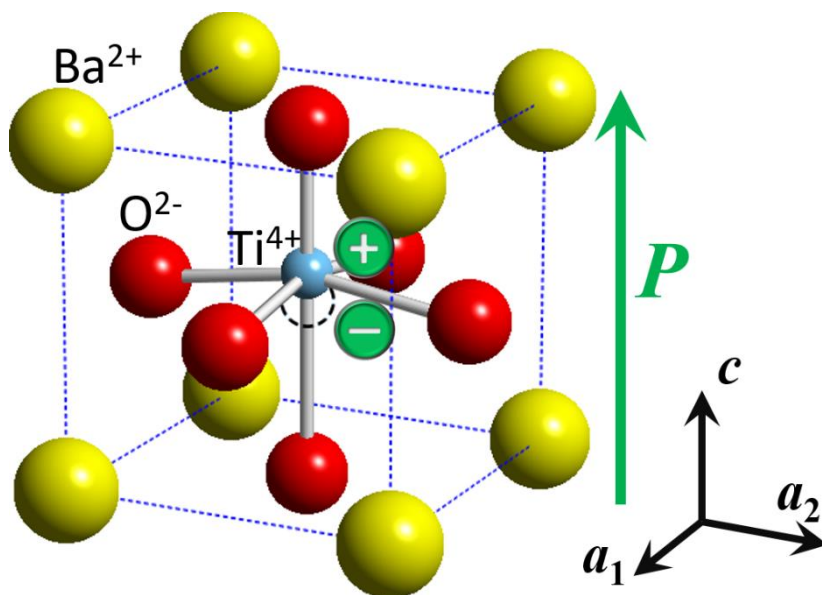


Figure 1-1. The unit cell of the tetragonal phase ferroelectric BaTiO₃ at room temperature. An electric dipole arises in the unit cell from the spontaneous displacement of the center of the Ba²⁺ and Ti⁴⁺ cations with respect to the center of the O²⁻ anions.

Formation of ferroelectric domains is an important phenomenon which plays a critical role in various properties of ferroelectric materials. For example, upon cooling down a BaTiO₃ crystal from high temperature, a multidomain structure of tetragonal phases are naturally formed, without forming a grain boundary. Figure 1-2 shows a typical ferroelectric *a/c* multidomain structure in a BaTiO₃ crystal. The existence of 6 possible dipole orientations in a unit cell, i.e., along a_1^+ , a_1^- , a_2^+ , a_2^- , c^+ , and c^- , which are symmetry-related in the high-temperature cubic phase, enables spontaneous formation of local polarization along all 6 directions.

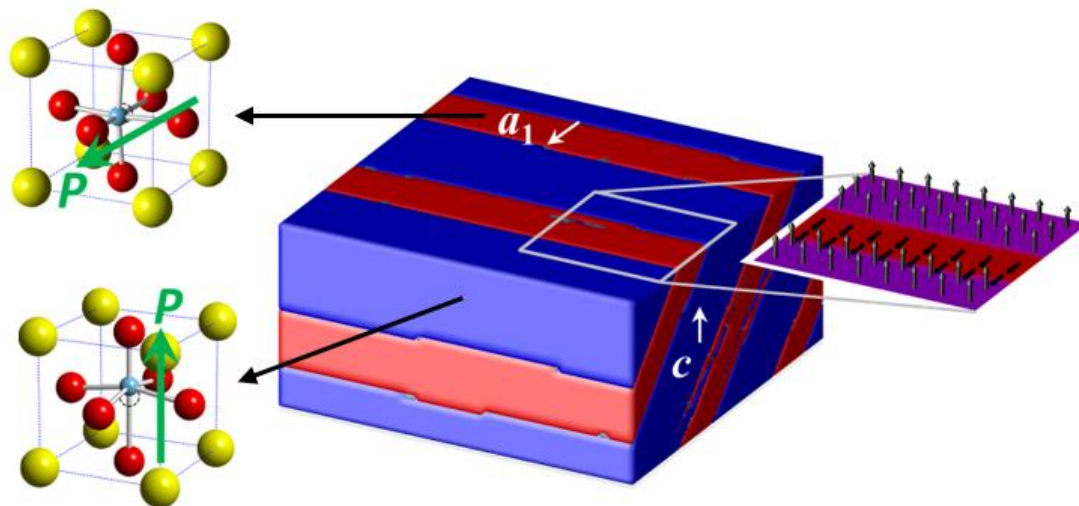


Figure 1-2. Schematics of a typical ferroelectric a/c multidomain structure in a BaTiO_3 single crystal at room temperature. The right part shows the spatial profile of polarization vector in a region across three ferroelectric domains. The domain structure and spatial distribution of polarization are from phase-field simulations [6]. The left parts are crystal structures with different cation displacements in (top) a - and (bottom) c -domains.

A continuous region with homogeneous electric dipole orientation (or polarization) is called a ferroelectric domain. Regions between two adjacent domains are called domain walls, across which the local polarization undergoes a spatial variation from the spontaneous polarization in one domain to that in the other. Domain walls are typically a few unit cells thick in tetragonal domains in BaTiO_3 at room temperatures. Such multi-domain structures are usually stabilized by electrostatic, elastic, or chemical fields, etc.

The polarization in ferroelectric materials can be switched between different orientations through applying external fields, which is called domain switching. According to the symmetry of high-temperature ferroelectric phase, there exists symmetry-related, energetically degenerate states which are stabilized at energy minima with respect to structural change (or polarization). As schematically illustrated in Fig. 1-3 (a), on applying an external field (e.g., an electric field) to

overcome a certain energy barrier between two energy minima, polarization is switched from one stable state to another.

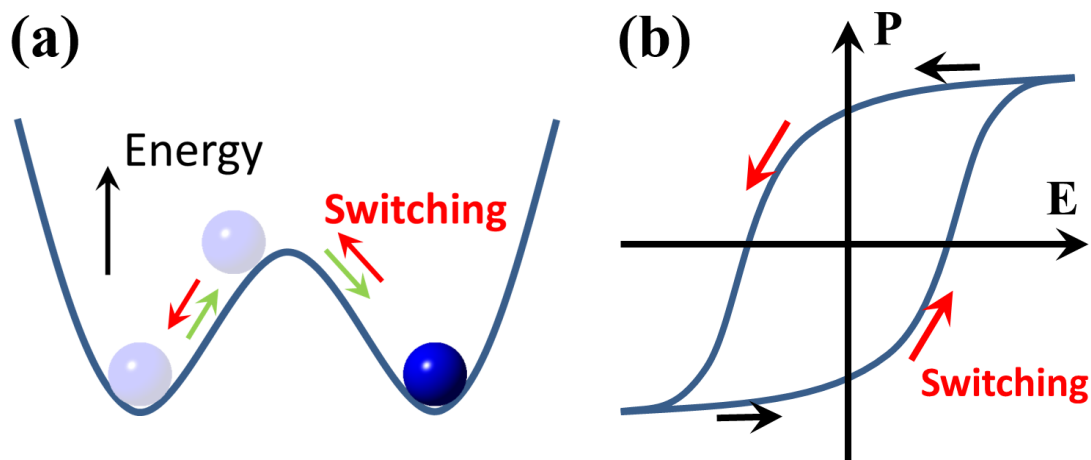


Figure 1-3. (a) Schematics of the energy path during the process of domain switching between energetically degenerate states in a ferroelectric oxide, where the energy barrier is overcome by an applied external field. (b) Typical polarization response in a ferroelectric material upon applying an electric field loop, showing switching of polarization between two energetically degenerate states.

Upon applying an external electric field loop, typical polarization response in a normal ferroelectric material demonstrates a hysteresis loop (called a P-E loop) with two polarization switching processes between two energetically degenerate stable states in one cycle, as shown by the schematics in Fig. 1-3 (b). Similar to an M-H loop in magnetic materials, in the P-E loop, the equilibrium polarization upon decreasing the electric field to zero (i.e., no external field) is called the remnant polarization (P_R), and the external electric field under which polarization reduces to zero is called the coercive field (E_C).

Other than to electric field, the ferroelectric polarization also shows responses to many other external stimuli, including thermal, mechanical, magnetic, and optical stimuli [7], originating from electro-mechanical, electro-thermal, and magnetoelectric couplings, etc. For

example, formation or switching of spontaneous polarization in ferroelectric materials is accompanied by a deformation of the crystal lattice, which is called electrostriction, and thus polarization can be altered or switched upon an external strain or stress, as a converse effect of such electro-mechanical coupling. Due to their ability to respond to multiple fields, ferroelectric materials found applications in many technologies, e.g., non-volatile memories, sensors, transducers, energy-efficient cooling devices, etc. [8-14].

1.1.2 Ferroelectric composites and heterostructures

A composite approach, by which two or more materials are combined within specific microstructures, explores the combination of properties of constituent materials, and can greatly improve the material performance and design flexibility as compared with single phase materials, and expand the range of applicability of materials.

The resultant properties of a composite can be categorized into sum properties, combination properties, and product properties [15]. The sum property manifests itself as the average of the property of the constituent phases, e.g. density, heat capacity, etc. Combination properties follow more complicated mixing rules, which is dependent on the microstructure of the composite. For example, in a ferroelectric/ferroelectric two-phase composite, properties including elastic stiffness, dielectric permittivity, piezoelectric coefficient, and spontaneous polarization, etc., are all combination properties which can be tuned through manipulating the microstructure. Product property is considered as a product of two other properties in different constituent phases, e.g., magnetoelectric coupling property emerging in a composite with piezoelectric and magnetostrictive phases.

Microstructural factors including phase connectivity, phase fraction, scales of microstructure, phase interface quality, etc., would strongly affect properties and performances of

a composite. As shown in Fig. 1-4, a two-phase composite may possess a 0-3 connectivity with secondary phase (0-dimensional) particles distributed in a (3-dimensional) matrix or a 1-3 connectivity with secondary phase (1-dimensional) rods distributed in a (3-dimensional) matrix, or a 2-2 connectivity with (2-dimensional) layered structures [16]. The different connectivity would result in distinct performances of the composite, suitable for different applications. Through microstructure and interface design, the performance of a composite can be optimized for specific applications.

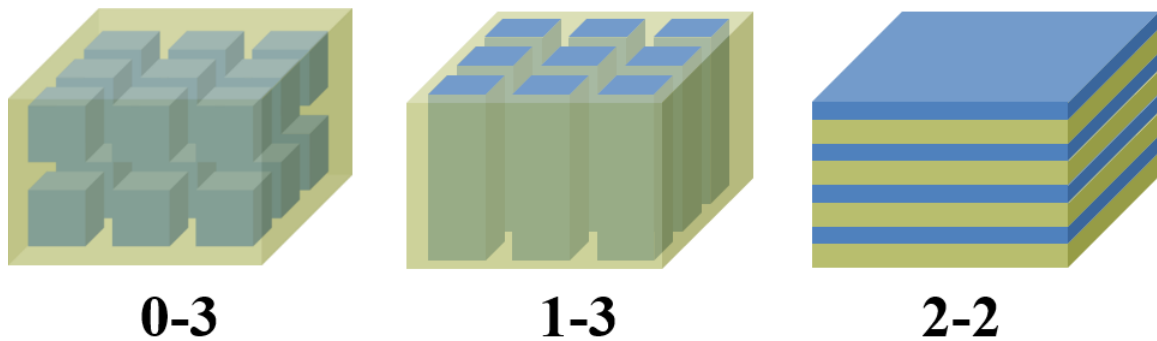


Figure 1-4. Schematics of composites with 0-3, 1-3, and 2-2 connectivities.

Ferroelectric composites and heterostructures have attracted great interest in past decades and seen improving performance for multifunctional applications including sensors, transducers, energy storage, etc. For example, magnetic/ferroelectric multiferroic heterostructures show magnetoelectric cross-coupling as an emerging property, which can be more than a thousand times greater than that in the known single-phase magnetoelectrics [17-19]. Composites combining ferroelectric oxides with polymer materials offer enhanced piezoelectric performances for application in transducers, with improved flexibility and acoustic impedances [16, 20, 21]. Theoretical understandings and predictions of the properties can provide useful guidance in tuning the functionalities of ferroelectric composites and heterostructures.

1.2 Brief introduction to the phase-field model of ferroelectric materials and composites

Phase-field model is a powerful tool for studying microstructure evolution during phase transformations, chemical reaction, transport, etc., and predicting properties of materials with arbitrary microstructures [22-25]. Instead of explicit treatment of interfaces, the phase-field method employs a diffuse interface description, i.e., using a phase field $\eta(\mathbf{x})$ (\mathbf{x} is the spatial position) representing the concentration of a phase (or domain, etc.) which can change continuously across the interface. The temporal evolution of the microstructure is modeled by solving partial differential equations describing the kinetics of the phase field, which are called governing equations of the phase-field model. When combined with the Landau theory describing phase transformations, the corresponding order parameters are adopted as the phase field in the model.

The phase-field model is a numerical model which more easily considers spatial inhomogeneity of a system with an evolving microstructure as compared with analytical models similarly based on Landau theory. It is also a mesoscale model which allows description of nanoscale structures including phase interfaces, grain boundaries, and ferroelectric and magnetic domain walls yet can also be applied to systems with much larger sizes, e.g., hundred microns scale.

1.2.1 Phase-field model of ferroelectric materials

In the phase-field model of ferroelectric materials, the evolution of the ferroelectric polarization field $\mathbf{P}(\mathbf{x})$ is governed by the time-dependent Ginzburg-Landau equation [24],

$$\frac{\partial P_i}{\partial t} = -L_{Pij} \frac{\delta F(\mathbf{P})}{\delta P_j} \quad (1-1)$$

where t is time, F is the total free energy of the system as a functional of the polarization field, and \mathbf{L}_p is the kinetic coefficient of polarization evolution related to domain wall mobility. Subscripts $i,j,k,l,m = 1,2,3$ are indices for components of vectors and tensors in an $x_1-x_2-x_3$ 3-dimensional Cartesian coordinate, and summation convention over repeated subscript indices $i,j,k,l,m = 1,2,3$ are employed herein and throughout the whole dissertation. $\delta F(\mathbf{P})/\delta \mathbf{P}$ here indicates a variational derivative of the total free energy with respect to the polarization order parameter; $\mathbf{f}_p = -\delta F(\mathbf{P})/\delta \mathbf{P}$ is called the driving force of polarization evolution. Equation 1-1 is solved using a semi-implicit Fourier spectral method [26] in this dissertation.

The total free energy $F(\mathbf{P})$ includes the following contributions [24, 27]:

- Landau free energy F_{Landau} ;
- Polarization gradient energy F_{gradient} ;
- Electrostatic energy F_{electric} ;
- Elastic energy F_{elastic} ;

as below,

$$F = F_{\text{Landau}} + F_{\text{gradient}} + F_{\text{electric}} + F_{\text{elastic}} \quad (1-2)$$

Following the Landau theory of phase transformations, the ferroelectric Landau free energy F_{Landau} is a polynomial of the order parameter \mathbf{P} . For example, the 8th-order polynomial form is written as [24]

$$\begin{aligned} F_{\text{Landau}} = \int \bigg[& a_1 (P_1^2 + P_2^2 + P_3^2) + a_{11} (P_1^4 + P_2^4 + P_3^4) + a_{12} (P_1^2 P_2^2 + P_1^2 P_3^2 + P_2^2 P_3^2) \\ & + a_{111} (P_1^6 + P_2^6 + P_3^6) + a_{112} (P_1^4 P_2^2 + P_1^4 P_3^2 + P_2^4 P_1^2 + P_2^4 P_3^2 + P_3^4 P_1^2 + P_3^4 P_2^2) \\ & + a_{123} P_1^2 P_2^2 P_3^2 + a_{1111} (P_1^8 + P_2^8 + P_3^8) \\ & + a_{1112} (P_1^6 P_2^2 + P_1^6 P_3^2 + P_2^6 P_1^2 + P_2^6 P_3^2 + P_3^6 P_1^2 + P_3^6 P_2^2) \\ & + a_{1122} (P_1^4 P_2^4 + P_1^4 P_3^4 + P_2^4 P_3^4) + a_{1123} (P_1^4 P_2^2 P_3^2 + P_2^4 P_1^2 P_3^2 + P_3^4 P_1^2 P_2^2) \bigg] d\mathbf{x}^3 \end{aligned} \quad (1-3)$$

where higher-order terms are neglected. a_i , a_{ij} , a_{ijk} , and a_{ijkl} are 2nd-, 4th-, 6th-, and 8th-order Landau coefficients of a material, respectively, which can be constructed from fitting experimental measurements on ferroelectric properties, or from ab initio calculations. A similar 6th- (or 4th-) order polynomial form is also employed in certain ferroelectric systems with 8th- (or 6th- and 8th-) order terms further neglected. On the other hand, the Landau free energy of a linear dielectric (or paraelectric) material can be written as a 2nd-order polynomial (see Chapter 2).

The ferroelectric gradient energy F_{gradient} is given by [27]

$$\begin{aligned}
F_{\text{gradient}} = \int & \left[\frac{1}{2} g_{11} \left(\left(\frac{\partial P_1}{\partial x_1} \right)^2 + \left(\frac{\partial P_2}{\partial x_2} \right)^2 + \left(\frac{\partial P_3}{\partial x_3} \right)^2 \right) + g_{12} \left(\frac{\partial P_1}{\partial x_1} \frac{\partial P_2}{\partial x_2} + \frac{\partial P_1}{\partial x_1} \frac{\partial P_3}{\partial x_3} + \frac{\partial P_2}{\partial x_2} \frac{\partial P_3}{\partial x_3} \right) \right. \\
& + \frac{1}{2} g_{44} \left(\left(\frac{\partial P_1}{\partial x_2} + \frac{\partial P_2}{\partial x_1} \right)^2 + \left(\frac{\partial P_1}{\partial x_3} + \frac{\partial P_3}{\partial x_1} \right)^2 + \left(\frac{\partial P_2}{\partial x_3} + \frac{\partial P_3}{\partial x_2} \right)^2 \right) \\
& \left. + \frac{1}{2} g_{44m} \left(\left(\frac{\partial P_1}{\partial x_2} - \frac{\partial P_2}{\partial x_1} \right)^2 + \left(\frac{\partial P_1}{\partial x_3} - \frac{\partial P_3}{\partial x_1} \right)^2 + \left(\frac{\partial P_2}{\partial x_3} - \frac{\partial P_3}{\partial x_2} \right)^2 \right) \right] d\mathbf{x}^3
\end{aligned} \tag{1-4}$$

g_{11} , g_{44} , and g_{44m} are gradient energy coefficients of a material, related to properties of the ferroelectric domain walls including the thickness, energy, and anisotropy, etc.

The electrostatic energy F_{electric} is given by

$$F_{\text{electric}} = \int \left(-P_i E_i^{\text{ext}} + \frac{1}{2} \kappa_0 \kappa_b E_i^{d2} \right) d\mathbf{x}^3 \tag{1-5}$$

where \mathbf{E}^{ext} and \mathbf{E}^d are the external electric field and depolarization field, respectively, κ_0 is the vacuum permittivity, and κ_b is the relative background dielectric permittivity [28]. The depolarization field \mathbf{E}^d arises from the electrostatic interaction and is usually in the opposite direction of ferroelectric polarization, thus called the depolarization field. The electrostatic condition [29]

$$\kappa_0 \kappa_b \frac{\partial E_i^d}{\partial x_i} + \frac{\partial P_i}{\partial x_i} = 0 \tag{1-6}$$

is assumed to hold at each evolution step, from which \mathbf{E}^d can be solved. The electrostatic equilibrium equation (Equation 1-6) is a Poisson equation, where a Fourier spectral solution [29] is employed in the present dissertation. The contribution of electrostatic energy to the driving force is calculated as

$$f_P^{\text{elastic}} = -\left(E_i^{\text{ext}} + E_i^d\right) \quad (1-7)$$

The elastic energy F_{elastic} is expressed as [30]

$$F_{\text{elastic}} = \int \frac{1}{2} c_{ijkl} \left(\varepsilon_{ij} - \varepsilon_{ij}^0\right) \left(\varepsilon_{kl} - \varepsilon_{kl}^0\right) d\mathbf{x}^3, \quad (1-8)$$

where \mathbf{c} is the elastic stiffness tensor and ε^0 is the stress-free strain (or eigenstrain) related to the local ferroelectric order,

$$\varepsilon_{ij}^0 = Q_{ijkl} P_k P_l + \varepsilon_{ij}^{\text{lattice}} \quad (1-9)$$

\mathbf{Q} denoting the electrostrictive coefficient tensor, and $\varepsilon^{\text{lattice}}$ is the stress-free strain of the lattice arising from factors other than the polarization order, e.g., lattice mismatch between phases, thermal expansion effect, or magnetostriction, etc. Based on Equations 1-8 and 1-9, the contribution of the elastic energy to the driving force is further calculated as

$$f_P^{\text{elastic}} = 2\sigma_{jk} Q_{jkli} P_l \quad (1-10)$$

$\sigma_{ij} = c_{ijkl} \left(\varepsilon_{kl} - \varepsilon_{kl}^0\right)$ is the local stress field. An elastic equilibrium condition is assumed at each evolution step, as expressed by the elastic equilibrium equation:

$$\frac{\partial \sigma_{ij}}{\partial x_j} = 0 \quad (1-11)$$

with zero external body force. Equation 1-11 is solved using a Fourier spectral scheme [30] in the present dissertation.

1.2.2 Phase-field model of ferroelectric composites

For modeling a ferroelectric composite or heterostructure, a fixed phase field $\eta_b(\mathbf{x})$ describing the multi-phase structure is considered, which serves as an additional order parameter other than the polarization order. $\eta_b(\mathbf{x})$ is the local concentration of the b -th phase, with $0 < \eta_b(\mathbf{x}) < 1$. $\eta_b(\mathbf{x})$ follows either a sharp interface or diffuse interface description. This allows a spatial variation of material properties in the system, expressed as a linear combination of each phase:

$$\mathbf{y}(\mathbf{x}) = \sum_b \eta_b(\mathbf{x}) \mathbf{y}_b \quad (1-12)$$

Here \mathbf{y} presents material constants including Landau coefficients, background dielectric permittivity, elastic stiffness tensor, and electrostrictive coefficient, etc. \mathbf{y}_b is the material constants of the b -th phase.

With spatial varying properties, both the electrostatic Poisson equation (Equation 1-6) and the elastic equilibrium equation (Equation 1-11) change to partial differential equations with spatial-dependent coefficients, which are solved through employing Fourier-spectral iterative-perturbation methods [31, 32] in the dissertation.

1.3 Research Objectives

The main purpose of the present research is to investigate the properties of ferroelectric composites and heterostructures using a phase-field model. The specific objectives of the dissertation are: (1) to develop several phase-field models describing the piezoelectric, magnetoelectric, and electrothermal coupling, of static, relaxational kinetic and ultrafast dynamic time scales, in ferroelectric and magnetic/ferroelectric composites and heterostructures; (2) to examine linear magnetoelectric cross-coupling in magnetic/ferroelectric composites, focusing on microstructure influences; (3) to investigate kinetic properties of elastically coupled colinear

ferroelectric and magnetic domains in magnetic/ferroelectric heterostructures; (4) to study ferroelectric properties and electrocaloric effect in ferroelectric/relaxor composites; (5) to explore transient phenomena during ferroelectric domain evolution under various ultrafast external stimuli in ferroelectric oxides.

1.4 Dissertation structure

This dissertation contains six chapters: (1) Introduction, (2) Predicting effective magnetoelectric response in magnetic/ferroelectric composites via phase-field modeling, (3) Phase-field study on kinetic properties of elastically coupled magnetic and ferroelectric domains, (4) Phase-field study on an anomalous negative electrocaloric effect in a ferroelectric/relaxor composite, (5) Phase-field study on inhomogeneous ferroelectric domain dynamics under ultrafast stimuli, and (6) Conclusions and future work.

In Chapter 1, basic concepts of ferroelectric composites and heterostructures are briefly introduced. The main research tool of phase-field modeling and research objectives of the dissertation are discussed.

In Chapter 2, a phase-field model coupled with constitutive equations is formulated to investigate the magnetoelectric cross-coupling in magnetic/ferroelectric composites. The model allows us to obtain static piezoelectric, piezomagnetic, dielectric, and magnetoelectric properties under a given magnetic or electric field, from the local distributions of polarization, magnetization, and strain in the composites. Taking $\text{CoFe}_2\text{O}_4/\text{BaTiO}_3$ composites as an example, effective magnetoelectric coupling coefficient, i.e., magnetic-field-induced voltage output (or changes in polarization response), is numerically calculated. Influences of several microstructural

factors including the phase connectivity and the phase fraction of the composites on the magnetoelectric coupling properties are discussed.

In Chapter 3, a phase-field model is employed to study the kinetic properties of elastically coupled colinear magnetic and ferroelectric domains that show one-to-one pattern match. A multiferroic layered heterostructure of $\text{Co}_{0.4}\text{Fe}_{0.6}/\text{BaTiO}_3$ is considered as an example. Kinetics of the local elastic coupling is investigated by simulating the time-dependent electric-field-driven responses in local magnetization/polarization/strain distributions and by comparing the associated velocities of the magnetic and ferroelectric domain walls. The simulation reveals the electric-field-driven magnetic domain and domain wall kinetics with an alternating occurrence of local magnetization rotation and coupled motion of magnetic and ferroelectric domain walls with almost identical velocities.

In Chapter 4, we investigate an anomalous negative electrocaloric effect in the P(VDF-TrFE)/P(VDF-TrFE-CFE) ferroelectric/relaxor composite which shows cooling phenomenon upon applying an electric-field pulse without subsequent heating, through applying a phase-field model. Evolution of domain structure and changes in dipole ordering upon applying the electric field pulse is simulated. It is revealed that existence of the P(VDF-TrFE) normal ferroelectric phase and P(VDF-TrFE-CFE) relaxor phase act to stabilize the ordered and disordered state, respectively, leading to such anomalous electrocaloric effect. At room temperature, an adiabatic cooling of $\Delta T = -2.6^\circ\text{C}$ on applying $E = 30\text{MV/m}$ is found. The influence of operating temperature is predicted and discussed.

In Chapter 5, a phase-field model is developed for understanding and predicting the dynamical responses of both ferroelectric and ferroelastic domain patterns under ultrafast electrical, thermal, mechanical, and optical stimuli, with advanced numerical algorithms for solving the governing dynamical equations. As an example, the nanoscale and mesoscale domain dynamics of BaTiO_3 crystals under ultrafast stimuli are investigated. Deterministic 180°

ferroelectric domain switching through the application of ultrashort mechanical stimuli is demonstrated. Furthermore, a laser-pulse-induced domain dynamics showing distinct responses determined by both the orientation and the location of the domains, as observed experimentally, is theoretically examined. Mesoscale mechanisms of ferroelectric domain and domain wall responses, as well as intrinsic lattice vibrations, are revealed.

In Chapter 6, the dissertation is summarized with some major conclusions listed. Some future directions related to the topic of the dissertation, including microstructure design of piezoelectric composites, phase-field study on ultrafast dynamics in magnetic/ferroelectric heterostructures, and phase-field study on ultrafast dynamics in electronic phase transitions, are further discussed.

Chapter 2

Predicting effective magnetoelectric response in magnetic/ferroelectric composites via phase-field modeling

2.1 Introduction

Magnetoelectric composites of magnetic and ferroelectric materials offer advantages over most single-phase magnetoelectric materials due to their strong magnetoelectric coupling effect at room temperature and great design flexibility [17, 33-37]. The magnetoelectric effect in such composites is normally understood as a product property of piezoelectricity in ferroelectrics and piezomagnetism in magnets [38], leading to an electric polarization excited by a weak AC magnetic field (with either low or high frequencies) oscillating in a DC bias magnetic field, i.e., the direct magnetoelectric effect, or conversely, a modulation of magnetization upon DC or AC electric fields. Among them, the direct magnetoelectric effect has been extensively studied in various magnetoelectric composites since the early 1970s, and can be potentially used to develop highly sensitive magnetic field sensors [39-41], electric current probes [42], novel magnetoelectric read heads [43], and energy harvesters [44].

Theoretical approaches for such direct magnetoelectric effect include the early parallel-series type model [45], the Green's function technique (multiple-scattering approach) [38, 46, 47] micromechanical models [48-50] and the Landau-Ginzburg-Devonshire thermodynamic theory [51-55]. Although powerful, these continuum media methods are not capable of describing the spatial distribution of electric polarization, magnetization and elastic fields upon applying an external magnetic field. Such mesoscopic insights, however, can provide more explicit guidelines

for the improvement of the overall magnetoelectric responses based on a deeper understanding of the microstructure-property correlation.

In the present work, based on a phase-field model [23, 24, 56-61] coupled with constitutive equations, we can simulate both the effective magnetoelectric coupling coefficients and the local distributions of electric polarization (i.e., ferroelectric domains) for bulk magnetoelectric composites with magnetic inclusions in a ferroelectric matrix. The obtained magnetoelectric coefficients are compared with existing results calculated by the Green's function approach [38]. Influences of several parameters including the phase fraction and aspect ratio of the magnetic inclusions on the magnetoelectric coefficient were investigated.

2.2 Phase-field model for magnetoelectric composites with linear properties

Let us consider a typical two-phase bulk magnetoelectric composite with periodically aligned cuboid-shaped CoFe_2O_4 (CFO) inclusions embedded in a BaTiO_3 (BTO) matrix, as shown in Fig. 2-1. In particular, by changing the aspect ratio $r = c/a$ of the CoFe_2O_4 cuboids, the 2-2 type laminate ($r < 0.05$), 0-3 type ($0.05 \leq r < 10$) particulate and 1-3 type ($r \geq 10$) rod magnetoelectric composites can be described,⁶ where each number denotes the connectivity of each phase [16], as illustrated in Figs. 2-1(b)~(d), respectively.

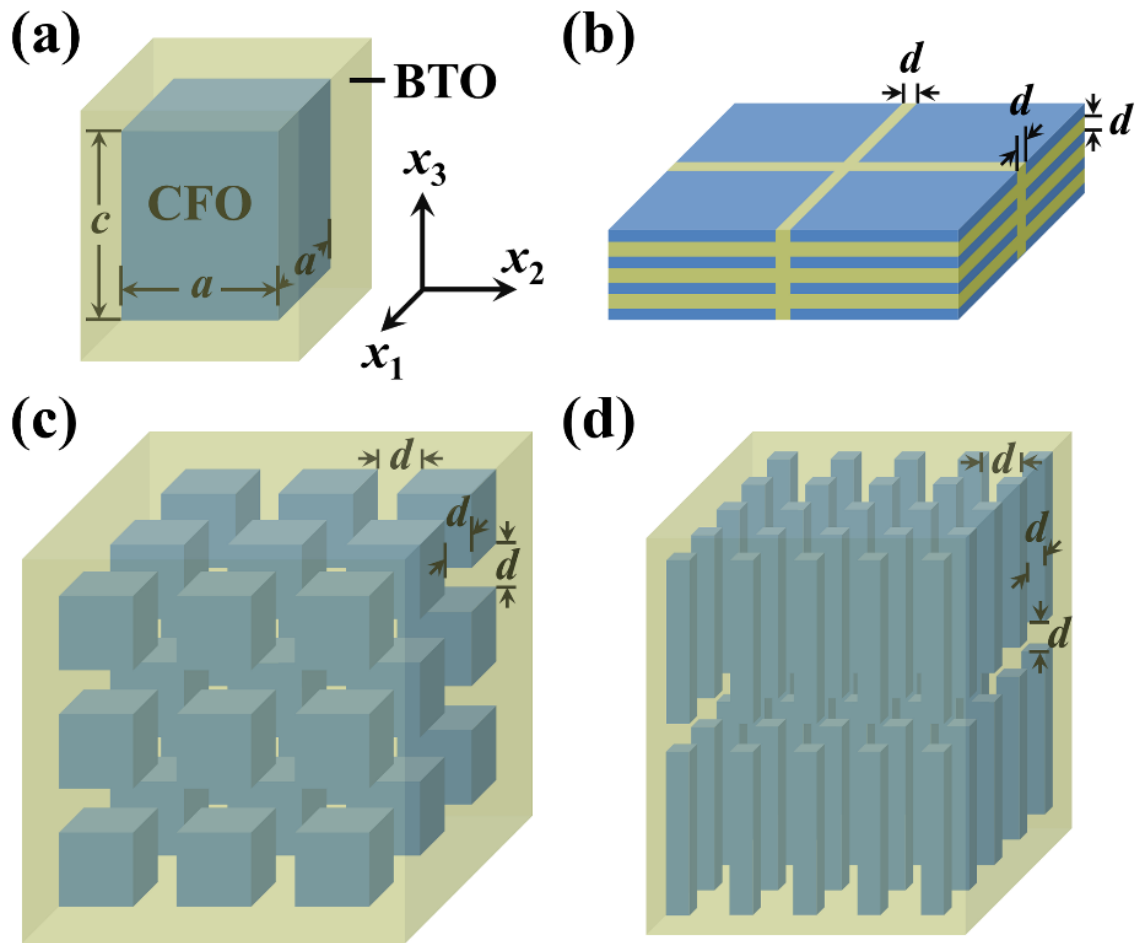


Figure 2-1. (a) Schematic illustration of the chosen simulation zone of the phase-field model, where a cuboid CoFe_2O_4 inclusion with a dimension of $a \times a \times c$ is embedded in a BaTiO_3 matrix. The composite is described by periodically aligning CoFe_2O_4 particles with a uniform separation distance d within all three directions. Composites of different phase connectivities including (b) 2-2, (c) 0-3 and (d) 1-3 types are obtained by varying the aspect ratios $r = c/a$ of the CoFe_2O_4 inclusions. The CoFe_2O_4 and BaTiO_3 phases are assumed to be intimately contacted at their interface region, with no gas phase (porosity) incorporated in the model.

2.2.1 Phase-field description of magnetoelectric coupling based on constitutive equations

As an example, uniform spontaneous magnetization M_S and polarization P_S (magnetic and ferroelectric single domains) along the out-of-plane axis are assumed for the CoFe_2O_4 and BaTiO_3 phases, respectively. Therefore, it is expected that it exhibits longitudinal magnetoelectric

effect⁶ based on the cross-product of the piezomagnetic and piezoelectric effects. In this case, relations between the stress $\boldsymbol{\sigma}$, strain $\boldsymbol{\varepsilon}$, electric displacement \mathbf{D} , electric field \mathbf{E} , magnetic induction \mathbf{B} and magnetic field \mathbf{H} can be described by the following linear constitutive equations [38], i.e.,

$$\begin{cases} \boldsymbol{\sigma} = {}^m \mathbf{c} \boldsymbol{\varepsilon} - {}^m \mathbf{q}^T \mathbf{H} \\ \mathbf{D} = \kappa_0 {}^m \boldsymbol{\kappa}_r \mathbf{E} \\ \mathbf{B} = {}^m \mathbf{q} \boldsymbol{\varepsilon} + \mu_0 {}^m \boldsymbol{\mu}_r \mathbf{H} \end{cases} \quad (2-1)$$

and

$$\begin{cases} \boldsymbol{\sigma} = {}^e \mathbf{c} \boldsymbol{\varepsilon} - {}^e \mathbf{e}^T \mathbf{E} \\ \mathbf{D} = {}^e \mathbf{e} \boldsymbol{\varepsilon} + \kappa_0 {}^e \boldsymbol{\kappa}_r \mathbf{E}, \\ \mathbf{B} = \mu_0 {}^e \boldsymbol{\mu}_r \mathbf{H} \end{cases} \quad (2-2)$$

for the CoFe_2O_4 and BaTiO_3 phases, respectively. Here \mathbf{c} , κ_0 , $\boldsymbol{\kappa}_r$, μ_0 and $\boldsymbol{\mu}_r$ denote the elastic stiffness, dielectric permittivity of vacuum, relative dielectric permittivity, magnetic permeability of vacuum and relative magnetic permeability, respectively. \mathbf{e} and \mathbf{q} are the piezoelectric and piezomagnetic coefficient tensors, respectively. The superscript T denotes the transpose of a tensor matrix, while presuperscripts m and e denote the constants of CoFe_2O_4 (magnetic) and BaTiO_3 (ferroelectric) phases, respectively. The room-temperature ($T = 298\text{K}$) material constants are listed in Table 2-1 [62-64].

Table 2-1. Material constants of CoFe_2O_4 and BaTiO_3 .

Material Constant	Unit	CoFe_2O_4	BaTiO_3
c_{11}	GPa	286	166.2
c_{12}	GPa	173	76.5
c_{33}	GPa	269.5	161.4
c_{13}	GPa	170.5	77.4
c_{44}	GPa	45.3	43.0

μ_{r33}	1	125	8
q_{31}	N/(A·m)	580.3	0
q_{33}	N/(A·m)	699.7	0
κ_{r33}	1	10	1350
e_{31}	C/m ²	0	-4.22
e_{33}	C/m ²	0	18.6

The direct magnetoelectric coupling coefficient in magnetoelectric composites can be extracted from the linear field-dependence under a relatively small applied magnetic field [35], i.e.,

$$\begin{cases} \boldsymbol{\sigma} = \mathbf{c}\boldsymbol{\varepsilon} - \mathbf{e}^T \mathbf{E} - \mathbf{q}^T \mathbf{H} \\ \mathbf{D} = \mathbf{e}\boldsymbol{\varepsilon} + \kappa_0 \boldsymbol{\kappa}_r \mathbf{E} + \boldsymbol{\alpha} \mathbf{H} \\ \mathbf{B} = \mathbf{q}\boldsymbol{\varepsilon} + \boldsymbol{\alpha}^T \mathbf{E} + \mu_0 \boldsymbol{\mu}_r \mathbf{H} \end{cases} \quad (2-3)$$

Note that the magnetoelectric coefficient tensor $\boldsymbol{\alpha}$ in Equations 2-1 ~ 2-3 is absent in both the magnetic and ferroelectric phases (Equations 2-1 and 2-2).

The microstructure (i.e., magnetic/ferroelectric domains, phase distribution) of the bulk magnetoelectric composite can be conveniently described within the framework of the phase-field model. Three non-conserved order parameters are utilized, including a local magnetization field $\mathbf{M}(\mathbf{x}) = (M_1, M_2, M_3)$, a local polarization field $\mathbf{P}(\mathbf{x}) = (P_1, P_2, P_3)$, and a phase order parameter $\eta(\mathbf{x})$ which describes the spatial distribution of the two phases, with $\eta(\mathbf{x}) = 1$ for the CoFe₂O₄ phase and $\eta(\mathbf{x}) = 0$ for the BaTiO₃ phase; \mathbf{x} is the position vector herein. Furthermore, temporal evolution of both the local magnetization and polarization distributions can be described by the Allen-Cahn equation [65], i.e.,

$$\begin{cases} \frac{\partial \mathbf{P}}{\partial t} = -L_1 \frac{\partial f}{\partial \mathbf{P}} \\ \frac{\partial \mathbf{M}}{\partial t} = -L_2 \frac{\partial f}{\partial \mathbf{M}} \end{cases}, \quad (2-4)$$

where L_1 and L_2 are kinetic coefficients related to evolution kinetics, and f is the local free energy density. Particularly, the formulation of the free energy density f in the present work is constructed based on previous phase-field models [24, 57] such that by minimizing it following Equation 2-4, the constitutive equations (Equations 2-1 and 2-2) could be automatically satisfied.

The total free energy is given by

$$f = f_{\text{magnetic}} + f_{\text{electric}} + f_{\text{elastic}}, \quad (2-5)$$

where f_{magnetic} , f_{electric} and f_{elastic} are the magnetic, electric, and elastic energy, respectively, expressed as,

$$f_{\text{magnetic}} = \eta \left(\frac{\mu_0}{2({}^m\mu_{r ii}^\sigma - 1)} M_i^2 \right) + (1-\eta) \left(\frac{\mu_0}{2({}^e\mu_{r ii}^\sigma - 1)} M_i^2 \right) - \frac{1}{2} \mu_0 H_i^d M_i - \mu_0 H_i^{\text{ext}} M_i, \quad (2-6)$$

$$f_{\text{electric}} = \eta \left(\frac{1}{2\kappa_0({}^m\kappa_{r ii}^\sigma - 1)} P_i^2 \right) + (1-\eta) \left(\frac{1}{2\kappa_0({}^e\kappa_{r ii}^\sigma - 1)} P_i^2 \right) - \frac{1}{2} E_i^d P_i - E_i^{\text{ext}} P_i, \quad (2-7)$$

$$f_{\text{elastic}} = \eta \left[{}^m c_{IJ}^M (\varepsilon_I - \varepsilon_I^0) (\varepsilon_J - \varepsilon_J^0) \right] + (1-\eta) \left[{}^e c_{IJ}^P (\varepsilon_I - \varepsilon_I^0) (\varepsilon_J - \varepsilon_J^0) \right], \quad (2-8)$$

where summation conventions over $i, j, k, l = 1, 2, 3$ (or $I, J, K, L = 1 \sim 6$ where a Voigt notation is adopted) are employed. μ_r^σ , κ_r^σ , \mathbf{c}^M and \mathbf{c}^P are the stress-free relative magnetic permeability, stress-free relative dielectric permittivity, constant magnetization elastic stiffness and constant polarization elastic stiffness, given by ${}^m\mu_{r ij}^\sigma = {}^m\mu_{r ij} + {}^m q_{iK} {}^m q_{jL} {}^m s_{KL}$, ${}^e\kappa_{r ij}^\sigma = {}^e\kappa_{r ij} + {}^e e_{iK} {}^e e_{jL} {}^e s_{KL}$, ${}^m c_{IJ}^M = {}^m c_{IJ} + {}^m q_{kl} {}^m q_{kj} / [\mu_0({}^m\mu_{r kk}^\sigma - 1)]$ and ${}^e c_{IJ}^P = {}^e c_{IJ} + {}^e e_{kl} {}^e e_{kj} / [\kappa_0({}^e\kappa_{r kk}^\sigma - 1)]$, respectively. \mathbf{s} ($=\mathbf{c}^{-1}$) is the elastic compliance tensor. \mathbf{H}^{ext} , \mathbf{H}^d , \mathbf{E}^{ext} and \mathbf{E}^d are the external magnetic, demagnetization, external electric and depolarization fields, respectively. ε^0 is the stress-free or phase transformation strain, which can be calculated as,

$$\varepsilon_i^0 = \eta \frac{{}^m s_{IJ}^M q_{kJ} M_k}{{}^m \mu_{rkk} - 1} + (1 - \eta) \frac{{}^e s_{IJ}^P e_{kJ} P_k}{\kappa_0 ({}^e \kappa_{rkk} - 1)}. \quad (2-9)$$

The demagnetization field \mathbf{H}^d and the depolarization field \mathbf{E}^d for the given distributions of magnetization and polarization are calculated by numerically solving the magnetostatic and electrostatic equations under periodic boundary conditions, i.e.,

$$\begin{cases} \partial H_i / \partial x_i = -\partial M_i / \partial x_i \\ \partial E_i / \partial x_i = -(1/\kappa_0) \cdot \partial P_i / \partial x_i \end{cases}, \quad (2-10)$$

where x_i is the i -th component of the position vector in the Cartesian coordinates. The solution for Equation 2-10 is obtained by introducing the magnetic scalar potential and electric potential, which are solved in the Fourier space; the details are given in Refs. [66] and [29]. The elastic field is obtained by solving the mechanical equilibrium equations

$$\partial c_{ijkl} (\varepsilon_{kl} - \varepsilon_{kl}^0) / \partial x_j = 0 \quad (2-11)$$

using an iteration method developed for materials with elastic inhomogeneity [67, 68] based on Khachaturyan's microelasticity theory [69]. Note that a 3×3 strain tensor ε_{kl} is used in Equation 2-11, while the Voigt notation is adopted elsewhere for simplicity. A clamped elastic boundary condition is employed, i.e., no macroscopic shape deformation happens for the composite materials during evolution.

2.2.2 Simulation setup

The basic building block of the magnetoelectric composites (see Fig. 2-1(a)) is discretized into a 3-dimensional array of cubic grid cells, i.e., $n_1 \Delta l \times n_2 \Delta l \times n_3 \Delta l$, where n_1 , n_2 and n_3 denote the numbers of grid cells along the x_1 , x_2 , and x_3 axes, respectively, with a total grid cell number of around $n_1 n_2 n_3 = 300,000$; Δl is the size of each grid in the real space. By properly choosing the grid numbers along each cubic axis and allocating the grid cells for BaTiO₃ and

CoFe₂O₄ regions, systems with different aspect ratios r and phase fractions V_f of the CoFe₂O₄ inclusions can be modeled. Δl is taken as 2.5 nm, corresponding to a total system size of $n_1\Delta l \times n_2\Delta l \times n_3\Delta l = 4,500,000\text{nm}^3$. In this case, the lateral size of the CoFe₂O₄ inclusions, e.g., $a = 28.2\text{nm}$ for $r = 100$ and $V_f = 0.5$, would be comparable to experiments (i.e., 20~30nm, Ref. [70]). Through solving Equation 2-4 using the forward Euler method [71], the magnetization and polarization distributions responsive to a given external field are obtained, and the effective direct magnetoelectric response of the composite can then be calculated upon local magnetization/polarization/strain fields achieving an equilibrium.

2.3 Results and discussion

2.3.1 Elasticity-mediated polarization response to an external magnetic field

Figures 2-2(a)~(c) show the equilibrium spatial distributions of the local strain and polarization fields in the 0-3 type, 2-2 type, and 1-3 type CoFe₂O₄/BaTiO₃ composites, respectively, in response to an external magnetic field along the positive x_3 axis, i.e., $H_3^{\text{ext}} = 100 \text{ A/m}$. The volume fraction of the CoFe₂O₄ phase V_f is fixed at 0.5. Upon this field, the magnetic CoFe₂O₄ phase would expand in the x_1 - x_2 plane [see the strain distributions of $\varepsilon_2 (= \varepsilon_1)$ on the left of Figs. 2-2(a)~(c)] due to its positive piezomagnetic coefficient $q_{32} (= q_{31})$, which leads to a compression near the contact region of the ferroelectric BaTiO₃ phase in the lateral direction (denoted as region 1), i.e., a negative strain $\varepsilon_2 (= \varepsilon_1)$, due to zero shape deformation in the whole composite under the clamped elastic boundary condition. Accordingly, such in-plane compressive strains in the BaTiO₃ phase induce a positive longitudinal polarization P_3 due to its negative piezoelectric coefficient $e_{32} (= e_{31})$ [see the polarization distributions on the

right of Figs. 2-2(a)~(c)]. Furthermore, CoFe_2O_4 also expands along the longitudinal x_3 direction [see the strain distributions of ε_3 in the middle of Figs. 2-2(a)~(c)] upon the positive H_3^{ext} because of a positive q_{33} . It compresses its intimately contacted BaTiO_3 phase region in the longitudinal direction (denoted as region 2), i.e., a negative ε_3 , and thus induces a negative P_3 in region 2 as $e_{33} > 0$.

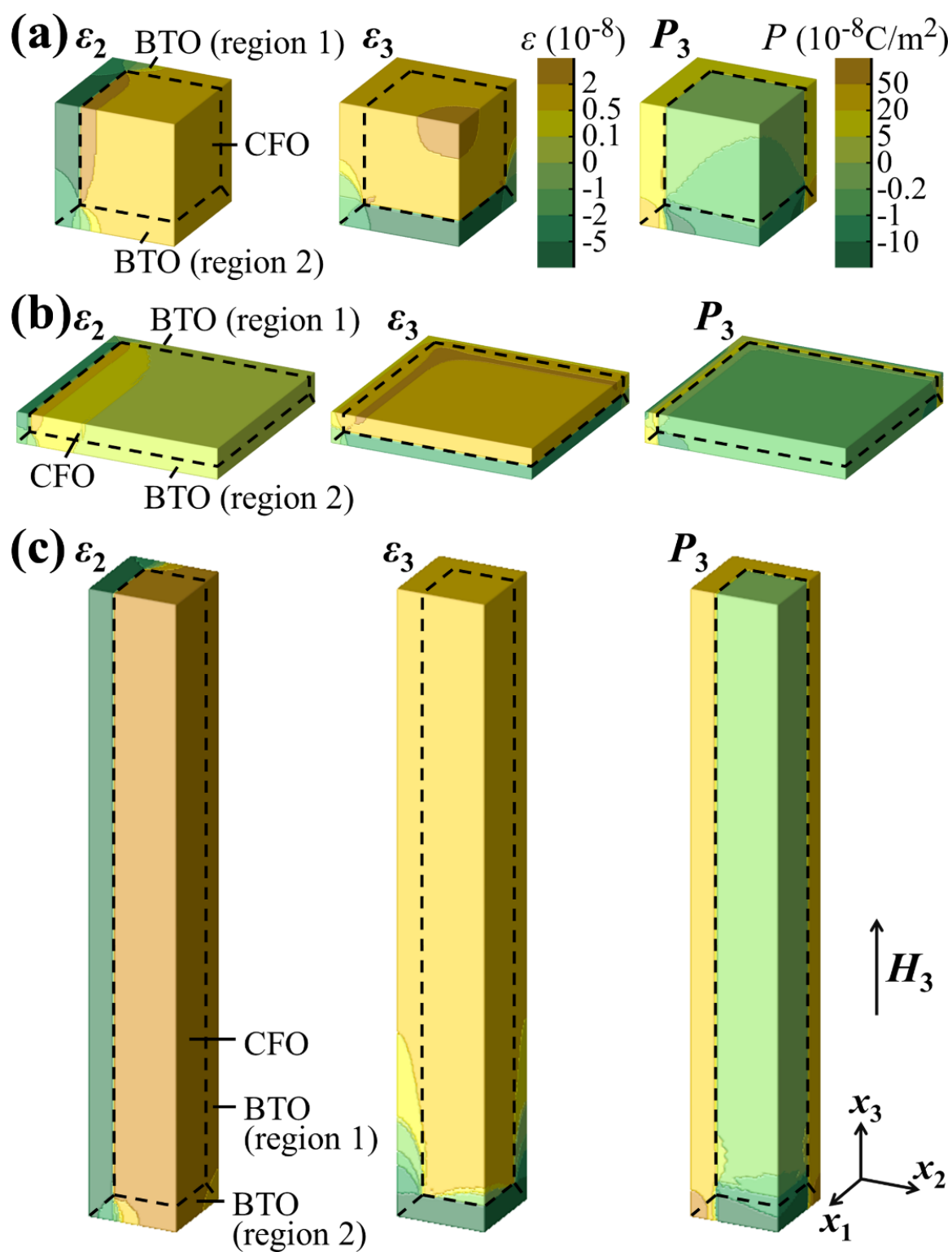


Figure 2-2. Equilibrium distributions of the lateral strain ε_2 , longitudinal strain ε_3 , and the longitudinal polarization P_3 responsive to an longitudinally applied magnetic field

$H_3 = 100 \text{ A/m}$, in composites of (a) 0-3 ($r=1$), (b) 2-2 ($r=0.02$) and (c) 1-3 ($r=10$) connectivities, with the CoFe_2O_4 phase fraction V_f taken as 0.5. For clarity, only 1/8 (half length in each dimension) of one building block is shown. Dashed lines indicate the $\text{CoFe}_2\text{O}_4/\text{BaTiO}_3$ phase boundaries and the partition of lateral and longitudinal regions in the BaTiO_3 phase.

Hence, the average polarization response \overline{P}_3 of the composite is determined by the competition between the lateral and longitudinal regions. For the laminated 2-2 type composites with a small r (see Fig. 2-2(b) for the case of $r=0.02$), the BaTiO_3 phase is dominated in volume by the longitudinal region 2, leading to an overall negative \overline{P}_3 as discussed above. However, the magnitude of \overline{P}_3 is small in such laminate geometry due to the strong longitudinal depolarization and demagnetization effect (Equation 2-10). For 0-3 type composites (see Fig. 2-2(a) for the case of $r=1$), the BaTiO_3 phase is composed of region 1 and region 2 with comparable volumes. However, the contribution from the lateral region 1 is dominant due to the stronger depolarization in the longitudinal region 2, and therefore the composite exhibits a positive \overline{P}_3 . It also shows a larger magnitude than that in laminated composites due to the enhanced value of both the strain ε_2 and ε_3 (Fig. 2-2(a)) from the reduced longitudinal demagnetization (and therefore a larger M_3) in such particulate magnetoelectric composites. Finally, in the 1-3 type magnetoelectric composites with an even larger aspect ratio r ($= 10$ in Fig. 2-2(c)) for the CoFe_2O_4 rod, the volume of the lateral region 1 becomes dominant, leading to a positive \overline{P}_3 . The greatly reduced longitudinal depolarization and demagnetization effects in such vertical geometry further enhance the magnitude of this positive \overline{P}_3 , indicating a very strong magnetoelectric coupling. evolution.

2.3.2 Influence of the aspect ratio of inclusions

With these magnetic-field-induced polarization distributions in mind, the effective direct magnetoelectric coefficient α_{ij} (in the unit of s/m) can be easily calculated following the constitutive equations (Equation 2-3), expressed as,

$$\alpha_{ij} = \overline{P}_i / H_j^{\text{ext}}. \quad (2-12)$$

For illustration, Fig. 2-3(a) presents the effective magnetoelectric coefficient α_{33} of CoFe₂O₄/BaTiO₃ composites with a fixed CoFe₂O₄ phase fraction $V_f = 0.5$ as a function of the aspect ratio r . The composite shows a small and negative α_{33} at a low r below 0.05 (2-2 type). As aspect ratio increases, α_{33} undergoes a sign change and then increases significantly at $r > 1$, indicating a reversal of the net longitudinal polarization \overline{P}_3 from downward to upward direction as discussed above.

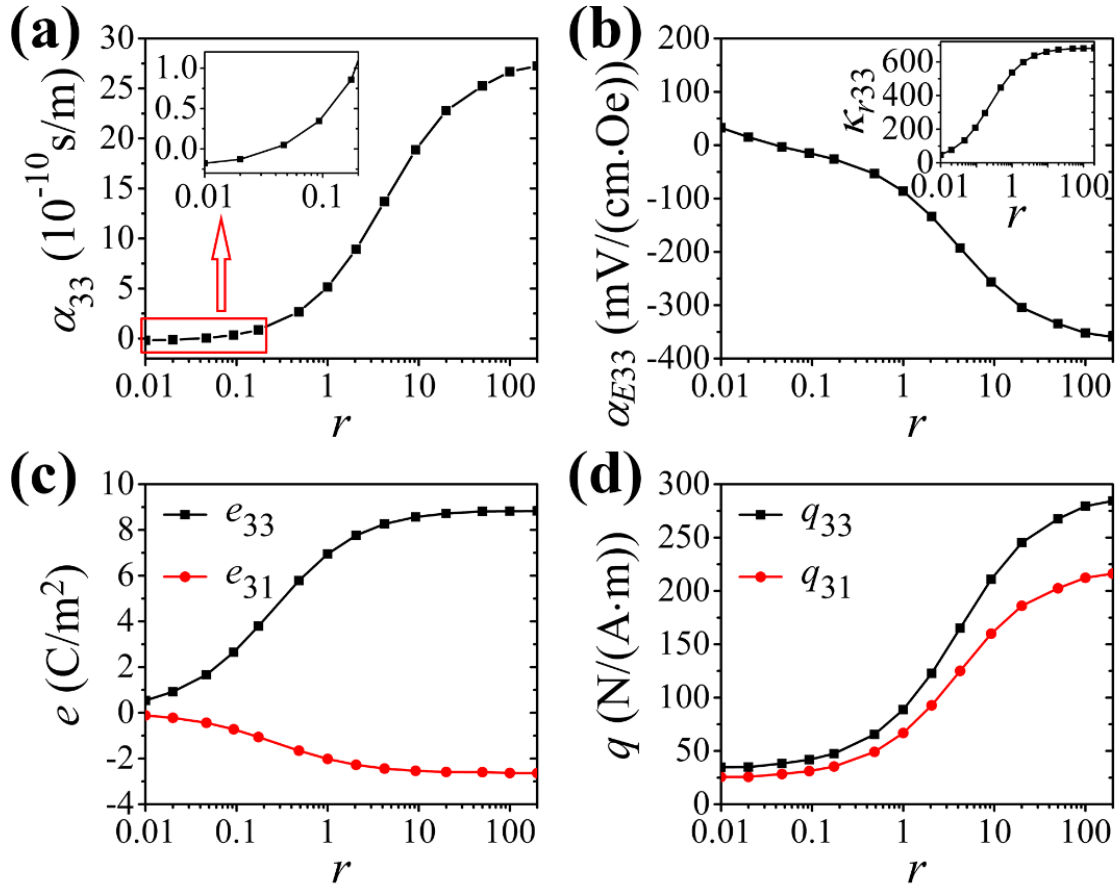


Figure 2-3. Effective (a) magnetoelectric coefficients (enlarged scale of the red rectangle part shown as inset), (b) magnetoelectric voltage coefficients (relative dielectric permittivity shown as inset), (c) piezoelectric coefficients and (d) piezomagnetic coefficients of the $\text{CoFe}_2\text{O}_4/\text{BaTiO}_3$ composites as a function of the aspect ratio r . The volume fraction of the CoFe_2O_4 phase is set to be 0.5.

Moreover, the effective magnetoelectric voltage coefficient α_{E33} (in the unit of $\text{mV cm}^{-1} \text{Oe}^{-1}$) can be written as $\alpha_{E33} = -\alpha_{33}/(\kappa_0 \kappa_{r33})$. The relative dielectric permittivity κ_r of the composite can be calculated following Equation 2-3 with the equilibrium average electric displacement $\bar{\mathbf{D}}$ obtained under an applied external electric field \mathbf{E}^{ext} ,

$$\kappa_{rij} = \bar{D}_i / (\kappa_0 E_j^{\text{ext}}). \quad (2-13)$$

We employ a small electric field $E_3^{\text{ext}} = 50\text{V/cm}$ along the positive x_3 axis. Dependences of the effective α_{E33} and κ_{r33} on the aspect ratio r are shown in Fig. 2-3(b) and its inset, respectively. As seen, the composite shows a dielectric permittivity starting from a small $\kappa_{r33} = 48$ for $r=0.01$. The dielectric constant is greatly enhanced with an increasing r to a large $\kappa_{r33} = 682$ for $r=200$, which can be explained in the context of an equivalent serial circuit of the low-capacitance CoFe_2O_4 and the high-capacitance BaTiO_3 for the 2-2 laminated geometry gradually changing to an equivalent parallel circuit for the 1-3 rod geometry. As a combined property of α_{33} and κ_{r33} , the magnetoelectric voltage coefficient α_{E33} is positive in the laminated composites ($r < 0.05$), undergoes a sign change at around $r = 0.05$ (belonging to 0-3 particulate composites), and then increases remarkably on increasing r in 0-3 ($0.05 \leq r < 10$) particulate and 1-3 ($r \geq 10$) rod composites.

Besides the magnetoelectric response, the piezoelectric and piezomagnetic properties of the composite can also be obtained by examining the induced average polarization and magnetization upon imposing a uniaxial net strain $\overline{\varepsilon_j}$ (taken as 0.01% herein), i.e., $e_{ij} = \overline{P_i} / \overline{\varepsilon_j}$ and $q_{ij} = \mu_0 \overline{M_i} / \overline{\varepsilon_j}$. Shown in Figs. 2-3(c) and 2-3(d) are the variations of the longitudinal piezoelectric coefficient e_{3I} ($I=1,3$) and piezomagnetic coefficient q_{3I} ($I=1,3$) with the aspect ratio r . Both coefficients gradually increase with an increasing r , indicating a higher longitudinal piezoelectric and piezomagnetic coupling in the 1-3 rod composites, which would allow a stronger elastic interaction across the $\text{CoFe}_2\text{O}_4/\text{BaTiO}_3$ interface and hence a larger direct magnetoelectric effect. By contrast, the average longitudinal polarization $\overline{P_3}$ and magnetization $\overline{M_3}$ in the 2-2 laminated composites would be suppressed by large longitudinal depolarization and demagnetization fields, respectively, leading to smaller piezoelectric and piezomagnetic coefficients and a weaker direct magnetoelectric coupling.

2.3.3 Influence of phase fractions

We further study the influence of the phase fraction V_f on the direct magnetoelectric coefficient, as shown in Fig. 2-4(a). The obtained results agree well with previous predictions based on Green's function approach⁶ in CoFe₂O₄/BaTiO₃ composites with ellipsoidal CoFe₂O₄ inclusions. As can be seen, for all aspect ratios studied, the direct magnetoelectric coefficient α_{33} , which is zero in the single CoFe₂O₄ and BaTiO₃ phases (i.e., $V_f = 1$ and 0), emerges in the composite and reaches a maximum at a certain phase fraction. For instance, the maximum value of α_{33} at $r = 100$ is about 2.81×10^{-9} s/m at $V_f \approx 0.59$ (Fig. 2-4(a)). To better understand this, the elastic interaction between the BaTiO₃ and CoFe₂O₄ phases is examined. For the clamped case studied, the average field-induced strain in the CoFe₂O₄ and BaTiO₃ phases, i.e., $\overline{\epsilon^m}$ and $\overline{\epsilon^e}$, would be related as $V_f \overline{\epsilon^m} = -(1 - V_f) \overline{\epsilon^e}$, where $V_f \overline{\epsilon^m}$ could be considered as the average strain transferred across the CoFe₂O₄/BaTiO₃ interface, i.e., the strength of the elastic interaction. As an example, Fig. 2-4(b) shows the $V_f \overline{\epsilon^m}$ as a function of V_f in composites with different aspect ratios r . The maximum $V_f \overline{\epsilon^m}$ appears at medium phase fractions (e.g. $V_f \approx 0.59$ for $r = 100$), where both $\overline{\epsilon^m}$ and $\overline{\epsilon^e}$ can reach a relatively large value and hence ensure the largest magnetoelectric coupling coefficient α_{33} (Fig. 2-4(a)).

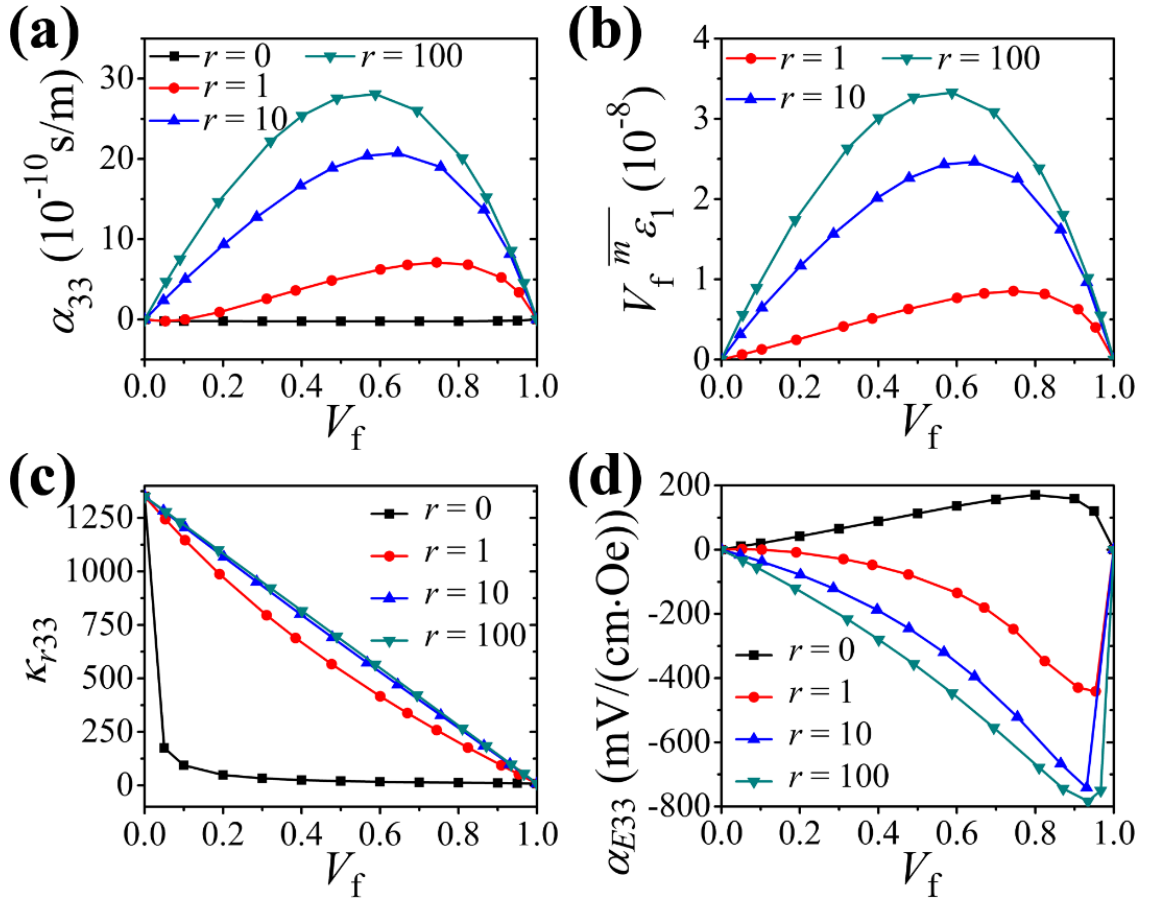


Figure 2-4. Effective (a) magnetoelectric coefficients, (c) relative dielectric permittivity and (d) magnetoelectric voltage coefficients of the $\text{CoFe}_2\text{O}_4/\text{BaTiO}_3$ composite with different aspect ratios r as a function of the phase-fraction V_f . (b) $V_f^m \overline{\epsilon}_1$ of the composite with different aspect ratios r upon applying a magnetic field $H_3^{\text{ext}}=100\text{A/m}$, as a function of the phase-fraction V_f .

It is also worth noting that the phase fraction V_f for the maximum α_{33} gradually shifts towards the CoFe_2O_4 -rich side (i.e., $V_f > 0.5$) from 0.59 to 0.74 as the aspect ratio r decreases from 100 to 1 (see Fig. 2-4(a)). This is because higher volume fractions V_f would be required to compensate the shrinking area of contact interface in the cases of 0-3 particulate composites compared to the relatively large interface area in the 1-3 rod composites such that the transferred field-induced strain $V_f^m \overline{\epsilon}$ can remain at a high value.

On the other hand, the effective longitudinal dielectric constant κ_{r33} rapidly decreases with increasing CoFe₂O₄ phase fraction V_f (Fig. 2-4(c)) due to the much smaller dielectric permittivity of the CoFe₂O₄, while it demonstrates a V_f dependence characteristic of an equivalent serial circuit of the low-capacitance CoFe₂O₄ and the high-capacitance BaTiO₃ for the 2-2 type structure ($r=0$), and of an equivalent parallel circuit for the 1-3 type structure ($r=100$). Figure 2-4(d) show the effective magnetoelectric voltage coefficient α_{E33} as a function of CoFe₂O₄ phase fraction V_f . As shown, the strongest magnetoelectric voltage response emerges in heavily CoFe₂O₄-rich side where κ_{r33} is small. For example, the largest α_{E33} is obtained as -783 mV/(cmOe) at $V_f=0.93$ and $r=100$.

2.3.4 Magnetoelectric coupling in thin film nanocomposites

Although CoFe₂O₄/BaTiO₃ bulk composites with 1-3 type rod geometry exhibit the largest magnetoelectric coupling, it can be further enhanced in thin film and island nanostructures, through releasing the mechanical clamping in the longitudinal direction or both direction of the CoFe₂O₄ rods. Through phase-field simulation, we demonstrate (see Fig. 2-5) the enhanced magnetoelectric response in 1-3 type thin film and island nanostructures, compared with that of a clamped bulk. In addition, the thin film composites also show a sign change of longitudinal polarization response on altering aspect ratio r of the CoFe₂O₄ rods, due to the competition between lateral and longitudinal elastic interactions, similar to the elastic interaction discussed above in bulk composites.

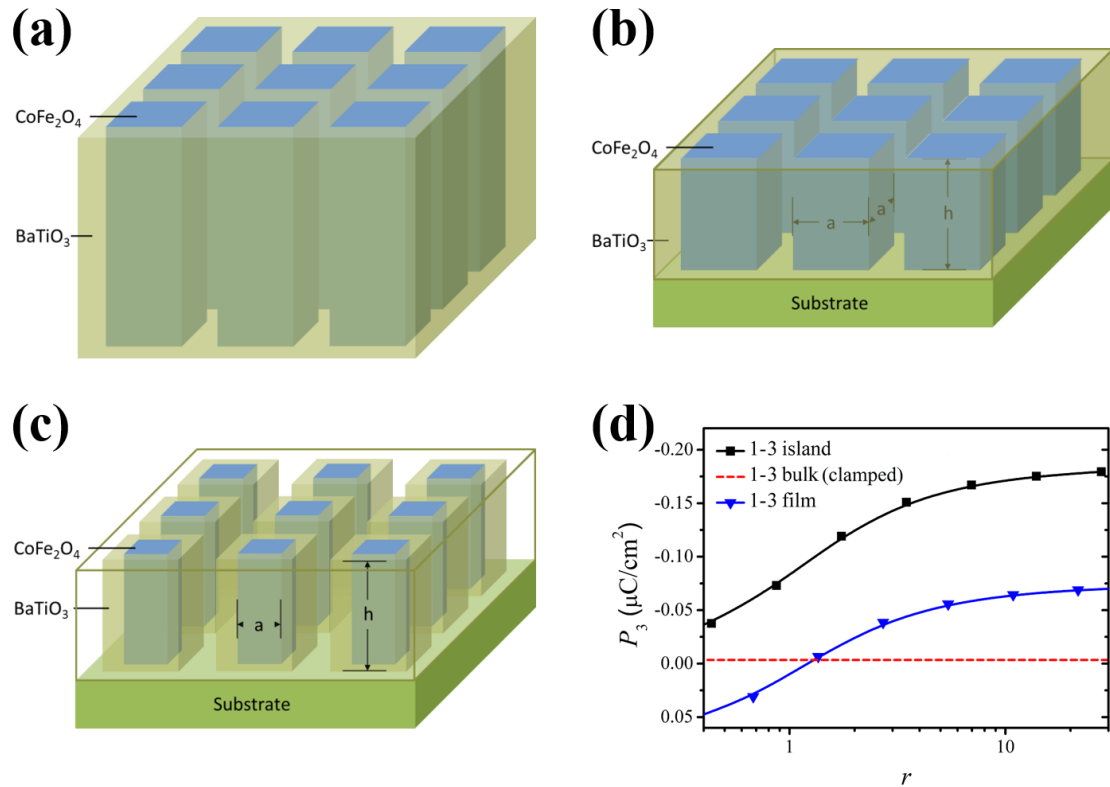


Figure 2-5. 1-3 type $\text{CoFe}_2\text{O}_4/\text{BaTiO}_3$ composites with thin film and island nanostructures show an enhanced magnetoelectric coupling property compared with 1-3 bulk composites with the same phase fraction. (a)~(c) Schematics of 1-3 type $\text{CoFe}_2\text{O}_4/\text{BaTiO}_3$ (a) bulk composites and composites with (b) thin film nanostructure and (c) island nanostructure. (d) Equilibrium polarization response P_3 as a function of the aspect ratio $r = h/a$ of the CoFe_2O_4 rods in 1-3 type island nanostructure and thin film nanostructure, respectively, compared with the polarization response in a 1-3 bulk composite, on applying an external magnetic field. Volume fraction of the CoFe_2O_4 phase is fixed at $V_f = 0.35$ for all composite structures.

Conclusion

In this chapter, a phase-field model coupled with constitutive equations has been developed to investigate the direct magnetoelectric coupling in bulk multiferroic

magnetic/ferroelectric composites. It provides a detailed examination of the composites that goes from the mesoscopic modeling of the local polarization/elastic field distributions (domains) to the predictions of effective magnetoelectric response within the context of the continuum media theory under a periodic boundary condition. These functional properties have proven to be strongly dependent on several microstructural factors of the composites including the phase fraction and phase connectivity. Such a simple phase-field based multi-scale approach should also have broad potential applications in predicting various effective properties such as the piezoelectric [72], piezomagnetic [73], dielectric [74], and elastic [75] responses in composite materials, which are directly deduced from the response of the complex microstructure to external fields.

This model can also be extended to include non-linear contributions to the effective properties, e.g., from domain wall motion, by incorporating magnetic exchange energy [66] and ferroelectric gradient energy [24, 27] in total free energy to describe magnetic and ferroelectric domain walls, respectively.

Chapter 3

Phase-field study on kinetic properties of elastically coupled magnetic and ferroelectric domains

3.1 Introduction

The scaling law for ferroics [76, 77] indicates that the domain width of magnets and ferroelectrics become comparable only when the thickness of ferroelectrics is much larger. Indeed, it has been recently demonstrated in multiferroic layered heterostructures with magnetic thin films directly grown on ferroelectric BaTiO₃ (BTO) substrates [78-85] that the domains in an as-grown magnetic thin film have not only the same width but also a surprising collinear alignment with the contacted ferroelectric domains. This further enables a precise control over the magnetic domain wall motion by electrically driving its elastically coupled ferroelectric domain wall [86, 87]. Such one-to-one match between magnetic and ferroelectric domains offers new opportunities for the creation of periodic magnetic domain patterns used for magnonic devices [88], and particularly, the low-power spintronic devices based on electro-strain-driven magnetic domain orientation [89, 90] or domain wall propagation [91, 92].

Theoretically, both *ab initio* calculations [80] and continuum-scale models [83] have been employed to describe the variations in the average magnetization as a function of electric field and/or temperature for such multiferroic magnetic/ferroelectric heterostructures. However, a rigorous 3-dimensional mesoscale model that can simulate the kinetic evolution of these elastic coupled magnetic and ferroelectric domains under external magnetic/electric field, is still lacking.

In this work, a phase-field model is developed to study the kinetics of such local elastic coupling between magnetic and ferroelectric domains in multiferroic heterostructures. We simulate the evolution of both types of domains upon applying an electric field to the heterostructure including field-driven changes in domain morphology and domain wall velocity. The simulation results agree with existing experimental observations. For illustration, we choose a model heterostructure with a polycrystalline $\text{Co}_{0.4}\text{Fe}_{0.6}$ (CoFe) magnetic film deposited on a BaTiO_3 single crystal substrate that initially has a periodic in-plane ferroelectric domain pattern [78, 81, 82].

3.2 Phase-field model

To overcome the challenge to model the large discrepancy between the thicknesses of the BaTiO_3 substrate ($\mu\text{m}\sim\text{mm}$) and the CoFe film ($\sim\text{nm}$), the phase-field modeling is carried out in two steps to mostly capture the mechanical boundary conditions in real systems: 1) simulating ferroelectric domain evolution and associated ferroelastic strain distribution in bulk BaTiO_3 substrate (Fig. 3-1(a)); 2) simulating magnetic domain evolution in CoFe film within a film-substrate system (Fig. 3-1(b)) [24], where effects of ferroelastic strains from the BaTiO_3 substrate are considered by employing a modified elastic boundary condition.

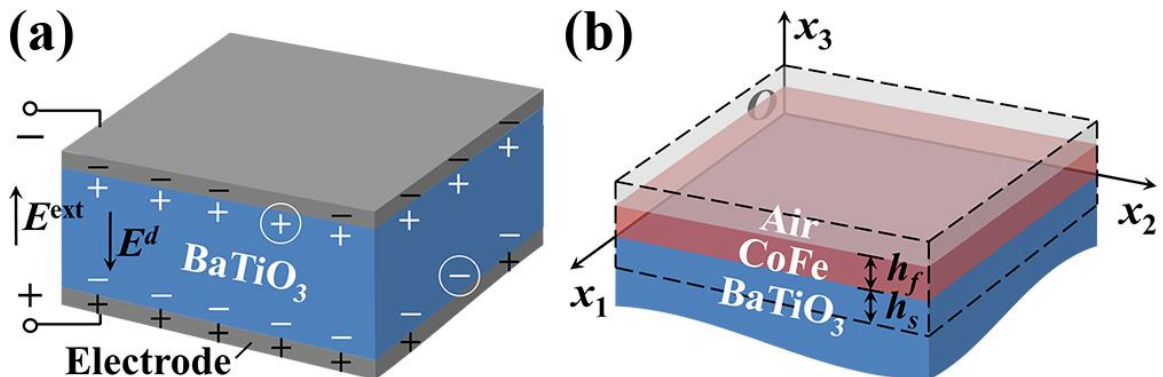


Figure 3-1. (a) Schematics of the simulation system in Step 1 of the phase-field model: determining ferroelectric domain structures in a fully electroded BaTiO₃ crystal substrate with uncompensated bound charges (see the circle) (b) Step 2: determining magnetic domain structures in the CoFe film in a film-substrate system. The simulation zone is marked by dashed lines, where a unique displacement boundary condition relating to polarization distribution (Equation 3-10) is applied at the bottom of the substrate at $x_3 = -h_s$.

3.2.1 Phase-field model on the ferroelectric domains

In Step 1, the total size of the bulk BaTiO₃ crystal is set as $800 \times 800 \times 400 \text{ nm}^3$, which is discretized into a 3-dimensional array of $160 \times 160 \times 80$ cells. The ferroelectric domain structure is described with a local polarization field $\mathbf{P}(\mathbf{x})$, where \mathbf{x} is the position vector.

Temporal evolution of the polarization field follows the time-dependent Ginzburg-Landau equation, i.e.,

$$\frac{\partial \mathbf{P}}{\partial t} = -L_p \frac{\delta F}{\delta \mathbf{P}}, \quad (3-1)$$

where L_p is a kinetic coefficient related to ferroelectric domain wall mobility [93]. F is the total free energy of the BaTiO₃ crystal, $F = F_{\text{Landau}} + F_{\text{gradient}} + F_{\text{electric}} + F_{\text{elastic}}$. Here F_{Landau} and F_{gradient} are the ferroelectric bulk free energy and ferroelectric gradient energy, respectively, with mathematic expressions given in Equations 1-3 and 1-4. F_{electric} is the electrostatic energy,

$$F_{\text{electric}} = \int \left(-\frac{1}{2} E_i^d P_i - E_i^{\text{ext}} P_i \right) dV, \quad (3-2)$$

where \mathbf{E}^d and \mathbf{E}^{ext} denote the depolarization field and the external electric field, respectively; summation conventions over repeat indices ($i = 1, 2, 3$) are employed. A mixed electrostatic boundary is considered in solving \mathbf{E}^d , in which the bound charges at the top and bottom electrodes are partly compensated (Fig. 3-1(a)), through treating the depolarization field as the

sum of a heterogeneous field $\mathbf{E}^{d,A}$ and a homogeneous field $\mathbf{E}^{d,B}$, i.e., $\mathbf{E}^d = \mathbf{E}^{d,A} + \mathbf{E}^{d,B}$. $\mathbf{E}^{d,A}$ is calculated by numerically solving the electrostatic equation

$$\kappa_0 \kappa^b \frac{\partial E_i^d}{\partial x_i} + \frac{\partial P_i}{\partial x_i} = 0 \quad (3-3)$$

using a short-circuit condition [29] on top and bottom boundaries, where κ_0 and κ^b are the vacuum and background dielectric permittivity [28], respectively. $\mathbf{E}^{d,B}$ is given by $\mathbf{E}^{d,B} = -k \bar{\mathbf{P}} / (\kappa_0 \kappa^b)$, in which $\bar{\mathbf{P}}$ is the average polarization in the system, and k is a factor determined by both the shape of the BaTiO₃ substrate and the fraction of uncompensated bound charges, which would affect the volume fraction of in-plane and out-of-plane ferroelectric domains at the remnant state. Here k is taken as 1% to describe the presence of a small fraction of uncompensated bound charges at the electrode/BaTiO₃ interface. The elastic energy F_{elastic} is expressed as,

$$F_{\text{elastic}} = \frac{1}{2} \int c_{ijkl} (\varepsilon_{ij} - \varepsilon_{ij}^0) (\varepsilon_{kl} - \varepsilon_{kl}^0) dV, \quad (3-4)$$

where \mathbf{c} is the elastic stiffness tensor and ε the total strain. $\varepsilon_{ij}^0 (= Q_{ijkl} P_k P_l$, \mathbf{Q} denoting the electrostrictive coefficient tensor) is the stress-free (or ferroelastic herein) strain during ferroelectric phase transitions (e.g., appearance of spontaneous polarization and polarization switching). The total strain $\varepsilon(\mathbf{x})$ is numerically solved based on Khachatryan's mesoscopic elasticity theory [69] under a 3-dimensional periodic stress-free boundary condition. The evolution of ferroelectric domains (Equation 3-1) is solved numerically using the semi-implicit Fourier spectral method [26]. Material parameters for the BaTiO₃ bulk crystal are $\alpha_1 = 8.0 \times 10^7 \times [1 / \tanh(160/T) - 1 / \tanh(160/390)]$, $\alpha_{11} = -1.154 \times 10^8$, $\alpha_{12} = 6.530 \times 10^8$, $\alpha_{111} = -2.106 \times 10^9$, $\alpha_{112} = 4.091 \times 10^9$, $\alpha_{123} = -6.688 \times 10^9$, $\alpha_{1111} = 7.59 \times 10^{10}$,

$\alpha_{1112} = -2.193 \times 10^{10}$, $\alpha_{1122} = -2.221 \times 10^{10}$, $\alpha_{1123} = 2.416 \times 10^{10}$, $Q_1 = 0.11$, $Q_2 = -0.045$, $Q_4 = 0.029$, $\kappa^b = 10$, $s_{11} = 9.1 \times 10^{-12}$, $s_{12} = -3.2 \times 10^{-12}$, $s_{44} = 8.2 \times 10^{-12}$ (in SI units) [28, 94-96].

The ferroelastic strains in the BaTiO₃ substrate include (1) the structural strain from the cubic to tetragonal phase transition that can be partly transferred to CoFe film during its growth [81]; and (2) the electric-field-induced strain during 90° ferroelectric domain switching [97], which normally can be fully transferred to the CoFe film [98, 99]. As mentioned above, spatial distribution of such ferroelastic strains will be used as the elastic boundary condition of the substrate (see discussion later) in Step 2 for simulating magnetic domain evolution in the CoFe film. The simulation zone of the film-substrate system (Fig. 3-1(b)) is discretized into a 3-dimensional array of 160×160×32 cells, wherein 12 layers of CoFe are placed over 15 layers of BaTiO₃ substrate and the uppermost 5 layers are air. The size of each cell is taken as 5×5×1 nm³, and hence the thicknesses of the CoFe film (i.e., h_f) and the top layers of BaTiO₃ substrate (i.e., h_s) are 12 nm and 15 nm, respectively. Three sets of order parameters are used to describe such CoFe/BaTiO₃ system, including a local polarization field $\mathbf{P}(\mathbf{x})$, a local magnetization field $\mathbf{M}(\mathbf{x}) = M_S \mathbf{m}(\mathbf{x})$ where M_S is the saturation magnetization and \mathbf{m} the normalized magnetization, and a phase field variable $\eta(\mathbf{x})$ describing the spatial distribution of the two phases, with $\eta(\mathbf{x}) = 1$ in the CoFe film and $\eta(\mathbf{x}) = 0$ in the BaTiO₃ substrate.

3.2.2 Phase-field model on the magnetic domains

The temporal evolution of the magnetization field is described by the Landau-Lifshitz-Gilbert equation, i.e.,

$$\left(1 + \alpha^2\right) \frac{\partial \mathbf{M}}{\partial t} = -\gamma_0 \mathbf{M} \times \mathbf{H}_{\text{eff}} - \frac{\gamma_0 \alpha}{M_S} \mathbf{M} \times (\mathbf{M} \times \mathbf{H}_{\text{eff}}), \quad (3-5)$$

where α is the damping constant, γ_0 is the gyromagnetic ratio, and \mathbf{H}_{eff} is the effective magnetic field, given by $\mathbf{H}_{\text{eff}} = -(1/\mu_0)(\delta F/\delta \mathbf{M})$. The free energy F for CoFe is calculated as $F = F_{\text{exch}} + F_{\text{ms}} + F_{\text{external}} + F_{\text{elastic}}$, where F_{exch} , F_{ms} , and F_{external} are the magnetic exchange energy, magnetostatic energy, and external magnetic field energy, respectively, with the same formulations as in Ref. [100]. The expression of elastic energy F_{elastic} is the same as Equation 3-4, but here the stress-free strain ε_{ij}^0 is written as,

$$\varepsilon_{ij}^0 = \begin{cases} \eta \left[\frac{3}{2} \lambda_s (m_i m_j - \frac{1}{3}) \right] + (1-\eta) Q_{ijkl} P_k P_l, & i = j \\ \eta \left(\frac{3}{2} \lambda_s m_i m_j \right) + (1-\eta) Q_{ijkl} P_k P_l, & i \neq j \end{cases} \quad (3-6)$$

where λ_s is the saturation magnetostriction, and the polarization field distribution \mathbf{P} relating to the ferroelastic strain $Q_{ijkl} P_k P_l$ is taken from that in the top few layers of the BaTiO₃ substrate from Step 1. The total strain is calculated as the sum of a homogeneous strain $\bar{\varepsilon}$ and a heterogeneous strain $\delta \varepsilon(\mathbf{x})$, i.e., $\varepsilon(\mathbf{x}) = \bar{\varepsilon} + \delta \varepsilon(\mathbf{x})$. Here $\bar{\varepsilon}$ (including $\bar{\varepsilon}_{11}$, $\bar{\varepsilon}_{22}$, and $\bar{\varepsilon}_{12}$) are calculated as $\bar{\varepsilon}_{ij} = \bar{\varepsilon}_{ij}^{\text{BTO}} - r_g \bar{\varepsilon}_{ij}^{\text{BTO,growth}}$ ($i, j=1,2$), where $\bar{\varepsilon}^{\text{BTO,growth}}$ and $\bar{\varepsilon}^{\text{BTO}}$ are the volume averages of the spatially varying strain $\varepsilon(\mathbf{x})$ within the top 15 layers of the BaTiO₃ substrate during film growth and under the applied electric field, respectively, taken from Step 1, and r_g is the fraction of the relaxed strain taken as 0.9 according to experimental measurements [81]. In doing so, both the partial relaxation of the initial structural strain during the magnetic thin film growth and the full transfer of electric-field-induced strain are incorporated. The heterogeneous strain $\delta \varepsilon$, the volume average of which is zero [100], is computed as,

$$\delta \varepsilon_{ij} = \frac{1}{2} \left(\frac{\partial u_i}{\partial x_j} + \frac{\partial u_j}{\partial x_i} \right). \quad (3-7)$$

Here $\mathbf{u}(\mathbf{x})$ is the spatial distribution of local displacements, which can be obtained by solving the elastic equilibrium equation $\partial\sigma_{ij}/\partial x_j = 0$, expanded as,

$$c_{ijkl} \frac{\partial^2 u_k}{\partial x_l \partial x_j} = c_{ijkl} \frac{\partial \mathcal{E}_{kl}^0}{\partial x_j}. \quad (3-8)$$

Note that a stress-free boundary condition is applied at the top surface of the film ($x_3 = h_f$, see Fig. 3-1(b)), i.e.,

$$c_{i3kl} \frac{\partial u_k}{\partial x_l} \Big|_{x_3=h_f} = c_{i3kl} \mathcal{E}_{kl}^0 \Big|_{x_3=h_f}, \quad (3-9)$$

while a displacement boundary condition is imposed at the bottom of the substrate ($x_3 = -h_s$, see Fig. 3-1), expressed as [30],

$$u_i \Big|_{x_3=-h_s} = u_i^{\text{BTO}} - r_g u_i^{\text{BTO,growth}} \quad (i=1,2,3), \quad (3-10)$$

where $\mathbf{u}^{\text{BTO,growth}}$ and \mathbf{u}^{BTO} are the displacement distributions in the top layers of the BaTiO₃ substrate during film growth and under the applied electric field, respectively. Equation 3-8 is solved by utilizing a superposition methodology [30]. The evolution of magnetic domains (Equation 3-5) is solved numerically using semi-implicit Fourier spectral method and Gauss-Seidel projection method [101]. Material parameters of CoFe are $M_s = 19.099 \times 10^5$, $\lambda_s = 1.39 \times 10^{-4}$, $\alpha = 0.025$, $c_{11} = 257 \times 10^9$, $c_{12} = 162 \times 10^9$, $c_{44} = 105 \times 10^9$ (in SI units) [102-104].

3.3 Results and discussion

3.3.1 Pattern copy between elastically coupled magnetic and ferroelectric domains

Utilizing the above-described phase-field model, we can easily reproduce the experimentally observed [78, 81] pattern copy between the elastically coupled magnetic and ferroelectric domains in the CoFe/BaTiO₃ heterostructure. As illustrated in in Fig. 3-2(a), alternating a_1 and a_2 in-plane ferroelectric domains with orthogonal polarizations are stabilized in the BaTiO₃ substrate before electric field poling, similar as those in experiments [78, 81, 82]. This pattern is precisely imprinted to the overlaying CoFe film during its growth through local elastic coupling. Such elastic modulation of the magnetic domains can be interpreted based on the difference between the two in-plane normal strain components, i.e., $\varepsilon_{11}-\varepsilon_{22}$, which determines the orientations of magnetic easy axes in the CoFe film. Specifically, an alternating distribution of positive and negative $\varepsilon_{11}-\varepsilon_{22}$ ($\sim 1\%$ and -1%) are generated corresponding to the alternating ferroelectric a_1 and a_2 domains in the BaTiO₃ substrate (see Fig. 3-2(b)), respectively, which are partly (10% [81] for $r_g=0.9$) transferred to the top CoFe film (see Fig. 3-2(c)). Such striped strain field induces the observed one-to-one match between the ferroelectric and magnetic domains [78, 81, 82], e.g., a_1 (ferroelectric) to a_1 (magnetic), and a_2 (ferroelectric) to a_2 (magnetic), due to the positive λ_S of Co_{0.6}Fe_{0.4} [105].

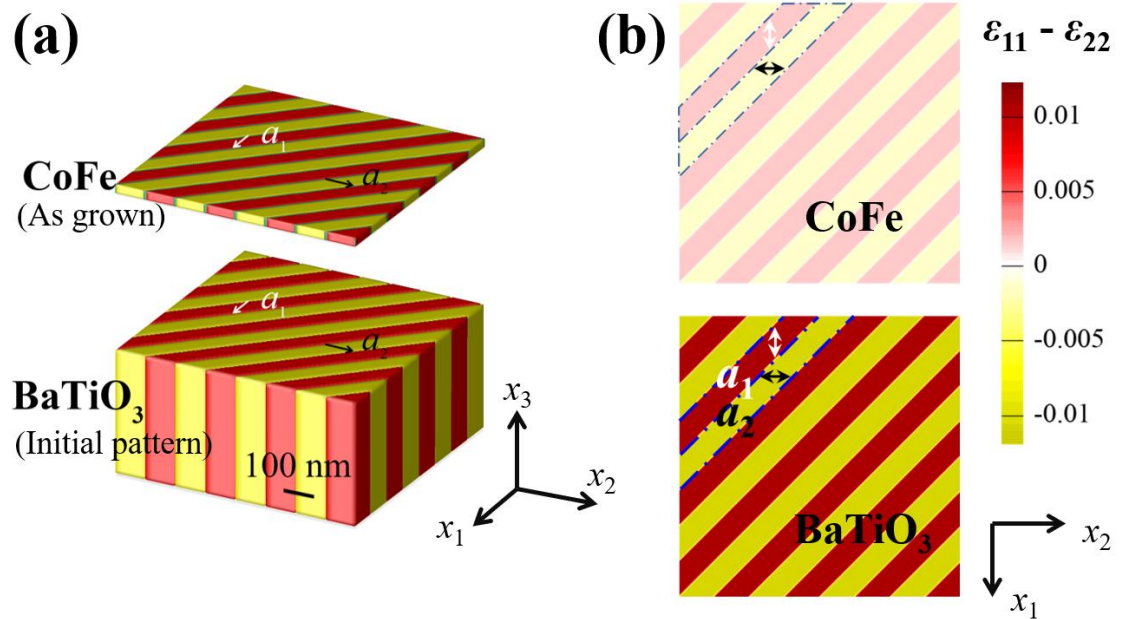


Figure 3-2. (a) Initial ferroelectric domain configuration of the BaTiO₃ substrate and magnetic domain configuration of the as grown CoFe film. The arrows indicate the directions of local polarization/magnetization vectors. Domain definitions and the corresponding polarizations/magnetizations: a_1 : $(P_1, 0, 0)$ or $(m_1, 0, 0)$; a_2 : $(0, P_2, 0)$ or $(0, m_2, 0)$; c : $(0, 0, P_3)$ or $(0, 0, m_3)$. (b) Corresponding distributions of the in-plane strain difference $\epsilon_{11} - \epsilon_{22}$ at the top surfaces of the original BaTiO₃ substrate and the CoFe film. The dashed lines indicate boundaries of the ferroelectric domains. The double-headed arrows indicate the elongated in-plane axes.

A theoretical examination of the magnetic domains in the as grown CoFe film through applying an in-plane magnetic field loop reveals perpendicular in-plane magnetic easy axes and correlated domain switching behavior of CoFe film regions on top of ferroelectric a_1 and a_2 domains, as seen in Fig. 3-3.

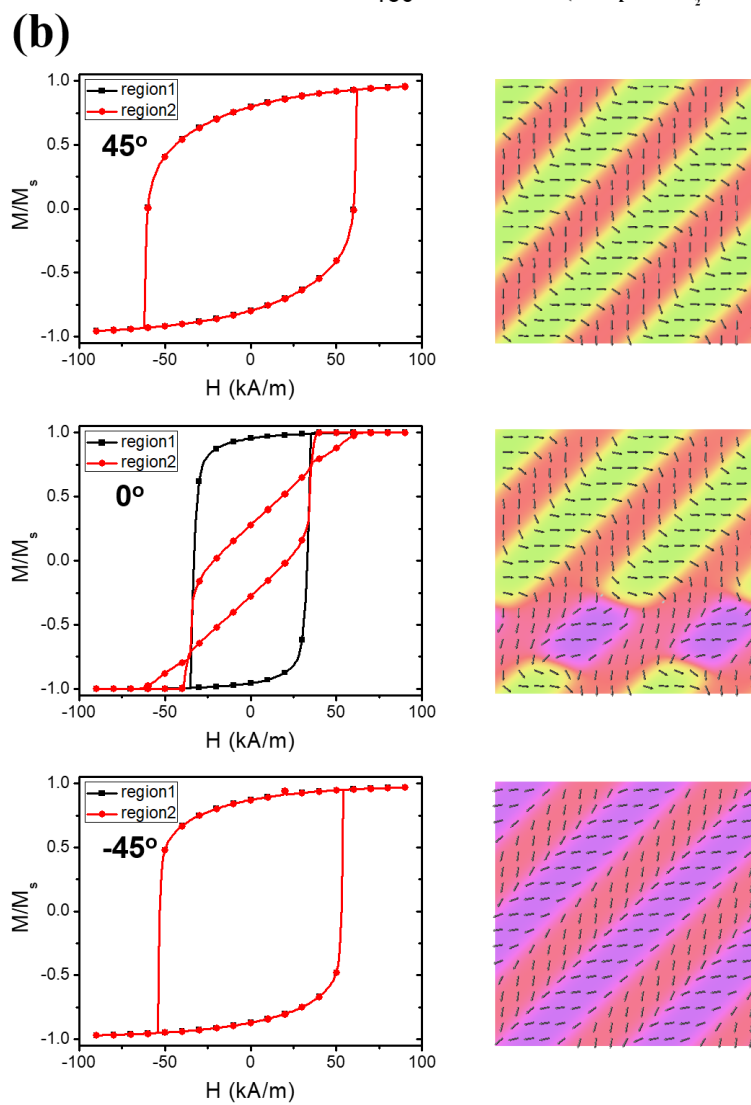
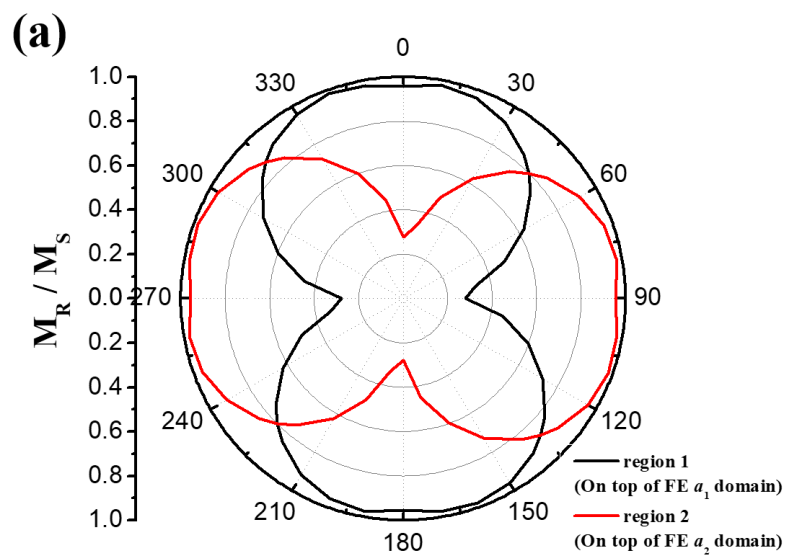


Figure 3-3. (a) Polar plot of the remnant magnetization M_R in regions on top of ferroelectric a_1 domains and regions on top of ferroelectric a_2 domains, respectively, on applying a magnetic field along in-plane direction. (b) (Left column) average magnetization response on applying a magnetic field loop along in-plane directions with angles $\theta=0^\circ$, $\theta=45^\circ$, and $\theta=-45^\circ$ with respect to the x_1 axis, respectively, and (right column) corresponding remnant magnetization configurations.

3.3.2 Electric field-manipulation of magnetic domain pattern

We next show the electric-field manipulation of magnetic domain pattern in such elastically coupled CoFe/BaTiO₃ heterostructure. An electric field along the out-of-plane x_3 direction, E_3 , is applied to the system, which cycles linearly between 0 and 600 kV/m at a rate of 7 kV/(m·ns). Upon increasing electric field, the initial in-plane a_1/a_2 stripe domains in the BaTiO₃ substrate gradually rotate off the plane and eventually become an out-of-plane c single domain at $E_3 = 600\text{kV/m}$ (see the second column in Fig. 3-4(a)). During this process, the strain field at the surface of BaTiO₃ changes from a striped pattern (see the first column in Fig. 3-4(b)) to an isotropic ($\varepsilon_{11}-\varepsilon_{22} \approx 0$) uniform distribution (see the second column in Fig. 3-4(b)), thereby the initial ferroelectric a_1 and a_2 domain regions undergoing the strain changes (i.e., $\Delta(\varepsilon_{11}-\varepsilon_{22})$) of about -1% and 1%, respectively. These electric-field-induced strain changes at the BaTiO₃ top surface are fully transferred to the overlaying CoFe film with an initial strain distribution shown in the first column in Fig. 3-4(c), resulting in a new striped strain field with $\varepsilon_{11}-\varepsilon_{22} \approx \mp 0.9\%$ as shown by the second column in Fig. 3-4(c). Accordingly, magnetic a_2 and a_1 domains are induced on top of the initial ferroelectric a_1 and a_2 domain regions, respectively, leading to a pattern interchange of the original magnetic a_1 and a_2 domain regions (see the second column in Fig. 3-4(a)).

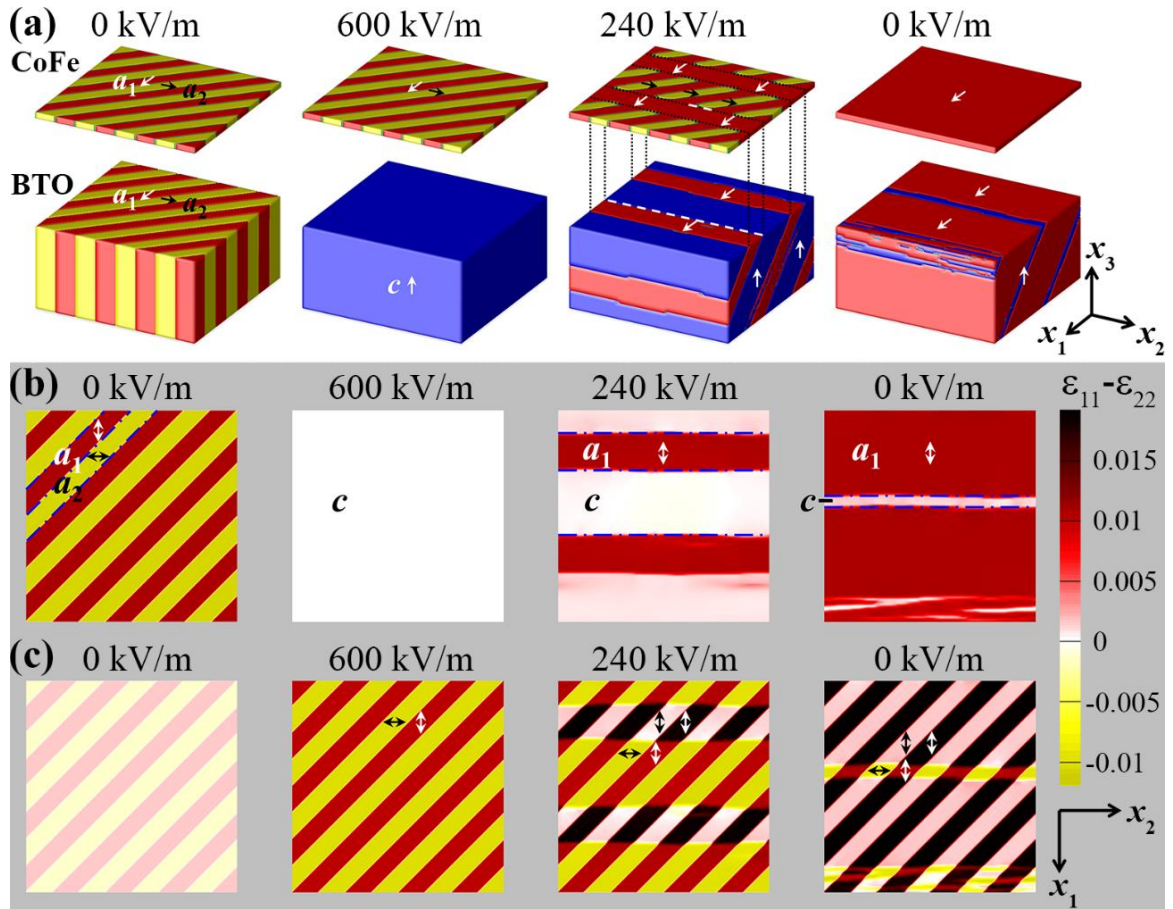


Figure 3-4. (a) Ferroelectric domain configuration of the BaTiO₃ substrate and magnetic domain configuration of the CoFe film upon increasing E_3 from 0 (first column) to 600kV/m (second column), followed by reducing E_3 to 240kV/m (third column) and then to 0 (fourth column). The arrows indicate the directions of local polarization/magnetization vectors. Domain definitions and the corresponding polarizations/magnetizations: a_1 : $(P_1, 0, 0)$ or $(m_1, 0, 0)$; a_2 : $(0, P_2, 0)$ or $(0, m_2, 0)$; c : $(0, 0, P_3)$ or $(0, 0, m_3)$. Corresponding distributions of the in-plane strain difference $\epsilon_{11} - \epsilon_{22}$ at (b) the top surfaces of the original BaTiO₃ substrate and (c) the CoFe film. The dashed lines indicate boundaries of the ferroelectric domains. The double-headed arrows indicate the elongated in-plane axes.

Subsequent decrease of E_3 induces the formation and growth of in-plane ferroelectric a_1 domains in the BaTiO₃ substrate, presenting a multi-domain a_1/c structure (see the third column in Fig. 3-4(a)). The development of ferroelectric a_1 domains is associated with an in-plane strain change, $\Delta(\epsilon_{11} - \epsilon_{22})$, of 1.0%, leading to the striped strain field of $\epsilon_{11} - \epsilon_{22} \approx 0.1\%$ and 1.9% within the regions of initial ferroelectric a_1 and a_2 domains at the BaTiO₃ surface, respectively (see the third

column in Fig. 3-4(b)). The corresponding strain distribution in CoFe film is illustrated by the third column in Fig. 3-4(c), where variations take place on top of the newly-developed ferroelectric a_1 domain and would favor an alignment of a magnetic a_1 domain as $\lambda_S > 0$. By contrast, the magnetic stripe domain on top of ferroelectric c domains is preserved, leading to a mixed a_1 and striped a_1/a_2 domain pattern in the CoFe film (see the third column in Fig. 3-4(a)).

As E_3 further decreases, the induced magnetic a_1 domain keeps growing with the expansion of its elastically coupled ferroelectric a_1 domain underneath, eventually exhibiting a magnetic a_1 single domain at $E_3 = 0$ (see the fourth column in Fig. 3-4(a)). An increase of E_3 back to 600kV/m brings back the magnetic a_1/a_2 stripe domain in CoFe film and the ferroelectric c single domain in BaTiO₃ substrate exactly as shown by the second column in Fig. 3-4(a). Such repeatable electric-field writing and erasure of magnetic striped a_1/a_2 domains have been demonstrated by experimental observations [81].

3.3.3 Domain evolution kinetics

A close examination on the kinetics of the magnetic domain evolution reveals an alternating occurrence of local magnetization rotation and domain wall motion associated with the ferroelectric domain evolution. In the downhill electric-field cycle, when the width of the newly-formed ferroelectric a_1 domains is small, the magnetic stripe pattern remains unchanged i.e., new magnetic a_1 domain does not form on top of the ferroelectric a_1 domain. When the underlying ferroelectric a_1 domain reaches a critical width of around 70 nm at $E_3 = 280$ kV/m, the magnetic striped a_1/a_2 domain above ferroelectric a_1 domain starts transforming into a magnetic a_1 domain through a coherent magnetization rotation of 90° (see Fig. 3-5(a)) as the ferroelastic strain-induced magnetic anisotropy is sufficiently large to overcome the exchange and

magnetostatic energy penalty. Detailed magnetic free energy analysis for such finite-size scaling of domain pattern transfer has been reported in a recent study [85].

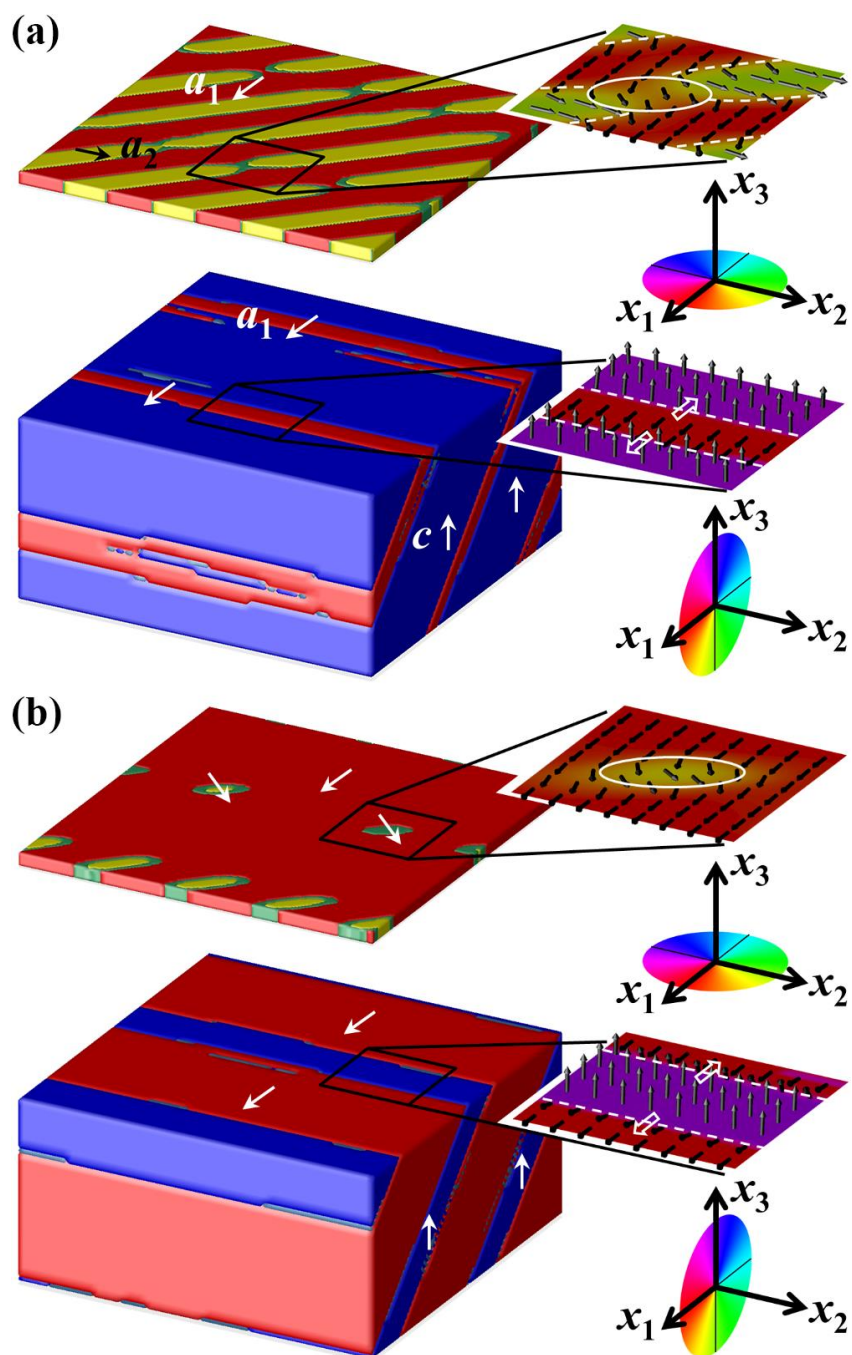


Figure 3-5. Magnetic and ferroelectric domain structures at (a) $E_3 = 280\text{kV/m}$ and (b) $E_3 = 110\text{kV/m}$ in a downhill electric-field cycle. (Right columns) close-up vector plots of the

polarization and magnetization configuration within the selected areas; the white dashed lines and the hollow arrows indicate the domain wall and the direction of the domain wall motion, respectively; the white solid circles indicate the regions undergoing magnetization rotation.

Such transformation from local magnetic a_1/a_2 to a_1 domain is complete as the E_3 decreases to 260 kV/m, at which the newly-developed magnetic a_1 domain are wider and gets coupled to the underlying ferroelectric a_1 domain. From the moment on, the evolution of the mixed a_1 and a_1/a_2 magnetic domains closely tracks the ferroelectric domain evolution through the motion of the elastically coupled magnetic and ferroelectric domain walls. For illustration, we select a certain magnetic a_1/a_2 domain wall and the associated ferroelectric a_1/c domain wall (as indicated by the white dashed lines in the third column of Fig. 3-4(a)) and track their velocities along the x_1 direction, as demonstrated in Fig. 3-6(a). The domain wall positions are located where $P_1 = P_3$ for a ferroelectric a_1/c domain wall and $m_1 = m_2$ for a magnetic a_1/a_2 domain wall (as an example, see Fig. 3-6(b) for the domain wall configurations at $E_3 = 240$ kV/m). As seen, the velocity of the magnetic a_1/a_2 domain wall is almost identical to the ferroelectric domain wall from $E_3 = 250$ kV/m to $E_3 = 130$ kV/m (see the region encircled by dash-dotted lines in Fig. 3-6(a)). Upon further reducing E_3 from 130 kV/m when the width of ferroelectric c domains reduces to about 110 nm, the a_2 domain rapidly shrinks, becoming decoupled from the underlying ferroelectric c domains due to the reduction of the ferroelastic strain-induced magnetic anisotropy. Such decoupling of magnetic a_2 and ferroelectric c domain is another manifestation of the finite-size scaling of the domain pattern transfer besides the onset of magnetic a_1 -to-ferroelectric a_1 domain coupling at $E_3 = 260$ kV/m. Indeed, the local a_2 domain starts transforming into a magnetic a_1 domain through a coherent magnetization rotation (e.g., see Fig. 3-5(b) at which $E_3 = 110$ kV/m) and eventually vanishes, creating a uniform a_1 single domain in the whole

CoFe film. Similar domain evolution behaviors are observed in the subsequent uphill electric-field cycle.

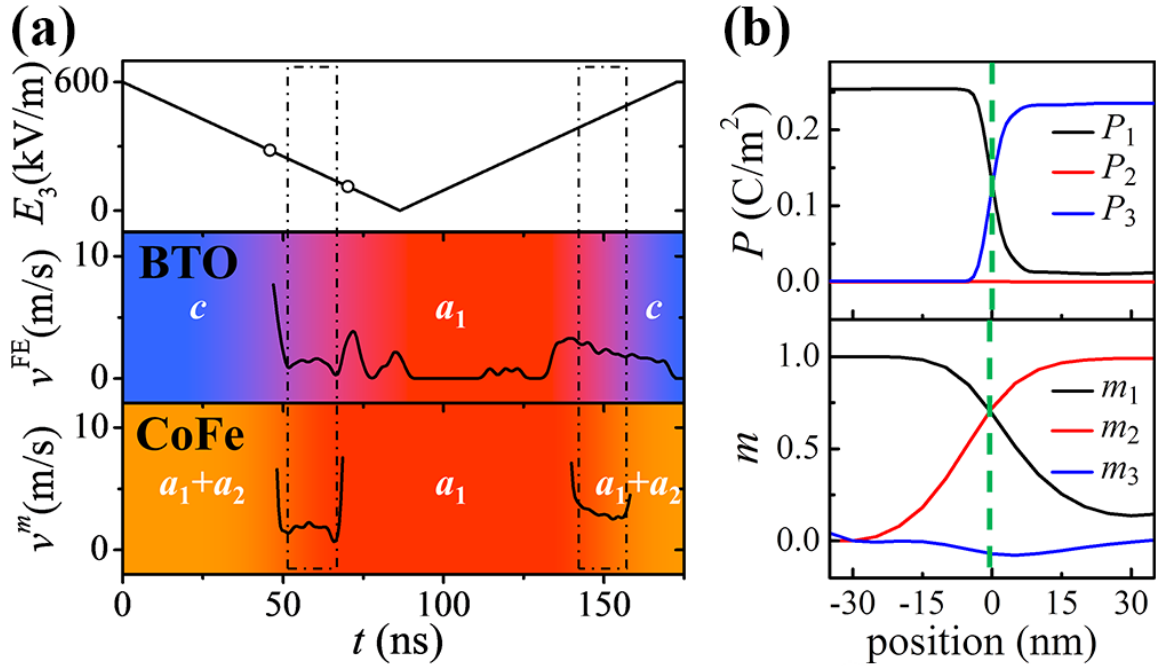


Figure 3-6. (a) (Top) time sequence of the applied out-of-plane electric field E_3 , and the velocities of (middle) ferroelectric and (bottom) magnetic domain wall motion, in ferroelectric a_1/c domain and mixed a_1 and a_1/a_2 magnetic domain configurations, respectively. The regions encircled by dash-dotted lines indicate the coupled domain wall motion, and the background colors indicate the dominant ferroelectric or magnetic domains at various stages. (b) (Top) polarization and (bottom) magnetization configurations across the selected ferroelectric and magnetic domain walls, respectively, at $E_3 = 240$ kV/m in the downhill cycle. The dashed lines indicate the domain wall positions.

3.4 Conclusion

In this chapter, a phase-field model has been developed to study the local elastic coupling behaviors of the magnetic and ferroelectric domains in a multiferroic heterostructure of a magnetic film grown on a ferroelectric substrate. Taking a polycrystalline CoFe and a BaTiO₃

crystal as an example, the one to one match of the initial magnetic and ferroelectric domain structures and the repeated electric-field writing and erasure of the magnetic striped domains have been simulated, providing modeling supplement and theoretical insights to experimental observations. Studies on the kinetics of the electric-field driven magnetic domain evolution reveal an alternating occurrence of local magnetization rotation and the coupled motion of magnetic and ferroelectric domain walls with almost identical velocities.

Chapter 4

Phase-field study on an anomalous negative electrocaloric effect in a ferroelectric/relaxor composite

4.1 Introduction

The electrocaloric effect is a phenomenon in which a dielectric material absorbs or releases heat in response to an applied electric field [106-111]. It originates from the electro-thermal coupling and is considered as the converse effect of pyroelectricity. The electrocaloric-effect-induced cooling shows high energy efficiency and is promising for next-generation environmental-friendly cooling technologies with improved efficiency and low cost [110, 111]. It has been experimentally demonstrated that electrocaloric effect can be tuned through ferroelectric or dielectric composite design [112-114].

An electrocaloric material will absorb (or release) heat if dipolar entropy is increased (or decreased). As shown in Fig. 4-1, applying an electric field would, in most cases, align the dipoles (i.e., ordered dipoles) and decrease the dipolar entropy inducing heating, and removing the field would increase the dipolar entropy (disordered dipoles) inducing cooling. However, in some cases [115-117], applying an electric field may also decrease the dipolar entropy leading to cooling, and removing the field would induce heating, which phenomenon is called a negative electrocaloric effect. Furthermore, our experimental collaborators X. Qian, Q. Zhang et al. report an anomalous negative electrocaloric effect in P(VDF-TrFE)/P(VDF-TrFE-CFE) normal ferroelectric/ relaxor polymer composites which shows cooling upon applying an electric field without subsequent heating on removing the field [118]. The phenomenon indicates that the applied field induces disordered dipoles in the composite with an increased dipolar entropy,

which structure remains stable upon removing the field. Such cooling effect can work on-demand with an instant cooling pulse, which is promising in some applications such as on-chip hotspot striking.

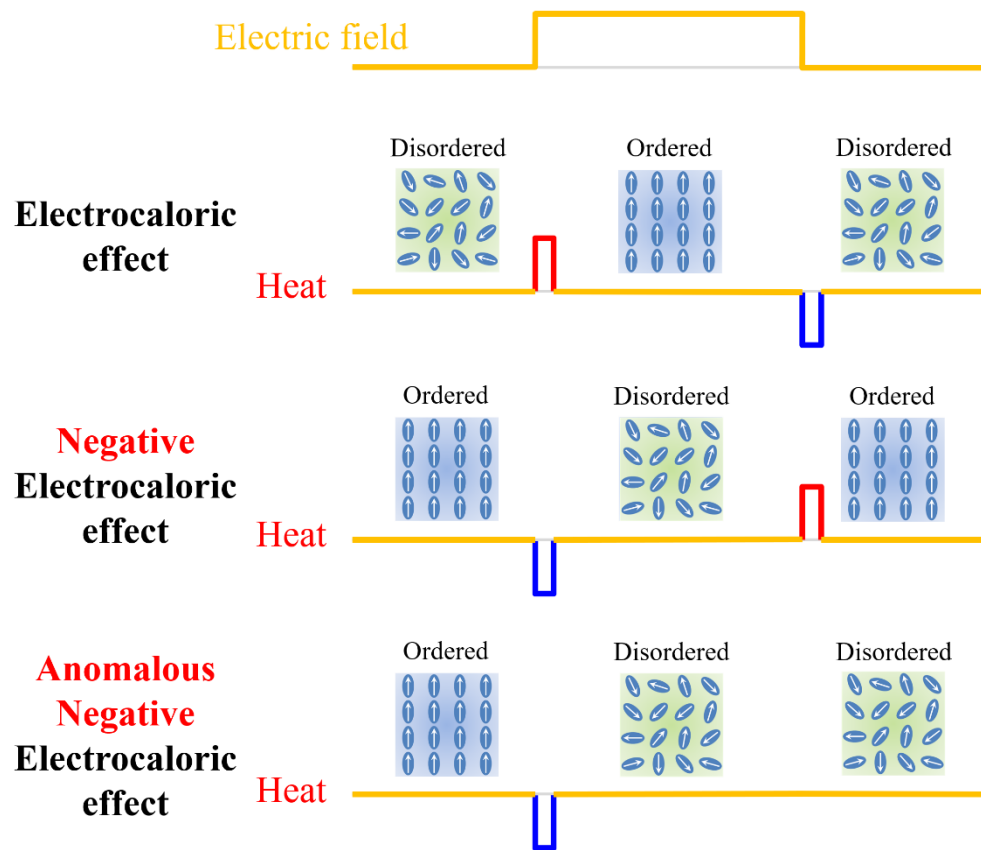


Figure 4-1. Dipole ordering and electrocaloric heat upon applying and removing an electric field for the normal electrocaloric effect, negative electrocaloric effect, and the anomalous negative electrocaloric effect.

Phase-field model is a powerful tool for studying microstructure evolution during phase transformation and predicting material properties, which has been applied to study ferroelectric materials [24, 30] and heterostructures [119, 120] based on Landau theory of phase transformations and time-dependent Ginzburg-Landau equation. In the present work, we employ

a phase-field model and thermodynamic analyses to verify the electric-field control on the dipole ordering in such ferroelectric composites and study the anomalous negative electrocaloric effect and its dependence on the temperature and the applied field.

4.2 Model and simulation method

4.2.1 Phase-field model on the ferroelectric domain evolution

To model the evolution of polarization and domain structure in the P(VDF-TrFE)/P(VDF-TrFE-CFE) composite, two sets of position-dependent order parameters are used to describe the microstructure, including a non-evolving $\eta(\mathbf{x})$ for the two-phase structure, with $\eta(\mathbf{x}) = 1$ for the P(VDF-TrFE) phase and $\eta(\mathbf{x}) = 0$ for the P(VDF-TrFE-CFE) phase, respectively, and the electric polarization $\mathbf{P}(\mathbf{x}, t)$ describing the ferroelectric domain structure in P(VDF-TrFE), where \mathbf{x} is the position vector, and t is the time.

The evolution of electric polarization in the composite responsive to an applied electric field is modeled through solving the time-dependent Ginzburg-Landau equation (Equation 1-1) by employing a semi-implicit Fourier-spectral method [26]. In evaluating total free energy of the system, the Landau free energy, the polarization gradient energy, and the electrostatic energy are considered, i.e.,

$$F(\mathbf{P}, \mathbf{E}, T) = \int \left[\eta \left(f_{\text{Landau}}^C + f_{\text{gradient}}^C \right) - (1 - \eta) \left(f_{\text{Landau}}^T + f_{\text{gradient}}^T \right) - \mathbf{P} \cdot \mathbf{E}^{\text{ext}} + \frac{1}{2} \varepsilon_0 \kappa_b \mathbf{E}^{d2} \right] d\mathbf{x}^3 \quad (4-1)$$

where superscripts C and T stand for the P(VDF-TrFE) copolymer and P(VDF-TrFE-CFE) terpolymer phases, respectively. The Landau potential is considered anisotropic and is expanded to a 6th-order polynomial as

$$f_{\text{Landau}}^C(\mathbf{P}) = a_1^C \mathbf{P}^2 + a_{11}^C \mathbf{P}^4 + a_{111}^C \mathbf{P}^6 \quad (4-2)$$

for the normal ferroelectric copolymer P(VDF-TrFE) and to a 2nd-order polynomial as

$$f_{\text{Landau}}^T(\mathbf{P}) = \mathbf{P}^2 / (2\kappa_0\kappa_r^T) \quad (4-3)$$

for the relaxor terpolymer P(VDF-TrFE-CFE), respectively; a and κ_r are the Landau energy coefficients and the relative dielectric permittivity, respectively. The distribution of electric field \mathbf{E} upon polarization evolution is obtained by solving the electrostatic Poisson equation $\nabla \cdot (\kappa_0\mathbf{E} + \mathbf{P}) = 0$ using a Fourier-spectral method [29]. Materials constants of P(VDF-TrFE) and P(VDF-TrFE-CFE) are listed in Table 4-1.

Table 4-1. Material constants of P(VDF-TrFE) and P(VDF-TrFE-CFE).

Material Constant	Unit	P(VDF-TrFE)	P(VDF-TrFE-CFE)
a_1	$\text{N}\cdot\text{m}^2/\text{C}^2$	$1.412 \times 10^7 (T/^\circ\text{C} - 36.8)$	$(2\kappa_0\kappa_{r11})^{-1}$
a_{11}	$\text{N}\cdot\text{m}^6/\text{C}^4$	-1.842×10^{11}	0
a_{111}	$\text{N}\cdot\text{m}^{10}/\text{C}^6$	2.585×10^{13}	0
g_{11}	$\text{N}\cdot\text{m}^4/\text{C}^2$	5×10^{-7}	0
g_{44}	$\text{N}\cdot\text{m}^4/\text{C}^2$	2.5×10^{-7}	0
g_{44m}	$\text{N}\cdot\text{m}^4/\text{C}^2$	2.5×10^{-7}	0
κ_{r11}	1	/	$8.8 - 0.412(T/^\circ\text{C}) - 6.20 \times 10^{-3}(T/^\circ\text{C})^2 + 5.26 \times 10^{-5}(T/^\circ\text{C})^3$ ($15^\circ\text{C} \leq T \leq 70^\circ\text{C}$)

The Landau energy coefficients of ferroelectric P(VDF-TrFE) with composition 65/35mol% are obtained from fitting experimental measurements on the temperature-dependent spontaneous polarization and coercive field of pure P(VDF-TrFE) (Table 4-1). The fitted Curie-Weiss temperature of pure P(VDF-TrFE) is 42°C. We employed the fitted Landau energy coefficients to a phase-field simulation on the P-E loops of pure P(VDF-TrFE) at different temperatures. As seen in Fig. 4-2, a square-shaped P-E loop characteristic of a normal ferroelectric phase is described. The temperature dependence of dielectric permittivity of P(VDF-

TrFE-CFE) is fitted to a 3rd-order polynomial from the experimentally measured dielectric permittivity at $15^{\circ}\text{C} \leq T \leq 70^{\circ}\text{C}$ (Table 4-1).

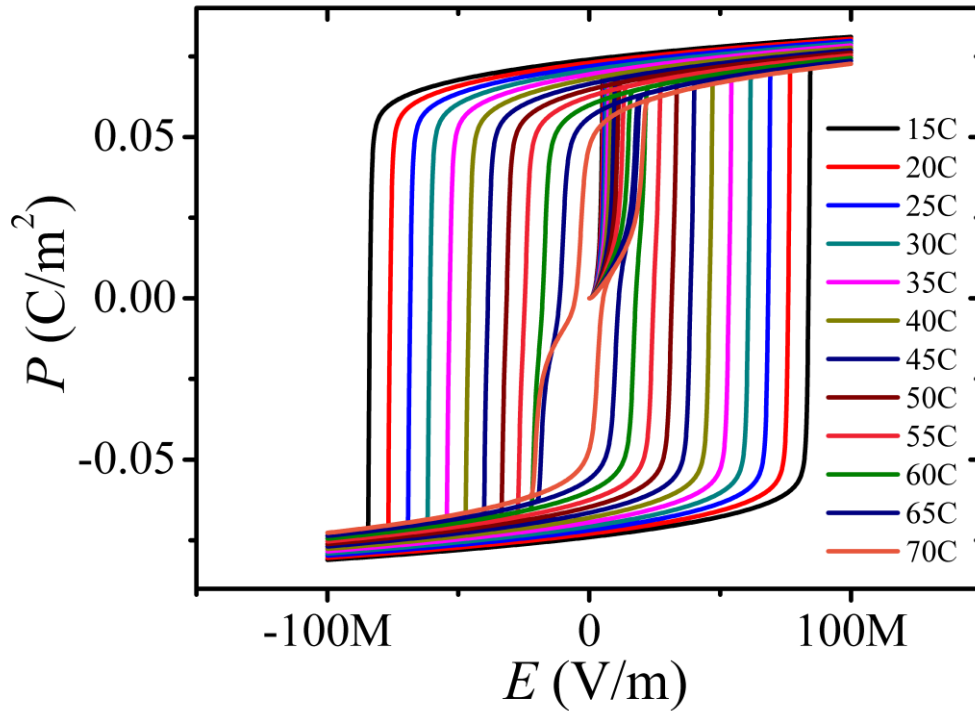


Figure 4-2. P-E loops of pure P(VDF-TrFE) at temperatures $15^{\circ}\text{C} \leq T \leq 70^{\circ}\text{C}$, from the phase-field simulation.

4.2.2 Calculation of electrocaloric effect

To calculate the electrocaloric-induced change in temperature and entropy based on the simulated response of domain structures with a phase-field model, a thermodynamic scheme is employed in the present work. As a matter of fact, phase-field model explicitly considers the free energy of the system, which allows convenient evaluation of the electrocaloric-induced change in

entropy and system temperature during domain evolution. The entropy density, i.e., entropy per unit volume, of a system contributed by the polarization order is calculated as

$$S = - \left(\frac{\partial f}{\partial T} \right)_{\mathbf{E}^{\text{ext}}} \quad (4-4)$$

where $f(\mathbf{P})$ is the free energy density caused by the polarization order, expressed as

$$f = f_{\text{Landau}} + \frac{1}{2} \varepsilon_0 E^{d2} - \mathbf{P} \cdot \mathbf{E}^{\text{ext}} \quad (4-5)$$

The change of entropy density of the system in a process is

$$\Delta S = \Delta \left(- \frac{\partial f}{\partial T} \right) = - \frac{\partial \Delta f}{\partial T} \quad (4-6)$$

Following Equation 4-6, the electrocaloric-induced entropy change of a system at isothermal condition (constant temperature) can be calculated through tracking the free energy change of a process and then calculate the shift of such free energy change within the same process (i.e., the same external field sequence) at a slightly different temperature (by 1K in the present work), i.e.,

$$\Delta S = - \frac{\Delta f(T_1) - \Delta f(T_2)}{T_1 - T_2} \quad (4-7)$$

Such isothermal entropy change, however, does not solely determine the heat released to the environment during isothermal processes. In ferroelectric systems, the evolution of ferroelectric domains under an external field may involve irreversible processes, including domain switching and domain wall motion, i.e., the change in the total entropy of the system and the environment $\Delta S_{\text{total}} > 0$. ΔS_{total} is related to the heat produced due to the irreversible process, Q_{irr} , i.e.,

$$\Delta S_{\text{total}} = \frac{Q_{\text{irr}}}{T} \quad (4-8)$$

Here Q_{irr} can be evaluated using the first law of thermodynamics, i.e., based on the work done by external electric field, and the change of the internal energy density of the system, with the following relation:

$$Q_{\text{irr}} = \int \mathbf{E}^{\text{ext}} \cdot d\mathbf{P} - \Delta f_{\text{int}} \quad (4-9)$$

where the internal energy density f_{int} is expressed as

$$f_{\text{int}} = f + \mathbf{P} \cdot \mathbf{E}^{\text{ext}} = f_{\text{Landau}} + \frac{1}{2} \epsilon_0 E^2 \quad (4-10)$$

Using Equation 4-10, we can also rewrite Equation 4-9 as

$$Q_{\text{irr}} = -\int \mathbf{P} \cdot d\mathbf{E}^{\text{ext}} - \Delta f \quad (4-11)$$

Equation 4-11 is used in the present work to calculate Q_{irr} of any processes. In an isothermal process, the heat release to the environment can be expressed as

$$Q = -T\Delta S + Q_{\text{irr}} \quad (4-12)$$

Alternatively, under an adiabatic condition, the temperature change of the system is calculated as

$$\Delta T \approx \frac{1}{VC_P} \int Q dV = \frac{1}{VC_P} \int (-T\Delta S + Q_{\text{irr}}) dV \quad (4-13)$$

where C_P is the heat capacity of the system at a fixed pressure and fixed polarization order, and V is the volume of the system. A small temperature change ($\Delta T \ll T$) is assumed herein. Equation 4-13 is adopted in the present work in evaluating the electrocaloric-effect-induced temperature change.

Note that the Maxwell-relation

$$\left(\frac{\partial S}{\partial \mathbf{E}} \right)_T = \left(\frac{\partial \mathbf{P}}{\partial T} \right)_E \quad (4-14)$$

were also used in some studies for theoretical calculations of electrocaloric effect, where the entropy change is expressed as

$$\Delta S = \int_0^{\mathbf{E}} \left(\frac{\partial S}{\partial \mathbf{E}} \right)_T \cdot d\mathbf{E} = \int_0^{\mathbf{E}} \left(\frac{\partial \mathbf{P}}{\partial T} \right)_\mathbf{E} \cdot d\mathbf{E} \quad (4-15)$$

Equation 4-15 indicates that the electrocaloric-effect-induced entropy change can be calculated by tracking the temperature-dependence and electric-field-dependence of the net polarization of the system. However, the Maxwell-relation fails to consider the inhomogeneous distribution of local polarization as well as heat generated in the irreversible processes as discussed above, and hence Equation 4-15 should not be applied to calculate the entropy change of processes which contains irreversible processes of ferroelectric domain evolution, e.g., domain switching, and is not adopted in the present work.

4.2.3 Simulation setup

In the phase-field simulation, the total size of the simulation system is taken as $4 \times 2 \mu\text{m}^2$, which is discretized into a 2-dimensional array of 800×400 grid points. The two-phase structure is generated by a phase-separation simulation using a spinodal free energy potential, where each phase takes a 50% volume fraction, with connected stripe patterns with 70~150 nm in width, as shown in Fig. 4-3. A sharp two-phase interface is adopted.



Figure 4-3. Spatial distribution of the two-phase structure of the P(VDF-TrFE)/P(VDF-TrFE-CFE) composite with a 50/50vol% phase fraction. P(VDF-TrFE) is shown by the white regions, while P(VDF-TrFE-CFE) is shown by the black regions.

4.3 Results and discussion

4.3.1 Ferroelectric properties of the composite

The simulated P-E loops of the P(VDF-TrFE)/P(VDF-TrFE-CFE) 50/50vol% composite at different temperatures is shown in Fig. 4-4, showing a mixed behavior of normal ferroelectric materials and ferroelectric relaxors. At room temperature ($T = 25^{\circ}\text{C}$), the composite shows a strong remnant polarization $P_R = 0.042\text{C/m}^2$ and a large coercive field $E_C = 35\text{MV/m}$, exhibiting the normal ferroelectric behavior similar to that of the P(VDF-TrFE) component. On the other hand, on increasing the temperature, the composite shows a gradual transition from a normal ferroelectric to a relaxor (or dielectric material) with narrower hysteresis loops, and exhibits the

relaxor (or dielectric) behavior of the P(VDF-TrFE-CFE) component at $T=70^{\circ}\text{C}$, with a greatly reduced remnant polarization $P_R=0.004\text{C}/\text{m}^2$ and a weak coercive field $E_C=10\text{MV}/\text{m}$.

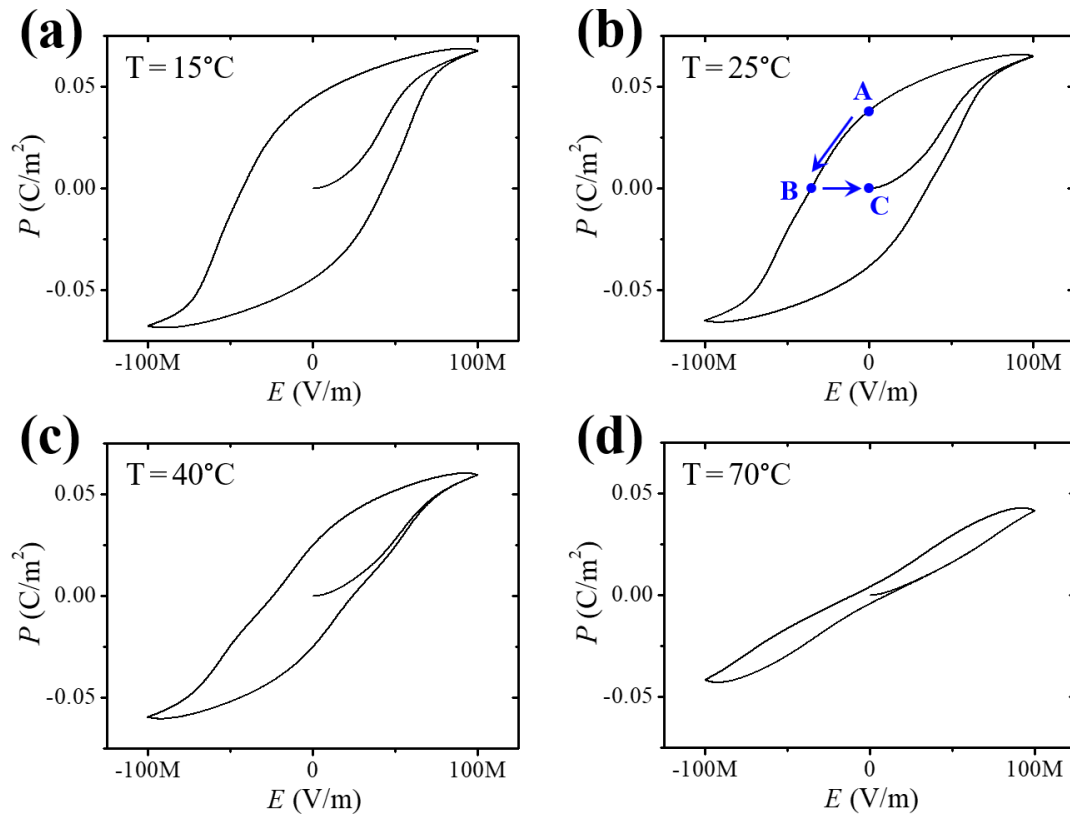


Figure 4-4. Simulated P-E loops of the P(VDF-TrFE)/P(VDF-TrFE-CFE) 50/50vol% with a $E=100\text{MV}/\text{m}$ poling field, at (a) 15°C , (b) 25°C , (c) 40°C , and (d) 70°C , respectively, showing the transition from a normal ferroelectric material with strong remnant polarization and coercive field in the P-E loop, to a relaxor (or dielectric material) with smaller hysteresis upon increasing the temperature.

4.3.2 Anomalous electrocaloric effect

Cooled from high temperature to the room temperature, the composite exhibits disordered polarization directions without an external electric field due to the relaxor nature of the

terpolymer component. A poling electric field aligns the polarization direction and generates a quasi-single domain which is stabilized by the copolymer phase upon removing the field. As seen in the top panel of Fig. 4-5, at room temperature, the remnant state after poling at $E_3 = 100\text{MV/m}$ shows a ferroelectric quasi-single domain with aligned polarization along the previous poling direction x_3 (indicated by point A in Fig. 4-4(b)). This is referred to as the poled state.

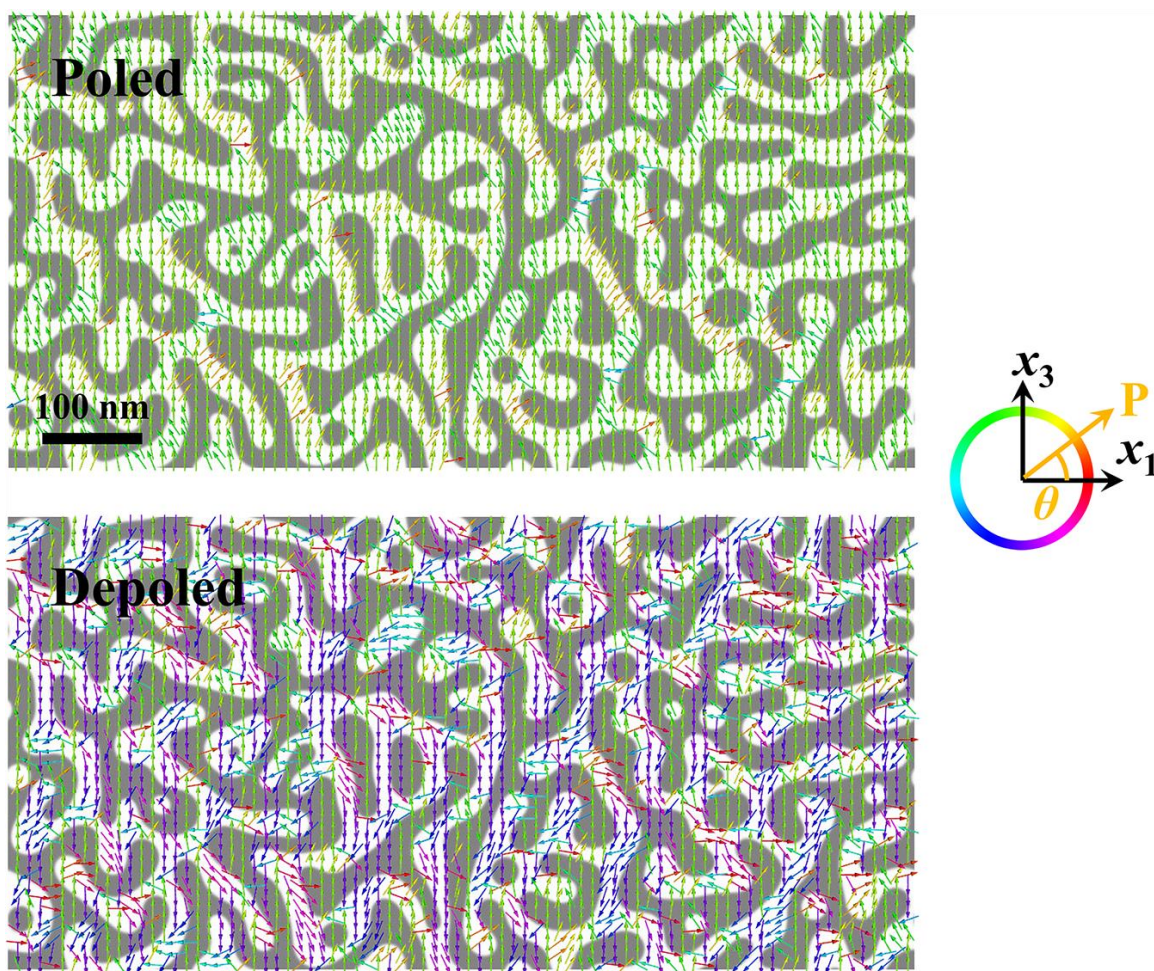


Figure 4-5. Simulated spatial map of the polarization vectors in the room temperature P(VDF-TrFE)/P(VDF-TrFE-CFE) 50/50vol% composite, at remnant states (top panel) after poling with $E_3 = 100\text{MV/m}$, and (bottom panel) after subsequent depoling with $E_3 = -35\text{MV/m}$, respectively. The light and dark backgrounds indicate regions of the P(VDF-TrFE) and P(VDF-TrFE-CFE) phases, respectively.

The remnant polarization in the ferroelectric copolymer generates a strong electric field along the previous poling direction in the adjacent terpolymer relaxor phase, stabilizing and aligning the polarization in the relaxor phase. As a result, the poled composite exhibits a strong alignment of electric dipoles around direction $\theta = 90^\circ$, the poling direction, which is also shown by the probability distribution of the polarization directions θ in the terpolymer phase in Fig. 4-6(a). Such ordering of electric dipoles indicates a low dipolar entropy state with potential cooling effect upon subsequent depoling.

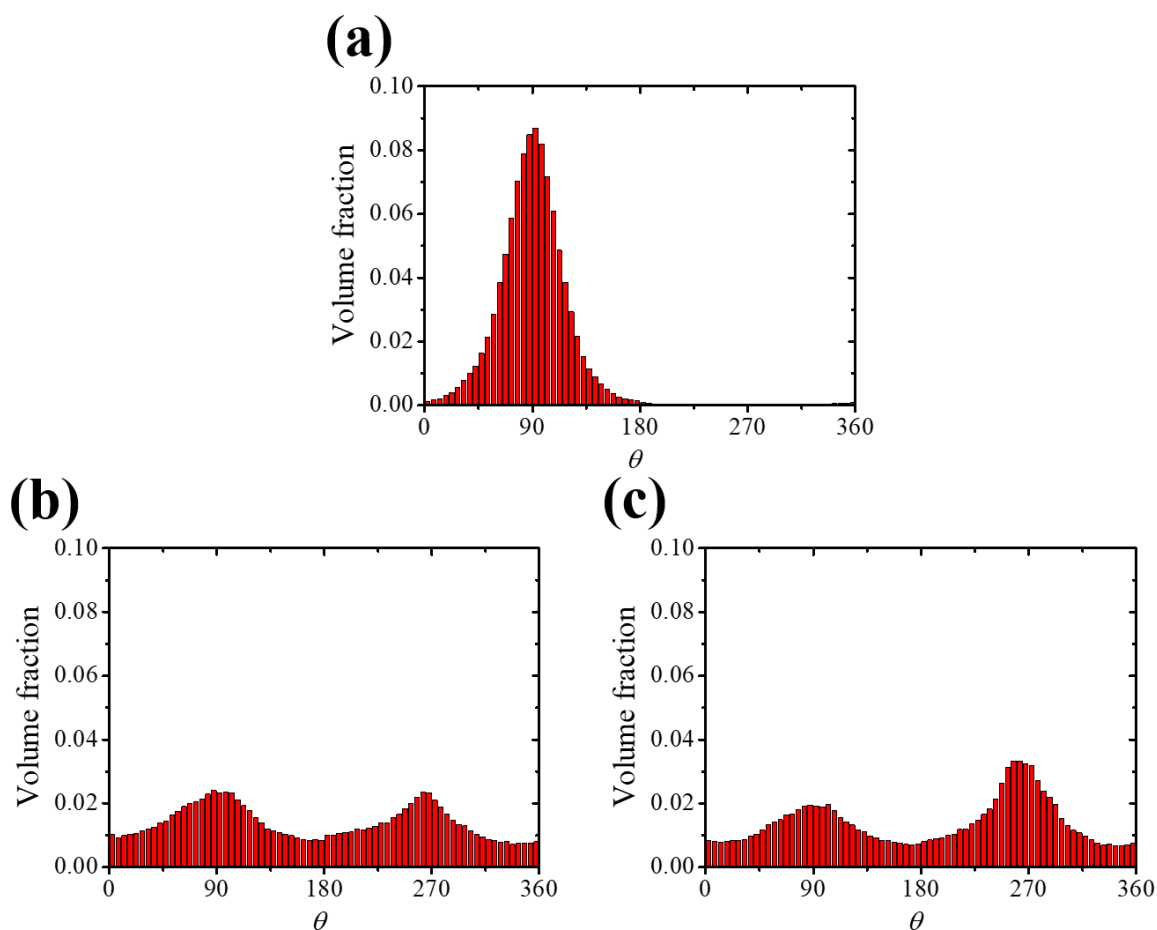


Figure 4-6. Simulated probability distribution of the orientation θ of polarization vectors inside the P(VDF-TrFE-CFE) relaxor phase, (a) at remnant states after poling with $E_3 = 100\text{MV/m}$, and after subsequent depoling with (b) $E_3 = -35\text{MV/m}$ and (c) $E_3 = -40\text{MV/m}$, respectively, of the room temperature P(VDF-TrFE)/P(VDF-TrFE-CFE) 50/50vol% composite.

The anomalous electrocaloric effect occurs upon subsequent depoling of such poled state with dipole ordering. On applying an increasing external field opposite the poling direction, the macroscopic polarization undergoes a continuous decrease with a steady slope on the P-E loop (Fig. 4-4(b)), showing a mixed behavior of normal ferroelectric materials and ferroelectric relaxors, where domain switching in P(VDF-TrFE) is buffered by the interaction of polar nanoregions in the P(VDF-TrFE-CFE) relaxor phase. With increasing external field, locally switched domains form and continuously expand, hence showing a continuous decrease of macroscopic polarization of the composite.

Upon increasing the depoling field to the coercive field value $E_3 = -35\text{MV/m}$, the composite is fully depoled with almost zero macroscopic polarization (indicated by point B in Fig. 4-4(b)). A disordered domain state is generated where the random dipole arrangement is stabilized by the P(VDF-TrFE-CFE) relaxor phase, due to the intrinsic polar nanoregions of the relaxor. Such disordered domain structure remains stable after the depoling field is removed (indicated by point C in Fig. 4-4(b)), as seen in the bottom panel of Fig. 4-5, referred to as the depoled state. The depoled state contains randomly oriented dipoles which are almost uniformly distributed in all directions, as shown by the probability distribution of polarization directions θ in Fig. 4-6(b).

Such disordering in dipoles upon depoling the composite induces a significant cooling through electrocaloric effect. By applying a thermodynamic calculation (Equation 4-13), the depoling process with an electric field pulse of $E = 30\text{MV/m}$ generates an adiabatic cooling of $\Delta T = -2.6^\circ\text{C}$ through the electrocaloric effect, which quantitatively agrees with the experimental measurement of $\Delta T = -2.1^\circ\text{C}$ [118].

4.3.3 Dependence of the electrocaloric effect on temperature and electric field

We next come to investigate the influence of operating temperature and electric field magnitude on the anomalous electrocaloric effect. As seen in Fig. 4-7, at $T = 25^\circ\text{C}$, with increasing magnitude of the depoling electric field pulse, the electrocaloric-induced cooling temperature ΔT increases upon formation of depoled ferroelectric domain structure and disordered electric dipoles, with a maximum $\Delta T = -2.6\text{K}$ at around $E = 31\text{MV/m}$, which is close to the coercive field $E_C = 35\text{MV/m}$. Further increasing of electric field would lead to a subsequent poling along the reverse direction (i.e., field overshoot), and would again induce an increased polarization ordering (e.g., see Fig. 4-6(c) for a depoling field of $E = 40\text{MV/m}$), and thus result in a decrease of the electrocaloric-induced cooling, as shown by the decreased cooling temperature $\Delta T = -2.0\text{K}$ at $E = 40\text{MV/m}$.

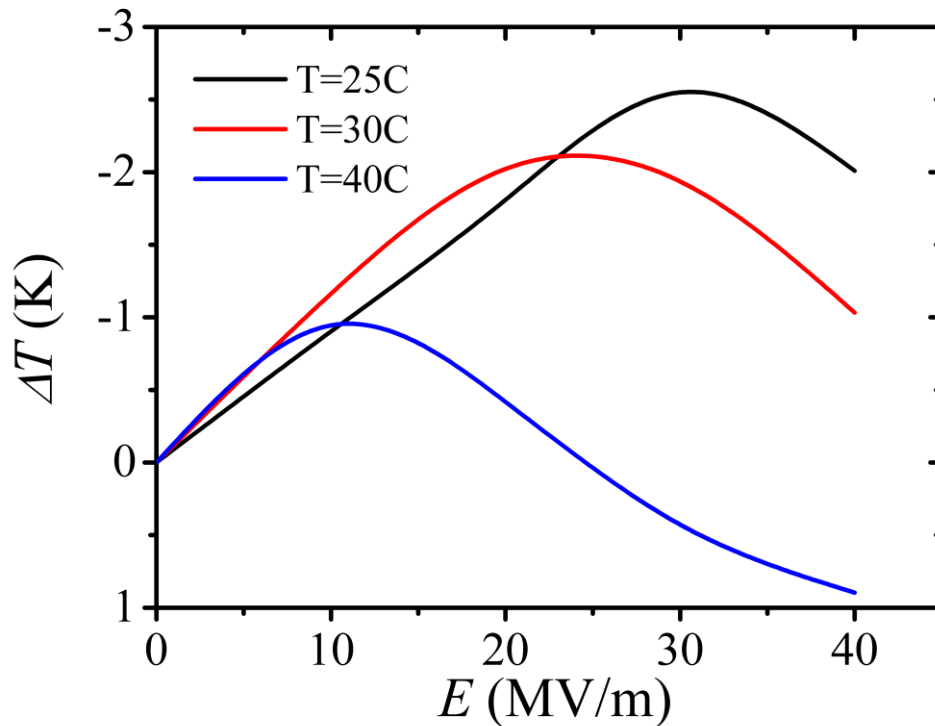


Figure 4-7. Simulated electrocaloric-induced cooling temperature ΔT in the P(VDF-TrFE)/P(VDF-TrFE-CFE) 50/50vol% composite as a function of the applied depoling field, at different operating temperatures $T=25^{\circ}\text{C}$, 30°C , and 40°C . With an increasing temperature, the overshooting threshold field decreases, resulting in a decreased maximum cooling temperature.

With increasing operating temperatures, the overshooting threshold field sharply decreases. As seen in Fig. 4-7, the overshooting threshold decreases to $E=24\text{MV/m}$ at 30°C and $E=11\text{MV/m}$ at 40°C . This is caused by the smaller coercive field of the P(VDF-TrFE)/P(VDF-TrFE-CFE) composite at increased temperatures (see Fig. 4-4) during the transition of the composite from a normal ferroelectric material to a ferroelectric relaxor. Such temperature dependence of overshooting threshold results in a decreased cooling peak ΔT at increased operating temperatures.

On the other hand, at a fixed low electric field (smaller than the overshooting threshold), the electrocaloric-induced cooling temperature ΔT is also slightly enhanced upon increasing operating temperatures, due to the more prominent depoling effect of the ferroelectric domains upon applying a small field before overshooting. For example, at $E=5\text{MV/m}$, the cooling temperature increases from $\Delta T=-0.4\text{K}$ to $\Delta T=-0.6\text{K}$, upon increasing the operating temperature from 25°C to 40°C .

4.4 Conclusion

In this chapter, through applying a phase-field model, we studied the anomalous negative electrocaloric effect, i.e., cooling phenomenon upon applying an electric-field pulse without subsequent heating, in the ferroelectric P(VDF-TrFE)/P(VDF-TrFE-CFE) 50/50vol% composite. A thermodynamic scheme is employed to calculate the electrocaloric effect during the evolution of domain structures.

Upon applying a reverse electric field to a poled composite, the sample is depoled with randomly oriented domains, which structure is stable upon removing the electric field. A decreased dipole order in such process results in an entropy decrease, i.e., a cooling effect. Both the P(VDF-TrFE) normal ferroelectric phase and the P(VDF-TrFE-CFE) relaxor phase are crucial in such phenomena, as they act to stabilize the poled (ordered) state and depoled (disordered) state, respectively. An adiabatic cooling of $\Delta T = -2.6^\circ\text{C}$ on applying an electric field pulse of $E = 30\text{MV/m}$ is found, which quantitatively agrees with the previous experimental measurement [118]. The dependence of the electrocaloric cooling temperature and overshooting field on the operating temperature is predicted.

Chapter 5

Phase-field study on inhomogeneous ferroelectric domain dynamics under ultrafast stimuli

5.1 Introduction

5.1.1 Background

Recent experimental observations and discoveries show fascinating dynamic phenomena and responses of inhomogeneous ferroelectric crystals under ultrafast ($>$ GHz) external stimuli [121-129]. For example, applying a 100fs laser pulse on the surface of a BaTiO₃ single crystal with a typical ferroelectric *a/c* domain structure generated local lattice oscillations with different dynamical behaviors of *a*- and *c*-domains [130], as shown in Fig. 5-1. It was shown that a single 100fs, 800 nm laser pulse applied to a PbTiO₃/SrTiO₃ superlattice led to the formation of an emergent “supercrystal” state, i.e. a 3-dimensional periodic array of regular domains of nanoscale sizes [131] that are unexpected under normal thermodynamic conditions.

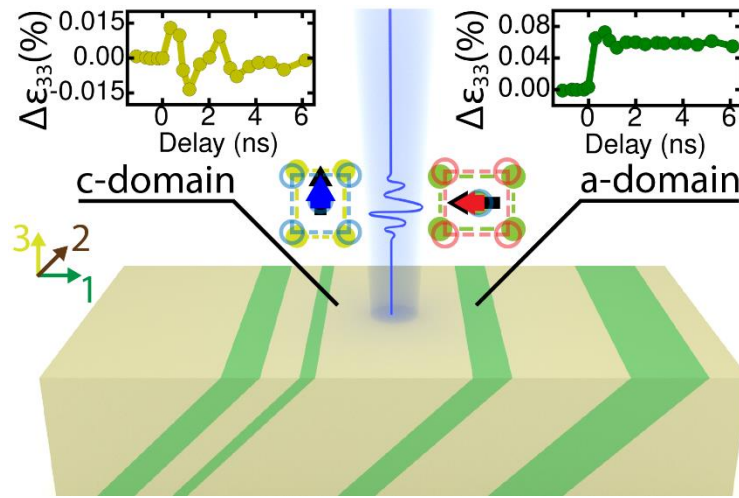


Figure 5-1. Experimentally measured oscillations of local surface strain ε_{33} in *c*-type domains (top-left plot) with an out-of-plane polarization direction (indicated by the blue arrow) and in *a*-type domains (top-right plot) with an in-plane polarization direction (indicated by the red arrow), upon applying an ultrashort laser pulse to the surface of a BaTiO₃ crystal. The figure is adapted from Ref. [130].

According to recent experimental reports, ultrafast electric and mechanical stimuli might produce extraordinary thermal, electric, mechanical and other multifunctional responses. For example, it was predicted that an ultrafast electric field pulse could generate a negative electrocaloric effect as high as 35K in PbTiO₃ within picoseconds [132]. The application of a femtosecond laser pulse on the surface of a ferroelectric PbTiO₃ [121] or BiFeO₃ [129] thin film yielded a transient strain arising from photostriction, a combination of photovoltaic and converse piezoelectric effects [133], which is two orders of magnitude larger than those generated through the static converse piezoelectric coupling.

As discussed above, applying an ultrafast stimulus to a polarization/strain pattern allows one to explore possible new transient phenomena or new metastable domain patterns that may emerge during the relaxation from its excited state back to the original or a new equilibrium state. Furthermore, many practical applications of transducers utilize the piezoelectric responses under stimuli with fast frequencies. A fundamental understanding of ultrafast dynamics in ferroelectrics

domains could further lead to potential applications of ferroelectric materials to THz electronics and all-optical manipulation of electric polarization and polarization domain walls.

Despite increasing experimental interests in ultrafast phenomena of ferroelectric crystals, there is currently still a lack of computational methods for modeling, understanding and predicting the ultrafast-external-fields-stimulated dynamics of complex mesoscale polarization/strain domain and domain wall patterns involving long-range elastic and electrostatic interactions. Although analytical theories [134-145] have been proposed to understand the dynamics of individual domains or planar walls as well as the dynamic dielectric responses of single domain ferroelectrics under high-frequency electric fields, it is challenging to utilize these theories to analyze more complex polarization domain patterns, e.g., those recently discovered in ferroelectric nanostructures (thin-films, islands, superlattices, etc.), such as polarization vortices [146-148], flux-closure domains [149-151], and skyrmions [152, 153]. It is also challenging to analytically treat the electrostatic and mechanical problems within ferroelectric nanostructures of complicated geometries.

5.1.2 Research Objectives

In the present work, we develop a dynamical phase-field model for understanding and predicting the ultrafast-external-fields-stimulated dynamic responses of domains and domain walls in ferroelectric nanostructures. Phase-field method allows us to take into account the long-range electrostatic and elastic interactions between the volume elements of a domain structure [154] and the polarization gradient energy as well as arbitrarily complex mesoscale polarization patterns and wall configurations. The present work further expands the conventional phase-field description of ferroelectric domains to the application in the ultrafast regime, i.e., GHz-THz scales.

The dynamics of a ferroelectric domain under ultrafast time range involves various dynamical mechanisms, including polarization dynamics, elastodynamics, and electrodynamics. As seen in the dielectric spectroscopy, polarization dynamics of a solid typically shows a relaxational behavior at around GHz frequency and 2 resonance behaviors at around THz and higher frequencies indicating polarization oscillation under an external field. Phase-field model based on Time-dependent Ginzburg-Landau equation (Equation 1-1) describe only the kinetic relaxation of a non-equilibrium state towards equilibrium, during which the free energy of an inhomogeneous state always decreases. Therefore, they cannot be directly applied to describing the oscillations of polarization and strain under high-frequency electric fields or mechanical forces.

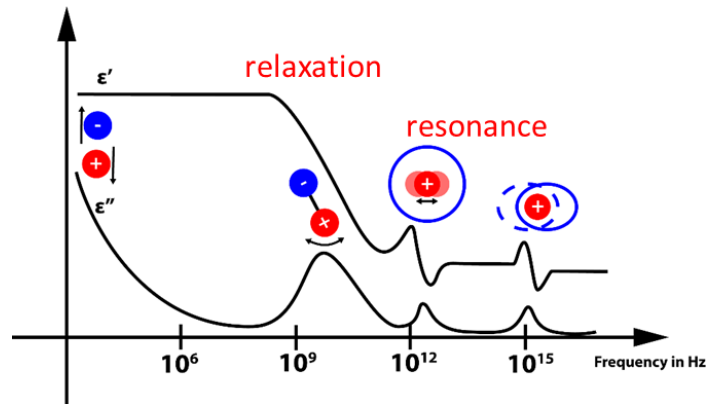


Figure 5-2. Schematic illustration of dielectric responses of a solid subject at different frequencies. The figure is adapted from [155].

Furthermore, the electrostatic and elastic equilibrium conditions considered in conventional phase-field descriptions are based on an important assumption that electrostatic and elastic equilibrium conditions are achieved in a much shorter time than the time for relaxation of domain structures or response to external stimuli. However, the assumption is no longer valid if the applied mechanical force pulse or electric field pulse is shorter than the minimum time span

for reaching the mechanical equilibrium or electrostatic equilibrium. As a matter of fact, the time for the establishment of a mechanical equilibrium condition or electrostatic equilibrium condition would scale proportionally with system size. For example, the typical time for the establishment of mechanical equilibrium $\sim 10^{-12}$ s in a system with ~ 100 nm size. In a sample with similar size, electrostatic equilibrium is established within much shorter time, typically $\sim 10^{-15}$ s. The present work aims at investigating domain dynamics under external stimuli with an ultrafast frequency of GHz~THz. Hence elastodynamics is treated instead of the conventional elastic equilibrium conditions, while the electrostatic condition still holds.

5.2 Phase-field model on ultrafast dynamics of ferroelectric materials

Following the discussion above, the present work focuses on a phase-field model of ferroelectric materials integrated with ultrafast polarization dynamics and elastodynamics.

5.2.1 Polarization dynamics

In an ultrafast scheme, we replace the time-dependent Ginzburg-Landau equation (Equation 1-1) with the nonlinear Klein-Gordon equation

$$\mu_{ij} \frac{\partial^2 P_i}{\partial t^2} + \gamma_{ij} \frac{\partial P_i}{\partial t} + \frac{\delta F}{\delta P_j} = 0 \quad (5-1)$$

to describe the temporal evolution of polarization. The kinetic parameters μ and γ are effective mass coefficient and damping coefficient of polarization evolution, respectively, which are related to the oscillation behavior of ferroelectric domains. μ and γ possess the symmetry of the high-temperature paraelectric phase and are therefore isotropic in ferroelectric perovskites, i.e.,

$$\mu_{11} = \mu_{22} = \mu_{33}, \mu_{12} = \mu_{13} = \mu_{23} = 0 \text{ and } \gamma_{11} = \gamma_{22} = \gamma_{33}, \gamma_{12} = \gamma_{13} = \gamma_{23} = 0.$$

Such description on the evolution of the local polarization \mathbf{P} is first proposed by Glinchuk *et al.* [140] in an analytical study on the high-frequency dielectric responses of a ferroelectric multilayer, where they extracted the nonlinear dielectric dispersion law as a function of wave vector and film thickness using the proposed equation. Similarly [141], they calculated the temperature dependence of the soft-mode frequency and the frequency dependence of the dielectric susceptibility of a ferroelectric thin film, which are qualitatively consistent with experimental measurements.

Here we briefly show the relation between kinetic parameters μ and γ and the intrinsic polarization oscillation and induced elastic vibration of ferroelectric domains. Consider the intrinsic vibration of \mathbf{P} in a ferroelectric single domain around its equilibrium value \mathbf{P}_{eq} . Assuming small vibration amplitude and constant external field, a linear restoring force can be expressed as

$$-\frac{\delta F}{\delta \mathbf{P}} = -\kappa^{-1}(\mathbf{P} - \mathbf{P}_{\text{eq}}) \quad (5-2)$$

where κ is the static dielectric permittivity of the ferroelectric domain. Thus, the general solution of Equation 5-2 is a damped oscillation written as

$$\mathbf{P} = \mathbf{P}_{t0} \exp\left(-\frac{\beta}{2}t\right) \exp\left[I\left(\sqrt{\omega_0^2 - \frac{\beta^2}{4}}\right)t\right] + \mathbf{P}_{\text{eq}} \quad (5-3)$$

where $\beta = \gamma_{11}/\mu_{11}$, $\omega_0^2 = \mu_{11}^{-1}\kappa^{-1}$, \mathbf{P}_{t0} is a constant determined by the initial condition, and I is the imaginary unit. As seen, the intrinsic frequency and rate of decay of the damped oscillation are determined by the kinetic parameters μ and γ . Under constant applied strain or stress, the evolution of strain in the ferroelectric domain is dominated by the evolution of ferroelectric order (i.e., polarization), and can also be estimated as a damped oscillation with the same frequency and rate of decay with the polarization evolution,

$$\varepsilon \approx \varepsilon_{t0} \exp\left(-\frac{\beta}{2}t\right) \exp\left[I\left(\sqrt{\omega_0^2 - \frac{\beta^2}{4}}\right)t\right] + \varepsilon_{eq}. \quad (5-4)$$

This indicates that the kinetic parameters μ and γ can be obtained using experimental measurements of the evolution of either polarization or strain, under a constant external field, by fitting the evolution of polarization/strain into a damped oscillation model and solving with the fitted intrinsic frequency and rate of decay.

The kinetic parameters of the BaTiO₃ single crystal are obtained through fitting the observed vibration of lattices reported by our experimental collaborators in Ref. [130]. Material constants of BaTiO₃ used in the dynamical phase-field model are listed in Table 5-1 [156].

Table 5-1. Material constants of BaTiO₃ in the dynamical phase-field model

Material Constant	Value
a_1	$(T - 388) \times 4.124 \times 10^5 \text{ J} \cdot \text{m} \cdot \text{C}^{-2}$
a_{11}	$-2.097 \times 10^8 \text{ J} \cdot \text{m}^5 \cdot \text{C}^{-4}$
a_{12}	$7.974 \times 10^8 \text{ J} \cdot \text{m}^5 \cdot \text{C}^{-4}$
a_{111}	$1.294 \times 10^9 \text{ J} \cdot \text{m}^9 \cdot \text{C}^{-6}$
a_{112}	$-1.950 \times 10^9 \text{ J} \cdot \text{m}^9 \cdot \text{C}^{-6}$
a_{123}	$-2.501 \times 10^9 \text{ J} \cdot \text{m}^9 \cdot \text{C}^{-6}$
a_{1111}	$3.863 \times 10^{10} \text{ J} \cdot \text{m}^{13} \cdot \text{C}^{-8}$
a_{1112}	$2.529 \times 10^{10} \text{ J} \cdot \text{m}^{13} \cdot \text{C}^{-8}$
a_{1122}	$1.637 \times 10^{10} \text{ J} \cdot \text{m}^{13} \cdot \text{C}^{-8}$
a_{1123}	$1.367 \times 10^{10} \text{ J} \cdot \text{m}^{13} \cdot \text{C}^{-8}$
g_{11}	$4.0 \times 10^{-10} \text{ J} \cdot \text{m}^{-1} \cdot \text{C}^{-2}$
g_{12}	0
g_{44}	$2.0 \times 10^{-10} \text{ J} \cdot \text{m}^{-1} \cdot \text{C}^{-2}$
g'_{44}	$2.0 \times 10^{-10} \text{ J} \cdot \text{m}^{-1} \cdot \text{C}^{-2}$
c_{11}	$1.98 \times 10^{11} \text{ Pa}$
c_{12}	$9.6 \times 10^{10} \text{ Pa}$
c_{44}	$1.22 \times 10^{11} \text{ Pa}$
Q_{11}	$0.11 \text{ m}^4 \cdot \text{C}^{-2}$
Q_{12}	$-0.045 \text{ m}^4 \cdot \text{C}^{-2}$

Q_{44}	$0.059\text{m}^4 \cdot \text{C}^{-2}$
α_L	$9 \times 10^{-6} \text{K}^{-1}$
μ_{11}	$5 \times 10^{-11} \text{J} \cdot \text{m} \cdot \text{A}^{-2}$
γ_{11}	$5 \times 10^{-2} \text{J} \cdot \text{m} \cdot \text{A}^{-2} \cdot \text{s}^{-1}$
ρ	$6.02 \times 10^3 \text{kg} \cdot \text{m}^{-1}$
α	0
β	$6.0 \times 10^{-12} \text{s}$

We developed a numerical solution based on Semi-implicit Fourier-spectral method [157-159] for Equation 5-1. First, we separate the contribution of gradient energy

$$F_{\text{gradient}} = \frac{1}{2} g_{ijkl} \frac{\partial P_i}{\partial x_j} \frac{\partial P_k}{\partial x_l} \quad (5-5)$$

to the driving force from all other energy contributions, i.e.,

$$f_{P_i} = -\frac{\delta F}{\delta P_i} = f_{P_i}^A + f_{P_i}^B \quad (5-6A)$$

$$f_{P_i}^A = -\frac{\delta}{\delta P_i} (F_{\text{Landau}} + F_{\text{electric}} + F_{\text{elastic}}) \quad (5-6B)$$

$$f_{P_i}^B = -\frac{\delta}{\delta P_i} F_{\text{gradient}} = g_{ijkl} \frac{\partial^2 P_k}{\partial x_j \partial x_l} \quad (5-6C)$$

and rewrite Equation 5-1 as

$$\mu_{ij} \frac{\partial^2 P_j}{\partial t^2} + \gamma_{ij} \frac{\partial P_j}{\partial t} - f_{P_i}^A - g_{ijkl} \frac{\partial^2 P_k}{\partial x_j \partial x_l} = 0 \quad (5-7)$$

For time discretization, a central, implicit, 2nd-order accurate difference scheme [160-162] is adopted, i.e.,

$$\mu_{ij} \frac{P_j^{[n+1]} - 2P_j^{[n]} + P_j^{[n-1]}}{\tau^2} + \gamma_{ij} \frac{P_j^{[n+1]} - P_j^{[n-1]}}{\tau} - f_{P_i}^A - \frac{g_{ijkl}}{4} \frac{\partial^2 P_k^{[n+1]} + 2P_k^{[n]} + P_k^{[n-1]}}{\partial x_j \partial x_l} = 0 \quad (5-8)$$

Superscripts $[n]$ denote quantities at the n -th evolution time step. τ is the time period per evolution step. The spatial differentials are then treated using a Fourier-spectral method. Through taking a

Fourier transform in the 3-dimensional space, i.e., $\mathbf{P}(x_1, x_2, x_3) \rightarrow \tilde{\mathbf{P}}(q_1, q_2, q_3)$ and $\mathbf{f}_P(x_1, x_2, x_3) \rightarrow \tilde{\mathbf{f}}_P(q_1, q_2, q_3)$, the solution of Equation 5-1 is given by

$$\tilde{P}_i^{[n+1]} = 4\tau^2 A_{ik} \tilde{f}_{Pk}^{A[n]} + B_{ik} \tilde{P}_k^{[n]} + B_{ik}^- \tilde{P}_k^{[n-1]} \quad (5-9A)$$

$$\begin{cases} (\mathbf{A}^{-1})_{ik} = 4\mu_{ik} + 2\tau\gamma_{ik} + g_{ijkl}q_jq_l\tau^2 \\ B_{ik} = A_{im} (8\mu_{mk} - 2\tau^2 g_{mjkl}q_jq_l) \\ B_{ik}^- = A_{im} (2\tau\gamma_{mk} - 4\mu_{mk} - \tau^2 g_{mjkl}q_jq_l) \end{cases} \quad (5-9B)$$

5.2.2 Elastodynamics

In the dynamical phase-field model for ferroelectric materials, the displacement field \mathbf{u} (or alternatively, strain field $\boldsymbol{\varepsilon}$) is employed as a second set of order parameter in addition to the polarization field \mathbf{P} , whose temporal evolution is described by the elastodynamics equation

$$\rho \left(\frac{\partial^2 u_i}{\partial t^2} + \alpha_{ij} \frac{\partial u_j}{\partial t} \right) = f_{vi} + \frac{\partial}{\partial x_j} \left(\sigma_{ij} + \beta \frac{\partial \sigma_{ij}}{\partial t} \right). \quad (5-10)$$

Here ρ is the density of the material, α and β are mass damping coefficient and stiffness damping coefficient, respectively, \mathbf{f}_v is the external body force density, i.e., external body force per unit volume, and $\boldsymbol{\sigma}$ is the local stress field, expressed as

$$\sigma_{ij} = c_{ijkl} (\varepsilon_{kl} - \varepsilon_{kl}^0) \quad (5-11)$$

where ε^0 is the eigenstrain field which is coupled to the polarization order parameter through the electrostrictive effect, i.e.,

$$\varepsilon_{ij}^0 = Q_{ijkl} P_k P_l + \varepsilon_{ij}^{\text{lattice}} \quad (5-12)$$

through which the elastodynamics equation and the polarization dynamics is coupled; \mathbf{Q} is the electrostrictive tensor, and $\boldsymbol{\varepsilon}^{\text{lattice}}$ is the spontaneous strain of the lattice due to factors other than

polarization order, e.g., lattice mismatch between different phases, or thermal expansion. Formulations similar to Equation 5-10 have previously been adopted in simulations of crack propagation dynamics [163-166]. It replaces the elastic equilibrium equation in regular phase-field models treating phase transformations with longer time ranges.

There have been previous attempts to numerically solve Equation 5-10 for the elastodynamics based on the finite element method [167-169]. Here we develop a numerical solution based on Fourier-spectral method [157-159] to Equation 5-10 with a 3-dimensional periodic boundary condition. The local strain is considered summation of a homogeneous strain and a heterogeneous strain, i.e., $\varepsilon_{ij}(\mathbf{x}) = \overline{\varepsilon_{ij}} + \delta\varepsilon_{ij}(\mathbf{x})$, where the heterogeneous strain $\delta\varepsilon_{ij}(\mathbf{x})$ is defined as

$$\delta\varepsilon_{ij} = \frac{1}{2} \left(\frac{\partial u_i}{\partial x_j} + \frac{\partial u_j}{\partial x_i} \right) \quad (5-13)$$

and satisfies

$$\int_V \delta\varepsilon_{ij} dx^3 = 0. \quad (5-14)$$

The homogeneous strain $\overline{\varepsilon_{ij}}$ represents the macroscopic deformation of the whole system.

Equation 5-10 is thus rewritten as

$$\rho \left(\frac{\partial^2 u_i}{\partial t^2} + \alpha_{ij} \frac{\partial u_j}{\partial t} \right) = f_{vi} + \left(1 + \beta \frac{\partial}{\partial t} \right) c_{ijkl} \frac{\partial^2 u_k}{\partial x_j \partial x_l} - \left(1 + \beta \frac{\partial}{\partial t} \right) c_{ijkl} \frac{\partial \varepsilon_{kl}^0}{\partial x_j} \quad (5-15)$$

The time discretization is conducted similarly to the treatment of the polarization dynamics equation (Equation 5-1), where a central, implicit, 2nd-order accurate difference scheme is adopted, i.e.,

$$\begin{cases} \mathbf{y} \rightarrow \frac{\mathbf{y}^{[n+1]} + 2\mathbf{y}^{[n]} + \mathbf{y}^{[n-1]}}{4} \\ \frac{\partial \mathbf{y}}{\partial t} \rightarrow \frac{\mathbf{y}^{[n+1]} - \mathbf{y}^{[n-1]}}{2\tau} \\ \frac{\partial^2 \mathbf{y}}{\partial t^2} \rightarrow \frac{\mathbf{y}^{[n+1]} - 2\mathbf{y}^{[n]} + \mathbf{y}^{[n-1]}}{\tau^2} \end{cases} \quad (5-16)$$

Here \mathbf{y} represents several variables including displacement, strain, stress, and eigenstrain, etc.

Equation 5-10 is reduced to a 2nd-order linear differential equation of $\mathbf{u}^{[n+1]}(\mathbf{x})$, expressed as

$$\begin{aligned} & \frac{\rho(u_i^{[n+1]} - 2u_i^{[n]} + u_i^{[n-1]})}{\tau^2} + \frac{\rho\alpha_{ij}(u_j^{[n+1]} - u_j^{[n-1]})}{2\tau} = f_{Vi}^{[n]} + c_{ijkl} \frac{\partial^2}{\partial x_j \partial x_l} \frac{u_k^{[n+1]} + 2u_k^{[n]} + u_k^{[n-1]}}{4} \\ & + \beta c_{ijkl} \frac{\partial^2}{\partial x_j \partial x_l} \frac{u_k^{[n+1]} - u_k^{[n-1]}}{2\tau} - c_{ijkl} \frac{\partial}{\partial x_j} \frac{\varepsilon_{kl}^{0[n+1]} + 2\varepsilon_{kl}^{0[n]} + \varepsilon_{kl}^{0[n-1]}}{4} - \beta c_{ijkl} \frac{\partial}{\partial x_j} \frac{\varepsilon_{kl}^{0[n+1]} - \varepsilon_{kl}^{0[n-1]}}{2\tau} \end{aligned} \quad (5-17)$$

A Fourier spectral method is adopted herein for solving the equation. Through performing a 3-dimensional Fourier transform in space for all spatial variables, e.g., $\mathbf{u}(x_1, x_2, x_3) \rightarrow \tilde{\mathbf{u}}(q_1, q_2, q_3)$, the solution is given by

$$\tilde{u}_i^{[n+1]} = 4\tau^2 A_{ik} \tilde{f}_{Vk}^{[n]} + B_{ik} \tilde{u}_k^{[n]} + B_{ik}^- \tilde{u}_k^{[n-1]} + C_{ikl} \tilde{\varepsilon}_{kl}^{0[n]} + C_{ikl}^+ \tilde{\varepsilon}_{kl}^{0[n+1]} + C_{ikl}^- \tilde{\varepsilon}_{kl}^{0[n-1]} \quad (5-18A)$$

$$\begin{cases} (A^{-1})_{ik} = 2\rho(2\delta_{ik} + \alpha_{ik}\tau) + c_{ijkl}q_jq_l\tau(\tau + 2\beta) \\ B_{ik} = 8\rho A_{ik} - 2A_{im}c_{mjkl}q_jq_l\tau^2 \\ B_{ik}^- = A_{im}(2\rho(\alpha_{mk}\tau - 2\delta_{mk}) + c_{mjkl}q_jq_l\tau(2\beta - \tau)) \\ C_{ikl} = -2IA_{im}c_{mjkl}q_j\tau^2 \\ C_{ikl}^+ = -IA_{im}c_{mjkl}q_j\tau(\tau + 2\beta) \\ C_{ikl}^- = -IA_{im}c_{mjkl}q_j\tau(\tau - 2\beta) \end{cases} \quad (5-18B)$$

δ is the Kronecker delta herein.

This solver works on a 3-dimensional periodic boundary problem with given applied strain or applied stress type of boundary condition and an initial local displacement field and local velocity field as the initial condition. For testing the numerical accuracy of the solver, a

preliminary test is conducted. We chose an isotropic system with $c_{11} = 210\text{GPa}$, $c_{12} = 90\text{GPa}$, $\rho = 5.0 \times 10^3 \text{kg/m}^3$, $\alpha_{11} = 2.0 \times 10^{10} \text{s}^{-1}$, and $\beta = 2.0 \times 10^{-12} \text{s}$. For simplicity, we employed a 2-dimensional system and assumed an initial displacement field \mathbf{u} with a Gaussian distribution centered in the middle of the simulation cell, zero initial velocity, zero body force, zero homogeneous strain, and zero eigenstrain. We plot the displacement along the central line as a function of time. As shown, the displacement field spreads out in space as a traveling wave whose magnitude decays over time. To check the correctness of the numerical solutions, we compare the solutions using the spectral solver with those using the finite-element method. As shown in Fig. 5-3, our preliminary results show that the solution from our spectral solver accurately matches the finite-element-method-based solution using the software COMSOL Multiphysics®. Moreover, our preliminary tests show that our spectral solver for the elastodynamics is at least an order of magnitude faster than the finite-element-method-based solver implemented in COMSOL Multiphysics®.

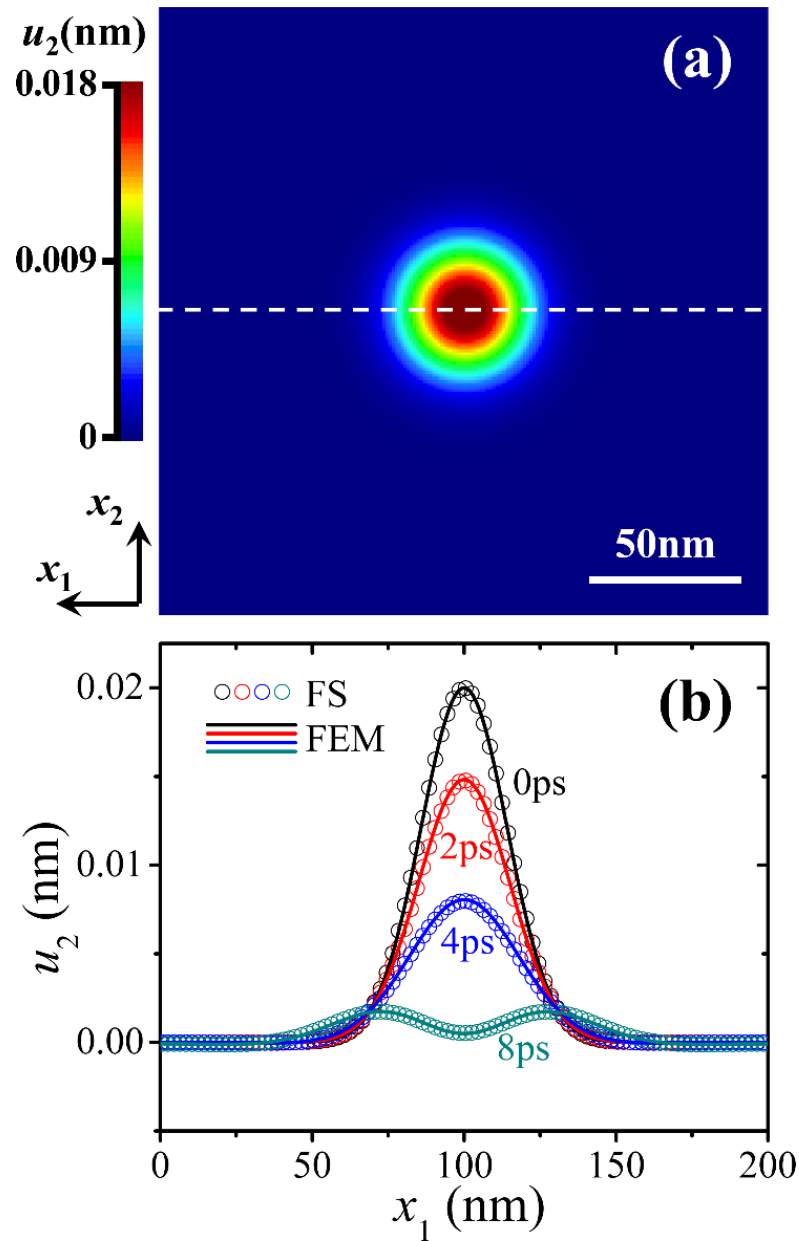


Figure 5-3. Numerical solution to the elastodynamics equation with our own solver based on the Fourier-spectral method (Equation 5-18), as compared with the elastodynamic solver in COMSOL Multiphysics® based on finite-element method (a) Initial displacement field u_2 , set as a Gaussian function of distance to the center of the simulation region. Initial velocity is set as 0. (b) Displacement field along the central line (indicated by the dashed line in (a)) at different times.

The solution of elastodynamics equation, coupled with the solution of polarization dynamics equation, and electrostatic equilibrium Poisson equation, are employed in the

dynamical phase-field model for ferroelectric systems, which will yield the spatial polarization dynamics and elastodynamics of a ferroelectric and ferroelastic domain structure as well as the local electric potential and stress distributions.

5.3 Domain wall dynamics under ultrafast electric field stimuli

We applied the dynamical phase-field model to a study on the high-frequency response behavior of ferroelectric domain walls and vortex core in BaTiO₃. As shown in Figs. 5-4(a) and 5-4(b), in a regular *a/c* stripe multi-domain with 90° domain walls, an AC electric field parallel to the domain wall plane is applied, which induces periodic domain wall motions, together with expansion and compression of the domain stripes. Shown in Figs. 5-4(c) and 5-4(d) is the motion of the vortex core in an island with a vortex domain structure, responsive to an AC electric field. Differences in characteristics of high-frequency and low-frequency dynamics of ferroelectric domain walls are described, where the high-frequency domain wall motion shows a typical flat stage during the cycle of a decreasing field, which is absent in the low-frequency mode.

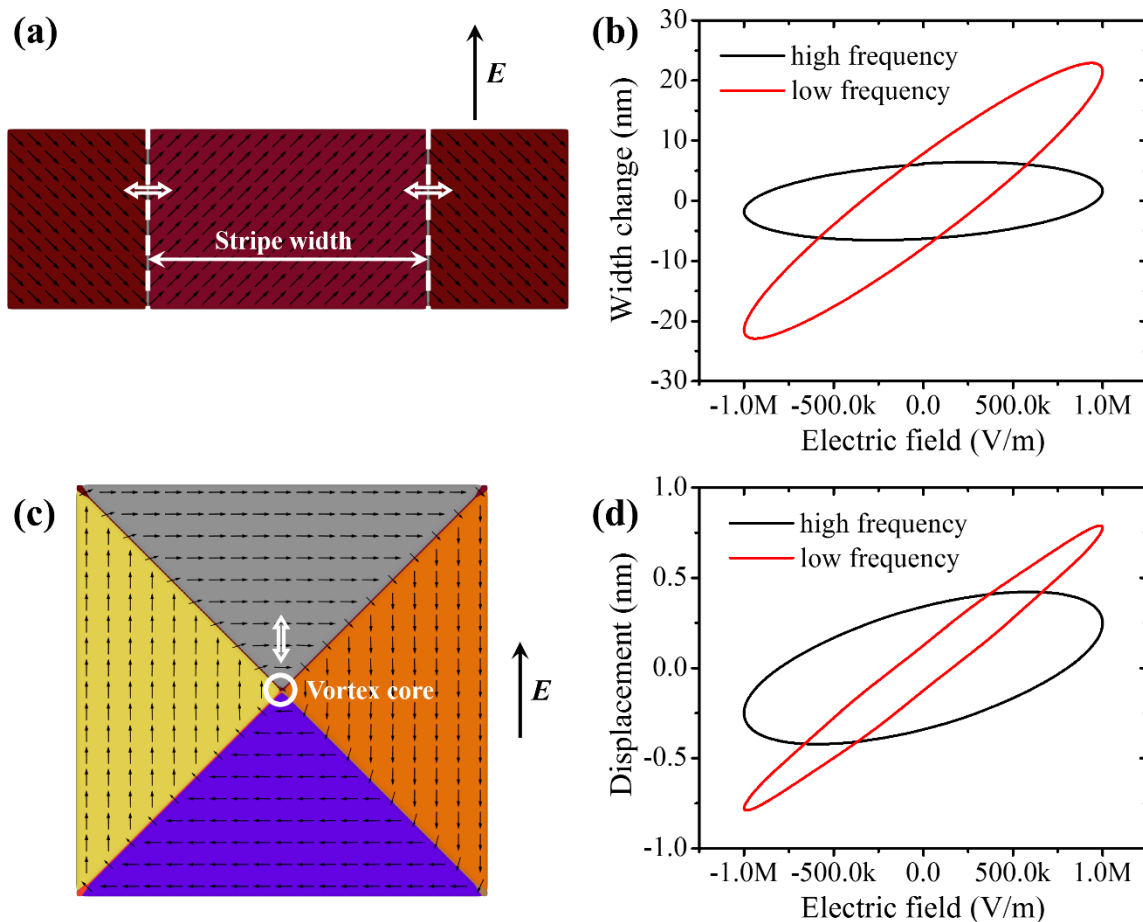


Figure 5-4. Dynamics of ferroelectric domain wall and vortex upon applying an AC electric field. (a) A multi-domain structure in BaTiO_3 with 90° domain walls and (b) the change in the width of the domain stripe responsive to an AC electric field. (c) A vortex domain structure in a BaTiO_3 island and (d) the displacement of the vortex core responsive to an AC electric field.

5.4 Ultrafast domain dynamics under thermal stimuli

We further study the polarization dynamics on applying ultrashort external thermal stimuli. As shown in Fig. 5-5(a), in a BaTiO_3 single domain with $P_1 = 0.260\text{C/m}^2$ at room temperature ($T = 298\text{K}$), an ultrafast heat pulse is applied in a circular region (in orange) at time $t = 0$, which instantaneously raises the local temperature by $\Delta T = 100\text{K}$. The temporal evolution and

spatial distribution of temperature field in the system is simulated by solving the thermal conduction equation, and the polarization dynamics is investigated.

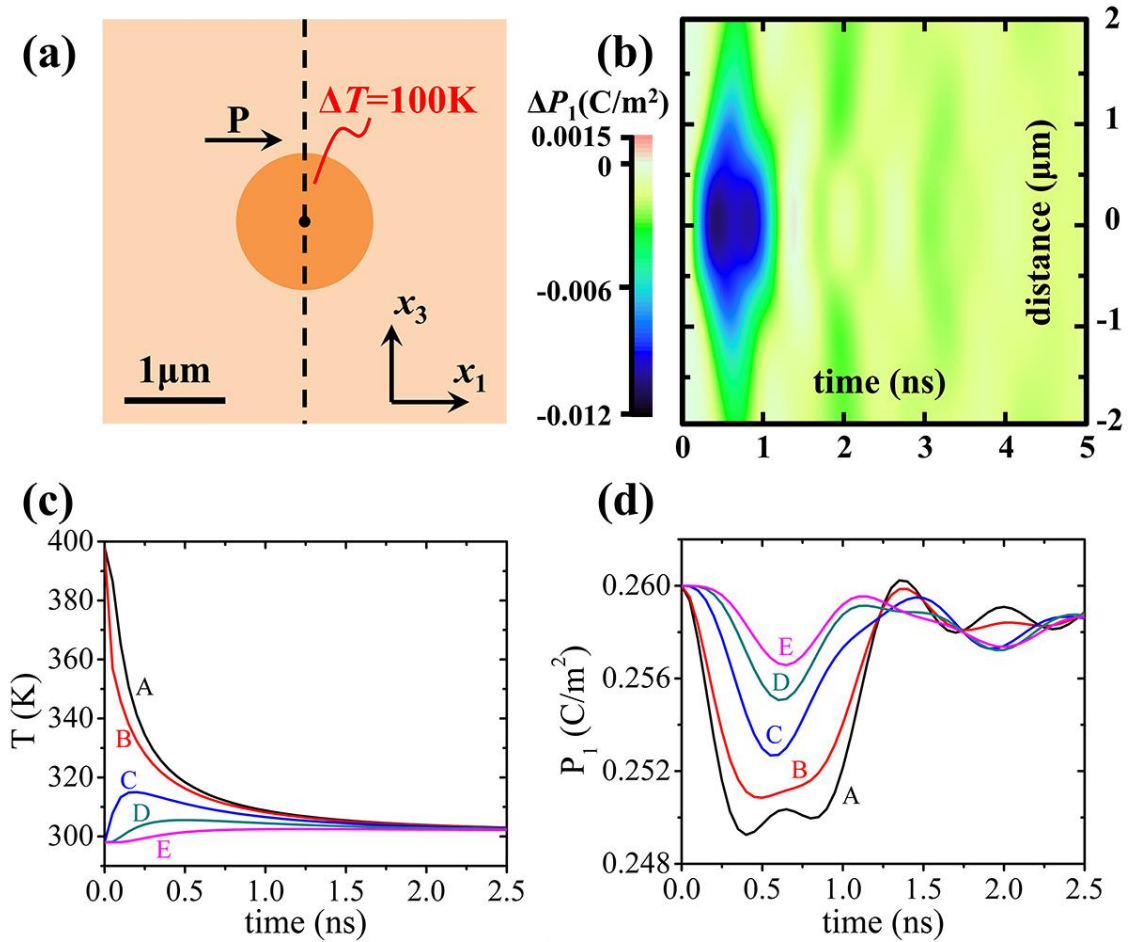


Figure 5-5. Ferroelectric domain dynamics upon applying a local heat pulse. (a) At $t=0$, a heat pulse is applied in a circular region (in orange) in a BaTiO₃ single domain, which raises the local temperature instantaneously by $\Delta T = 100\text{K}$. (b) The spatial-temporal map of the polarization change ΔP_1 along the vertical line across the center of the heated region (as indicated by the dashed line in (a)), after applying the laser pulse. The vertical axis indicates the distance Δx_3 from the center of the heated region. (c) Temperature T and (d) polarization P_1 in the first 2.5ns after heating, at different points below the heated region (along the dashed line in (a)), at distances $\Delta x_3 = 0$ (Point A), $\Delta x_3 = 0.5\ \mu\text{m}$ (Point B), $\Delta x_3 = 1.0\ \mu\text{m}$ (Point C), $\Delta x_3 = 1.5\ \mu\text{m}$ (Point D), $\Delta x_3 = 2.0\ \mu\text{m}$ (Point E), respectively.

As seen in Fig. 5-5(c), points A~E on the vertical dashed line in 6-5(a) with increasing distance $d = 0, 0.5, 1.0, 1.5,$ and $2.0\ \mu\text{m}$ from the center of the heated region undergoes a

temperature evolution with decreasing peak temperatures as well as increasing time delays on reaching the temperature peak, before reaching an equilibrium temperature $T = 302\text{K}$ within $\sim 2\text{ns}$. Response of the polarization field arises from the temperature change due to the pyroelectric effect, in which the polarization P_1 undergoes an initial decrease and subsequent oscillation (before approaching the new equilibrium value $P_1 = 0.258\text{C/m}^2$) at all points throughout the affected region (Fig. 5-5(d)) yet with various oscillation amplitudes, periods and phases. With increasing distances, the first trough of the oscillation appears at an increasing time delay $t = 0.40, 0.49, 0.57, 0.61,$ and 0.64ns , respectively, with a decreasing oscillation amplitude, as caused by the increasing delay and decreasing temperature of the temperature peak. Points C~E undergo similar oscillation periods of $\sim 1.4\text{ns}$, while points A and B from within the initially heated regions undergo additional oscillation periods compared with points C~E, as shown by two additional wave crests at $t = 0.81\text{ns}$ and $t = 2.30\text{ns}$ in the polarization oscillation. This is caused by the fast temperature decrease at these positions, which shifts the equilibrium position of polarization at a higher rate than the intrinsic oscillation frequency of polarization, showing more features of a forced oscillation.

The spatial-temporal map of polarization change ΔP_1 along the vertical dashed line in (a), is shown in Fig. 5-5(b). The evolution of polarization field at various positions outside the initially heated regions shows a similar oscillation period $\sim 1.4\text{ns}$ as determined by the intrinsic polarization dynamics, yet a delayed phase determined by the local temperature field, showing a dependence of polarization evolution on both the thermal conduction process and the intrinsic polarization dynamics.

5.5 Domain dynamics under ultrafast mechanical stimuli

The domain dynamics on applying ultrafast mechanical stimuli to a ferroelectric domain is further investigated. Figure 5-6 shows the simulated ferroelectric domain evolution on applying an ultrashort pulse of a local force. As seen in the first panel in the first row, in a ferroelectric a^+ single domain, we apply a force perpendicular to the polarization vector with body force density $f_{V3} = 2.5\text{nN/nm}^3$ and duration of 10ps within the dashed circular region at the center of the simulation system with radius $R = 320\text{nm}$. The evolution of strain and ferroelectric domains is simulated using the dynamical phase-field model.

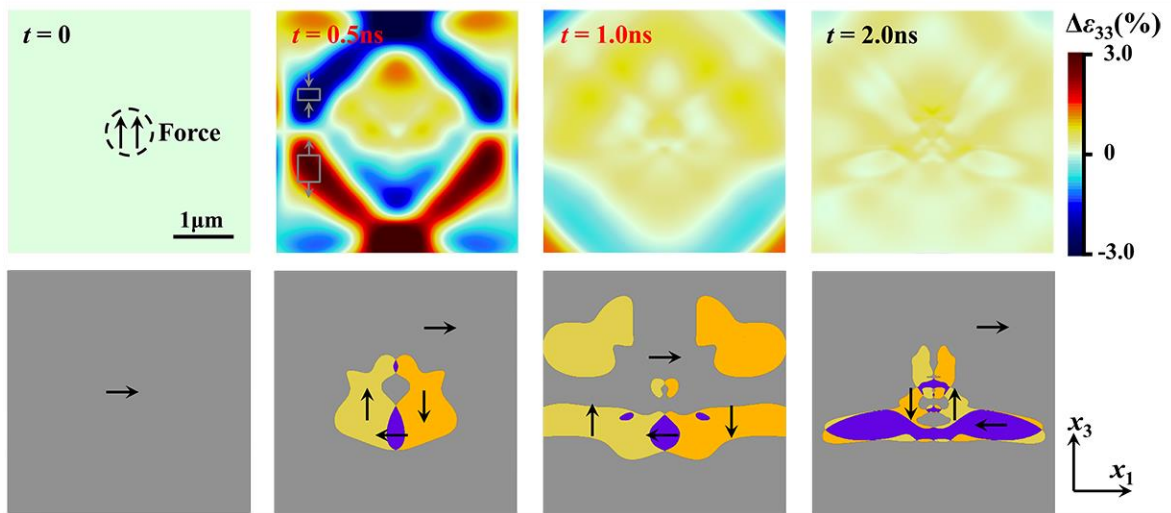


Figure 5-6. Evolution of (upper row) the strain field and (lower row) ferroelectric domain structure after applying a local body force with $f_{V3} = 2.5\text{nN/nm}^3$ and a duration of 10ps within a circular region (with radius $R = 320\text{nm}$) in a ferroelectric a_1 single domain. Local 180° domain switching is observed.

A mechanical wave is induced by the applied force with ripple patterns of alternating positive and negative strain changes $\Delta\epsilon_{33}$ (using the strain field ϵ at $t=0$ as a reference), as shown by the red/orange and blue/cyan regions in the first row in Fig. 5-6, which propagates away from

the center of the simulation system. A polarization response is induced by the mechanical wave due to the polarization-mechanical coupling through electrostrictive effect, which is shown by the evolution of ferroelectric domain structure in the second row in Fig. 5-6. In addition to regions with $\pm 90^\circ$ domain switching forming c^+ and c^- domains, regions below the center of the system undergoes a distinct 180° domain switching, forming an a^- domain which grows through time and remains stable. Consequently, a new multidomain structure dominated by mixed a^+ and a^- domains is generated upon reaching the new equilibrium.

Mesoscale mechanism of such ferroelectric domain structure evolution is revealed by analyzing the coupling of local polarization response to local strain field. As seen in the first panel of Fig. 5-7, at time delay $t = 0.5\text{ns}$ after applying the force, the spatial distribution of polarization response can be categorized into 4 different regimes, as indicated by point A, B, C1/C2, and D, respectively.

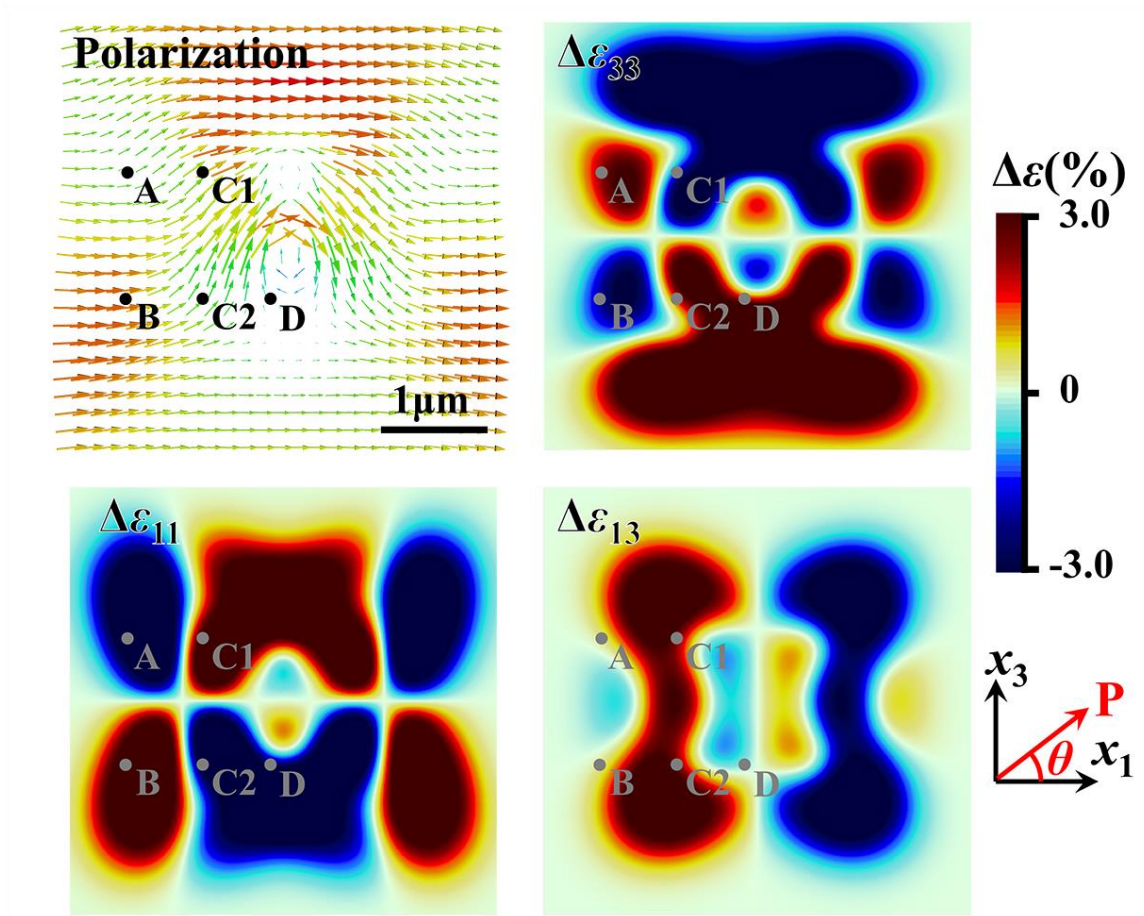


Figure 5-7. The profile of polarization \mathbf{P} at time delay $t=0.5\text{ns}$, and the profile of strain change $\Delta\epsilon_{33}$, $\Delta\epsilon_{11}$, and $\Delta\epsilon_{13}$ at time delay $t=0.25\text{ns}$, after applying the external force.

The polarization response at point A is dominated by a decrease in polarization amplitude without notable polarization rotation. This is caused by the change in normal strain components $\Delta\epsilon_{33} > 0$ and $\Delta\epsilon_{11} < 0$ which reduces P_1 through piezoelectric effect, as shown in Fig. 5-7. Note that the strain changes at time delay $t = 0.25\text{ns}$ is demonstrated herein, which advances the observed polarization response ($t = 0.5\text{ns}$) by $\Delta t = 0.25\text{ns}$, considering a finite time delay of polarization response under the influence of the local strain. Meantime, Point B undergoes an increase in polarization P_1 , which is induced by a strain change $\Delta\epsilon_{33} < 0$ and $\Delta\epsilon_{11} > 0$ through piezoelectric effect.

Regions around points C1 and C2 show counterclockwise polarization rotation by an angle $\theta < 90^\circ$, which is caused by the positive local shear strain $\varepsilon_{13}(=\Delta\varepsilon_{13}) > 0$ favoring rotation of the polarization vector towards the $+x_3$ direction forming a region with $P_1 > 0$ and $P_3 > 0$. However, distinct changes in local normal strains $\Delta\varepsilon_{33}$ and $\Delta\varepsilon_{11}$ also affect the polarization response, in which regions around point C1 undergo $\Delta\varepsilon_{33} < 0$ and $\Delta\varepsilon_{11} > 0$, favoring a decrease of P_1 and an increase of P_3 , thus resulting in a relatively small rotation angle $\theta < 45^\circ$ where \mathbf{P} would easily relax back to the original a^+ domain once the strain change $\Delta\varepsilon_{13}$ diminishes in time; regions around point C2 undergo a strain change $\Delta\varepsilon_{33} > 0$ and $\Delta\varepsilon_{11} < 0$, favoring an increase of P_1 and decrease of P_3 , with a much larger rotation angle $\theta > 45^\circ$, approaching the c^+ ferroelectric domain.

Point D undergoes a distinct process in which polarization rotates by an even larger angle $\theta > 90^\circ$. This is caused by the dynamical process of the local polarization evolution coupled to the evolution of the strain. Figure 5-8 shows the temporal evolution of polarization rotation angle and local shear strain $\varepsilon_{13}(=\Delta\varepsilon_{13})$ in the 180° domain switching region, at point D in Fig. 5-7. In the first 0.25ns after applying the local force, the local shear strain ε_{13} at point D undergoes a sign change from $\Delta\varepsilon_{13} > 0$ to $\Delta\varepsilon_{13} < 0$, as induced by the periodically alternating positive and negative strains generated and propagating from the center of the simulated system (Fig. 5-8(b)). As a result, the local polarization first undergoes a counterclockwise rotation towards the $+x_3$ direction during $t = 0 \sim 0.3$ ns (similarly to the adjacent C2 point at $t = 0.5$ ns discussed above), and then further rotates counterclockwise with $\theta > 135^\circ$ at $t = 0.5$ ns under the effect of a negative $\Delta\varepsilon_{13}$ which energetically favors a monoclinic ferroelectric domain with $P_1 < 0$ and $P_3 > 0$ (Fig. 5-8(a)). Subsequent evolution in local strain $\Delta\varepsilon_{13}$ continues to undergo several additional sign changes, yet with a fast decaying amplitude and is no longer strong enough to further switch the ferroelectric domain. Consequently, the local polarization gradually approaches the new equilibrium of an a^- domain at an energy minimum equivalent to the initial a^+ domain.

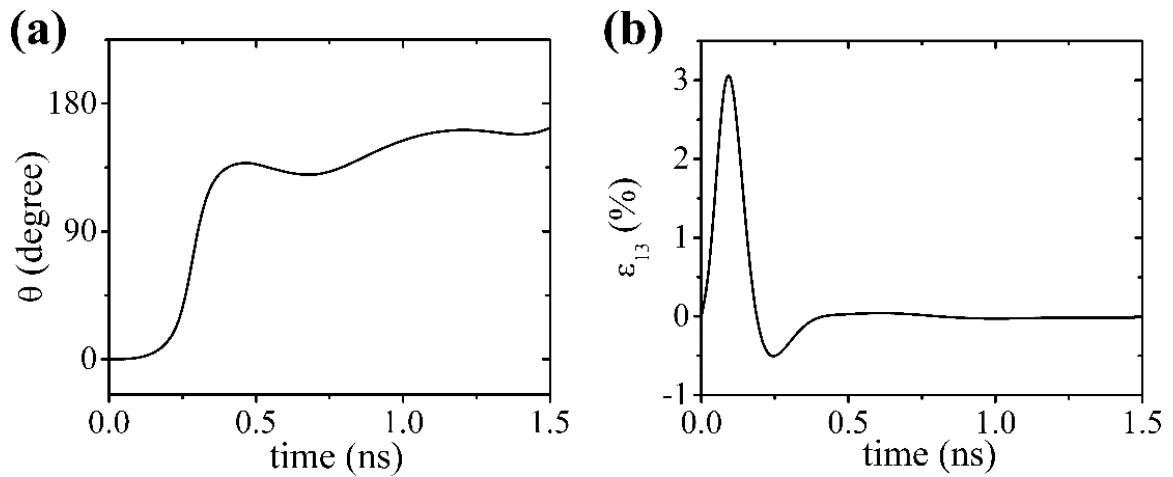


Figure 5-8. Time sequence of (a) rotation angle of polarization and (b) strain change $\Delta\epsilon_{13}$ at Point D (as indicated in Fig. 5-7), after applying the external force.

As a result, local deterministic non-volatile 180° ferroelectric domain switching is achieved through applying an ultrashort local mechanical pulse. Note that such 180° domain switching is difficult to achieve through applying a static force, strain, or stress, since the electro-mechanical coupling always possesses an inverse symmetry of polarization upon applying an external strain or stress, due to the symmetry of the ferroelectric perovskites, and thus favors formation of domains along either direction opposite each-other. To break such symmetry and achieve possible deterministic 180° domain switching, one can provide an external strain or stress with spatial variation and utilize the flexoelectric effect, or alternatively, one can provide an external strain or stress with temporal variation and utilize the polarization dynamics. Here we demonstrated through dynamical phase-field modeling a simple approach of applying an ultrashort pulse of a local force. More transient phenomena involving ultrafast dynamics of ferroelectric domains can be explored in future using the developed dynamical phase-field model.

5.6 Domain dynamics of a BaTiO₃ crystal under an ultrashort laser pulse

We further apply the dynamical phase-field model to study experimentally measured laser-pulse activated domain dynamics in a BaTiO₃ crystal. Experiments are conducted by our collaborators H. Akamatsu, V. Gopalan et al. [130].

As shown in Fig. 5-1, applying a 100fs laser pulse on the surface of a BaTiO₃ crystal with a typical *a/c* ferroelectric domain structure generates strain oscillations with ~GHz frequency. In addition to different dynamic behaviors observed in *a*- and *c*-domains, distinct dynamic behaviors of domains near the surface (surface regions) and domains at $\geq 700\text{nm}$ deep below the surface (subsurface domains) are also observed [130].

The response in the subsurface domains of the BaTiO₃ crystal under the applied laser pulse is modeled by considering the thermal effect of the laser which would heat up the affected region containing a few ferroelectric domains, as illustrated in the first panel in Fig. 5-9. A tentative effective temperature increase of $\Delta T = 6\text{K}$ is used.

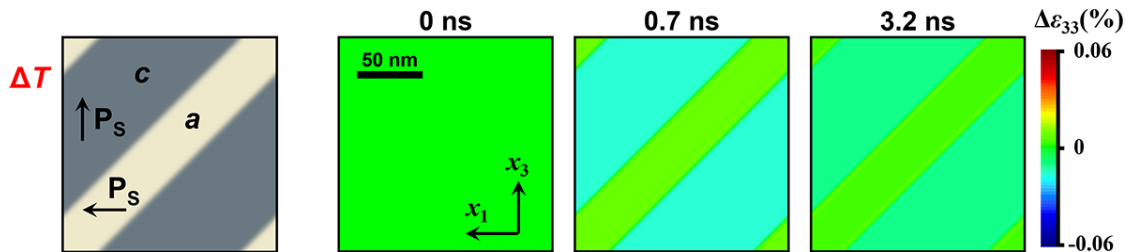


Figure 5-9. (First panel) schematics of domain structure in the subsurface region. (Other panels) simulated strain map $\Delta\epsilon_{33}$ at time delays $t = 0\text{ ns}$, $t = 0.7\text{ ns}$, and $t = 3.2\text{ ns}$, respectively, in the subsurface region.

As shown in Fig. 5-10(a), under the increased temperature $\Delta T = 6\text{K}$, the polarization inside each domain undergoes a damped oscillation with ~GHz frequency and decreases to a new equilibrium state through pyroelectric effect. Evolution of the strain field is closely coupled to the

polarization response through electrostrictive effect, and it undergoes a damped oscillation with almost the same frequency. Effect of the temperature increase directly through thermal expansion shows a smaller influence in the change of the strain field. The simulated temporal evolution of the strain $\Delta\epsilon_{33}$ in c -domains shows an oscillation and decrease due to the decrease of local P_3 , which quantitatively agrees with the experimental measurement in subsurface c -domains, as shown in Fig. 5-10(b). Similarly, the simulated temporal evolution of the strain $\Delta\epsilon_{33}$ in a domains undergoes a slight increase due to the decrease of local P_1 . Simulated strain map of the subsurface domains at different time delays are shown in Fig. 5-9. Therefore, the observed lattice dynamics of subsurface domains under the applied laser pulse can be explained by a pure thermal effect.

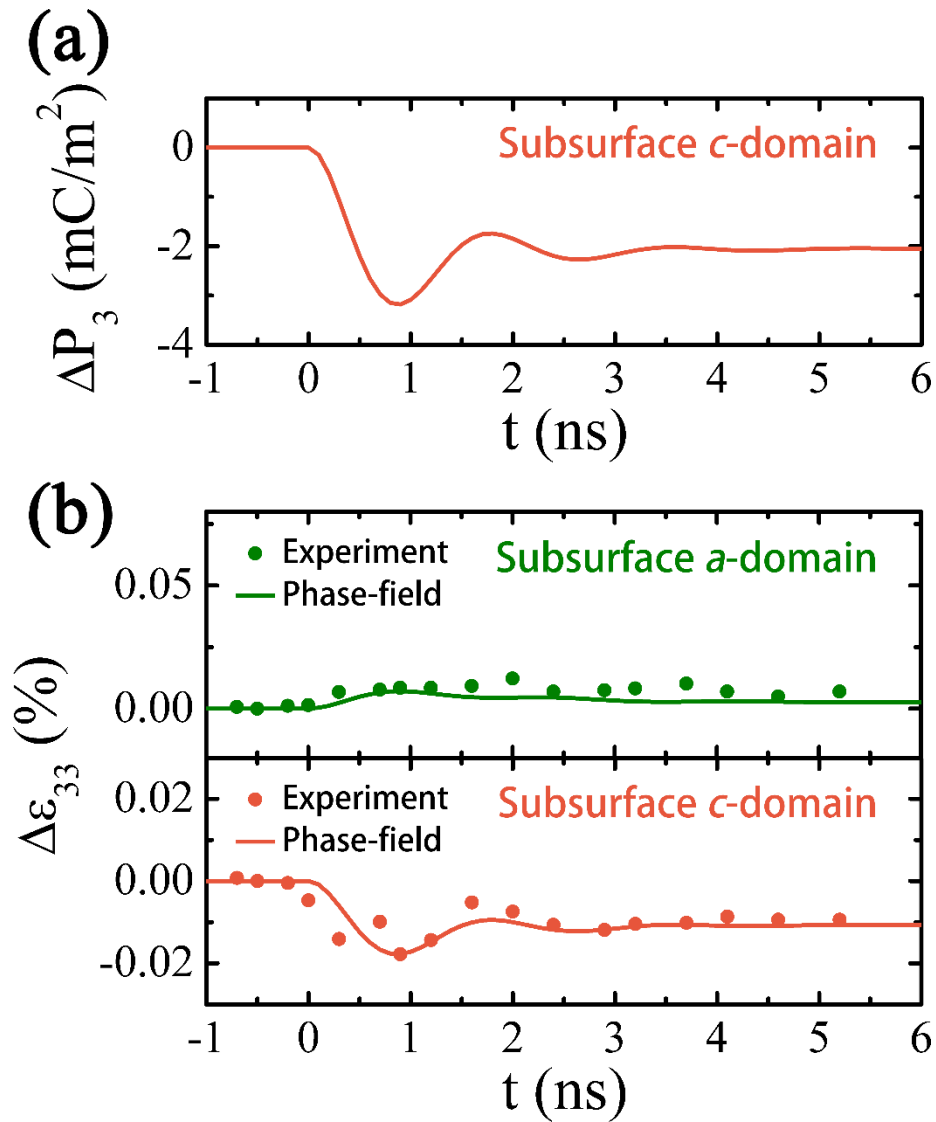


Figure 5-10. (a) Evolution of polarization change ΔP_3 in subsurface *c*-domain from the dynamical phase-field simulation. (b) Evolution of strain change $\Delta \epsilon_{33}$ in subsurface *a*- and *c*-domains from experimental measurement (dots) [130] and dynamical phase-field simulation (solid lines).

The dynamical evolution of the surface regions undergoes an initial increase of the out-of-plane strains $\Delta \epsilon_{33}$ in both *a*- and *c*-domains (Fig. 5-1) [130], showing different behavior from subsurface domains, which indicates the existence of a possible surface layer [170-174]. Specifically, the initial increase of $\Delta \epsilon_{33}$ in surface *c*-domains is contrary to a pure thermal effect. To understand the phenomena, we consider possible generation of an effective out-of-plane

electric field pulse E in the surface layer on applying the laser pulse onto the BaTiO₃ crystal, in addition to the thermal effect, as shown in the first panel of Fig. 5-11. An effective electric field pulse of $E=20\text{MV}$ with duration of 0.1ns is considered.

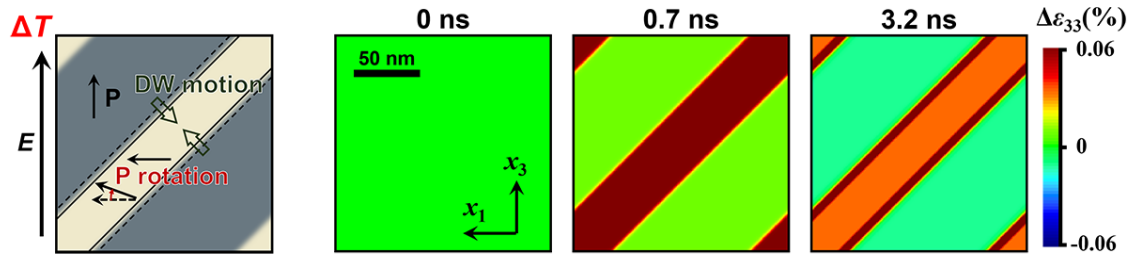


Figure 5-11. (First panel) schematics of domain structure in the surface region. The *a/c* domain wall (DW) moves towards *a* domain, while polarization inside *a* domain rotates towards the out-of-plane direction. (Other panels) simulated strain map $\Delta\epsilon_{33}$ at time delays $t=0\text{ns}$, $t=0.7\text{ns}$, and $t=3.2\text{ns}$, respectively, in the surface region.

Fig. 5-12(b) shows simulated temporal evolution of out-of-plane strain $\Delta\epsilon_{33}$ in surface *a*- and *c*-domains. The initial increase of $\Delta\epsilon_{33}$ in both *a*- and *c*-domains induced by the effective electric field pulse is observed showing agreement with the experimental measurement. Surface *c*-domains also undergo a decrease of the out-of-plane strain upon reaching the new equilibrium, i.e., $\Delta\epsilon_{33} < 0$ at $t=6\text{ns}$, due to the decreased equilibrium P_3 through the thermal effect of the laser similar to the case of subsurface *c*-domains.

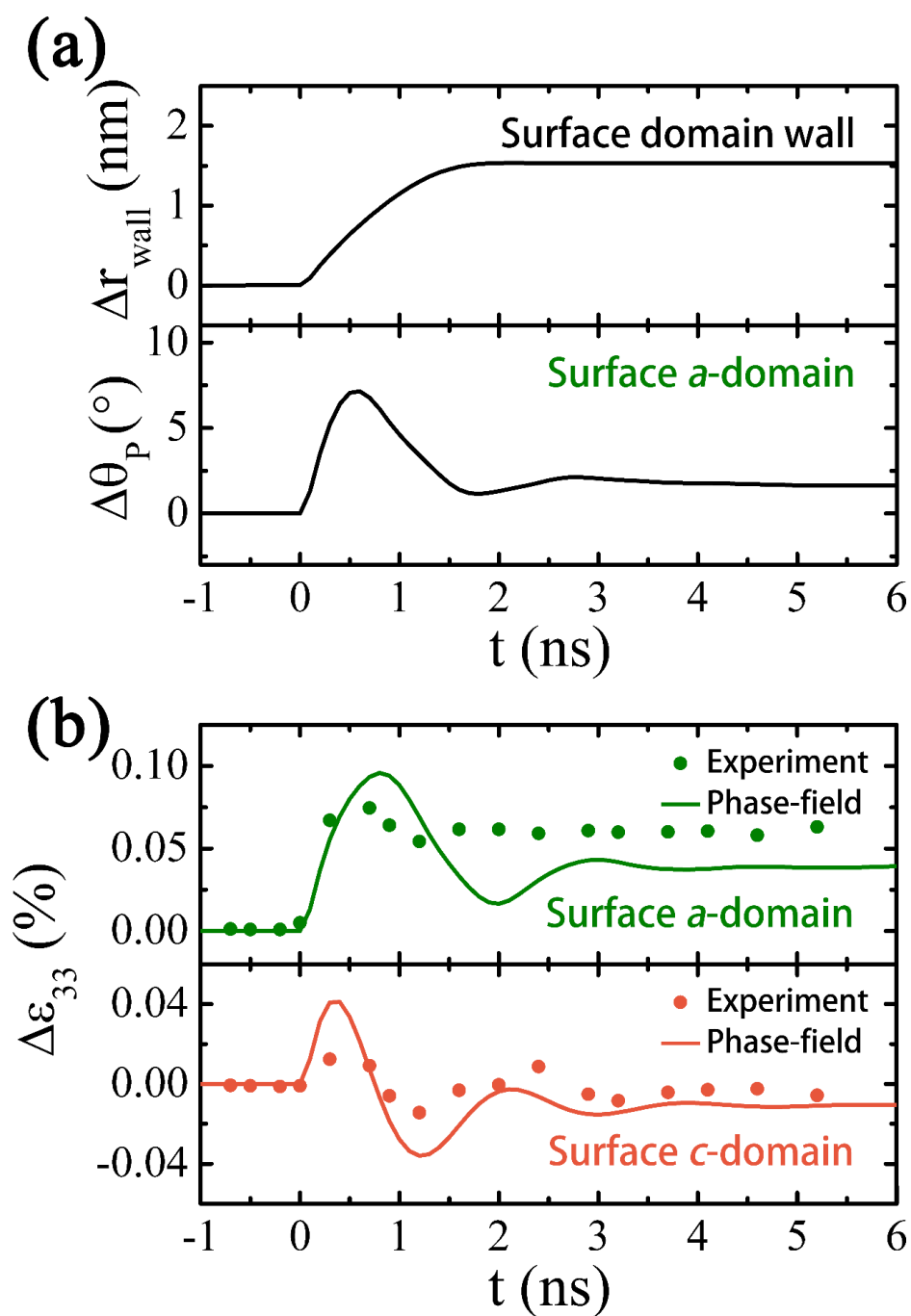


Figure 5-12. (a) Temporal evolution of displacement Δr_{wall} of the surface a/c domain walls and rotation angle $\Delta\theta_P$ of the polarization vector in surface a domains from the dynamical phase-field simulation. (b) Evolution of strain change $\Delta\varepsilon_{33}$ in the surface a - and c -domains from experimental measurement (dots) [130] and dynamical phase-field simulation (solid lines).

The effective electric field pulse also activated the motion of surface domain walls, where the a/c domain wall moves towards the a domain by $\sim 1.6\text{nm}$ or ~ 4 unit cells, resulting in a shrink of the surface a domain, leading to a subsonic domain wall speed of 2.5m/s within the first 1ns , as shown in Fig. 5-12(a). Such domain wall motion is also represented by a strong strain change at regions $\Delta\epsilon_{33}$ around the domain wall upon approaching new equilibrium, as shown in the simulated strain profile at the surface region at time delay 3.2ns in Fig. 5-11. The domain wall motion is further coupled with a rotation of polarization inside surface a domain towards the out-of-plane direction (see schematics in the first panel of Fig. 5-11) by an equilibrium value of $\Delta\theta_P = 2^\circ$, as shown in Fig. 5-12(a). Such polarization rotation in surface a domains coupled to domain wall motion results in the observed increase of out-of-plane strains towards the new equilibrium, i.e., $\Delta\epsilon_{33} = 0.04\%$ at $t = 6\text{ns}$. Therefore, we conclude that a combination of thermal effect and generation of an effective electric field pulse is responsible for the distinct behavior of the observed lattice dynamics in surface domains excited by an applied laser pulse.

5.7 Conclusion

In this chapter, we developed a dynamical phase-field model for understanding and predicting dynamical responses of inhomogeneous ferroelectric domains under ultrafast electrical, thermal, mechanical, and optical stimuli. Governing equations for ultrafast polarization dynamics and elastodynamics were introduced, where advanced numerical algorithms were employed.

As an example, we investigated the domain dynamics of BaTiO_3 under various types of ultrafast stimuli. The frequency-dependent response of domain wall motion and vortex core evolution to an external AC electric field is demonstrated. Domain dynamics under an external

local heat pulse show a combined characteristic of thermal conduction and intrinsic polarization dynamics under local temperature changes.

Ferroelectric domain dynamics under an ultrafast external mechanical force is determined by the dynamical process of the local polarization evolution couple to the temporal evolution of the strain. Our simulation demonstrated ultrafast-stimulated emerging transient phenomena which is absent on applying static stimuli. A deterministic 180° ferroelectric domain switching is discovered, which shows possibilities for precise mechanical manipulation of ultrafast ferroelectric domain switching.

We further successfully explained the experimentally observed laser-pulse-induced domain dynamics with distinct responses determined by both the orientation and the location of the domains. Mesoscale mechanisms of ferroelectric domain and domain wall responses under laser excitation as well as intrinsic lattice vibrations are revealed, where the critical influence of surface phenomena is demonstrated.

The present dynamical phase-field study focused on the polarization dynamics and elastodynamics at the GHz-THz scales while assuming electrostatic equilibrium. Future study can further incorporate the electrodynamics at petahertz (PHz) frequencies which will allow one to explore a full range of dynamic phenomena. We also plan to introduce into the phase-field model the electron correlation order for correlated systems, and employ electron-lattice, electron-polarization, and electron-antiferromagnetic coupling, and further investigate potential formation of novel electronic phases under ultrafast stimuli, including manipulation of metal-insulator transitions in correlated systems. The theoretical insights on ultrafast domain dynamics will provide useful guidance for exploring and manipulating dynamical functionalities of ferroelectric materials.

Chapter 6

Conclusions and future work

6.1 Summary and conclusions

In this dissertation, we developed phase-field models to investigate the properties of ferroelectric composites and heterostructures. Material properties including polarization, elastic, and thermal responses during the evolution of ferroelectric and ferroelastic domains in chosen systems, arising from the piezoelectric coupling, magnetoelectric coupling, electro-thermal coupling, as well as under ultrafast dynamic stimuli, are examined. The main contributions of the dissertation include:

- I. In Chapter 2, a phase-field model coupled with constitutive equations was developed to investigate the direct magnetoelectric coupling in bulk multiferroic magnetic/ferroelectric composites. It provides a detailed examination of the composites that goes from the mesoscopic modeling of the local polarization/elastic field distributions (domains) to the predictions of effective magnetoelectric response within the context of the continuum media theory under a periodic boundary condition. These functional properties have proven to be strongly dependent on several microstructural factors of the composites including the phase fraction and phase connectivity. Such a simple phase-field based multi-scale approach should also have broad potential applications in predicting various effective properties such as the piezoelectric, piezomagnetic, dielectric, and elastic responses in composite materials, which are directly deduced from the response of the complex microstructure to external fields.

The present model can also be extended to include non-linear contributions to the effective properties, e.g., from domain wall motion, by incorporating magnetic exchange energy and ferroelectric gradient energy in total free energy to describe magnetic and ferroelectric domain walls, respectively.

- II. In Chapter 3, we employed a phase-field model to study the local elastic coupling behaviors of the magnetic and ferroelectric domains in a multiferroic heterostructure of a magnetic film grown on a ferroelectric substrate. Taking a polycrystalline $\text{Co}_{0.4}\text{Fe}_{0.6}$ and a BaTiO_3 crystal as an example, the one to one match of the initial magnetic and ferroelectric domain structures and the repeated electric-field writing and erasure of the magnetic striped domains have been simulated, providing modeling supplement and theoretical insights to experimental observations. Studies on the kinetics of the electric-field-driven magnetic domain evolution reveal an alternating occurrence of local magnetization rotation and the coupled motion of magnetic and ferroelectric domain walls with almost identical velocities.
- III. In Chapter 4, through applying a phase-field model, we studied the anomalous negative electrocaloric effect, i.e., cooling phenomenon upon applying an electric-field pulse without subsequent heating, in the ferroelectric $\text{P}(\text{VDF-TrFE})/\text{P}(\text{VDF-TrFE-CFE})$ 50/50vol% composite. A thermodynamic scheme is employed to calculate the electrocaloric effect during the evolution of domain structures, based on tracking the evolution of the free energy of the system.

Upon applying a reverse electric field to a poled composite, the sample is depoled with randomly oriented domains, which structure is stable upon removing the field. A decreased dipole order in such process results in an entropy decrease, i.e., a cooling effect. Both the $\text{P}(\text{VDF-TrFE})$ normal ferroelectric phase and the $\text{P}(\text{VDF-TrFE-CFE})$ relaxor phase are crucial in such phenomena, as they act to stabilize the poled state and

depoled state, respectively. An adiabatic cooling of $\Delta T = -2.6^\circ\text{C}$ on applying $E = 30\text{MV/m}$ is found, which quantitatively agrees with the previous experimental measurement. The dependence of the electrocaloric cooling and overshooting field on operating temperature is predicted.

- IV. In Chapter 5, we developed a dynamical phase-field model for understanding and predicting dynamical responses of ferroelectric domains under ultrafast electrical, thermal, and mechanical stimuli. Governing equations for ultrafast polarization dynamics and elastodynamics were introduced, where advanced numerical algorithms were employed. As an example, we investigated the ferroelectric domain dynamics of BaTiO_3 crystals under various types of ultrafast stimuli. The frequency-dependent response of domain wall motion and vortex core evolution to an external AC electric field is demonstrated. Domain evolution dynamics under an external local heat pulse show a combined characteristic of thermal conduction and intrinsic polarization dynamics under local temperature changes.

Ferroelectric domain dynamics under an ultrafast external mechanical force is determined by the dynamical process of the local polarization evolution coupled to the temporal evolution of the strain. Our simulation demonstrates ultrafast-stimulated emerging transient phenomena which are absent on applying static stimuli. A deterministic 180° ferroelectric domain switching is discovered, which shows possibilities for precise mechanical manipulation of ultrafast ferroelectric domain switching.

We further successfully explained the experimentally observed laser-pulse-induced domain dynamics with distinct responses determined by both the orientation and the location of the domains. Mesoscale mechanisms of ferroelectric domain and domain wall responses under laser excitation as well as intrinsic lattice vibrations are revealed, where the critical influence of surface phenomena is demonstrated.

6.2 Directions for future work

Based on the phase-field model for ferroelectric composites and heterostructures and the inhomogeneous ferroelectric dynamics under ultrafast external stimuli, the following topics can be further studied.

6.2.1 Microstructure design of piezoelectric composites

Piezoelectricity, in which an electric voltage or polarization develops in response to an applied mechanical stress, finds wide applications in sensors, actuators, and transducers etc., which is important in various industrial and scientific areas. Piezoelectric composite materials offer advantages over single phase piezoelectrics with better performance and greater tunability [15, 16, 175, 176], which involves piezoelectric, dielectric, elastic, and conductivity considerations. Microstructure design has been used to control the performance of the piezoelectric composite. Using the concept of phase connectivity, composites are categorized into 0-3 type (particles), 1-3 type (rods), 2-2 type (multilayers) structures, or more complicated structures like 3-3 type inter-connected network structures (Fig. 6-1); these will strongly influence the effective piezoelectric properties of the composite.

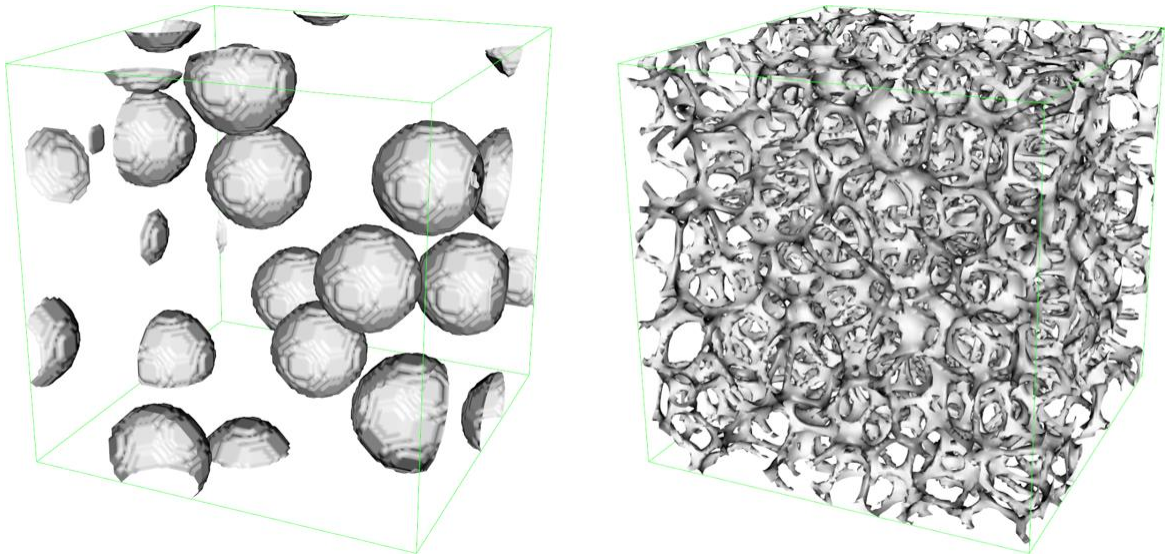


Figure 6-1. Comparison of the structure of piezoelectric composites (left panel) with ferroelectric oxide particles in a dielectric polymer matrix, and (right panel) with a porous ferroelectric ceramic forming interconnected networks in a dielectric polymer matrix. The silver phases indicate the ferroelectric oxide, while the rest of the space in the composite is filled with the polymer phase which is not drawn for clarity. The geometry of the network structure is generated with a grain growth simulation code.

For example, by constructing a porous ferroelectric PZT ceramic forming interconnected networks in a PDMS dielectric polymer matrix (see Fig. 6-1), preliminary phase-field simulation results show that the piezoelectric voltage response is enhanced by 4 times compared with that of composites with 0-3 type particle-matrix structure with the same phase fractions. It is revealed that such structure design would induce a stress distribution more concentrated on the ceramic network, upon applying an external force, resulting in the enhanced effective piezoelectric coupling.

One of the future directions is the theoretical investigation on the effective properties of a piezoelectric composite, including the influence of the phase structure and interfaces, and on enhancing the performance from a microstructural perspective. Both bulk composites and thin film and island nanostructures will be investigated.

6.2.2 Phase-field study on ultrafast dynamics in magnetic/ferroelectric heterostructures

In Chapter 5, a dynamical phase-field model for dynamical responses of ferroelectric domains under ultrafast stimuli is developed based on the coupled ultrafast polarization dynamics and elastodynamics. One future direction in theoretical studies of the dynamical functionalities of electronic materials is to couple the elastodynamics with the micromagnetic formulation for modeling the dynamics of magnetization under an ultrafast local mechanical pulse in ferromagnets, a topic that has recently gained rapidly increasing research interests [177-179]. The Landau-Lifshitz-Gilbert equation (Equation 3-5) describing the magnetization dynamics and the elastodynamics equation (Equation 5-10) are simultaneously solved.

It's also important to further extend the present dynamical phase-field model based on the present work for studying the ultrafast magnetoelectric response in a magnetic/ferroelectric heterostructure (Chapters 2 and 3), with a fully coupled elastodynamics, polarization dynamics, and magnetization dynamics. For example, the elastically coupled magnetic/ferroelectric domain in Chapter 3 (see Figs. 3-5 and 3-6) can be revisited, to investigate how the film thickness, the mechanical compatibility of the magnetic and ferroelectric materials, and the frequency of the applied electric-field pulses will influence the coupling between the ferroelectric and magnetic domains. This fully coupled ferroelectric-micromagnetic-elastodynamic phase-field model would provide a basis for computational optimization of the performances of piezostain-enabled magnetic and spintronic applications.

6.2.3 Phase-field study on ultrafast dynamics in electronic phase transitions

Electronic phase transitions in strongly correlated oxides like VO_2 have attracted great scientific and technological interest in the past decades. The metal-insulator transition, in which

the material switches between metallic and insulating states in an ultrashort time scale under external stimuli, exhibits great potential in novel power-efficient electronic and optical devices [180-182].

A mesoscale theoretical study of ultrafast electronic phase transitions in such systems that help reveal the mesoscale mechanisms would be important in providing theoretical guidance for optimizing the electronic and optical functionalities. In Chapter 5, we developed a dynamical phase-field model focusing on the evolution of polarization and elastic domains through introducing polarization dynamics and elastodynamics. It will be helpful to further introduce into the phase-field model the electron correlation order to describe the electronic phase and domains in strongly correlated systems and enable simulation of ultrafast electronic phase transitions. It's also important to employ electron-lattice, electron-polarization, and electron-antiferromagnetic coupling, and further investigate the potential formation of novel electronic phases under ultrafast stimuli, including manipulation of metal-insulator transitions in correlated systems, etc.

Bibliography

1. Jona, F. and G. Shirane, *Ferroelectric Crystals* 1962, New York: Macmillan.
2. Mitsui, T., I. Tatsuzaki, and E. Nakamura, *An Introduction to the Physics of Ferroelectrics* 1976, New York: Gordon and Breach Science Publishers.
3. Lines, M.E. and A.M. Glass, *Principles and Applications of Ferroelectrics and Related Materials* 1977, Oxford: Clarendon Press.
4. Valasek, J., *Piezo-electric and allied phenomena in Rochelle salt*. Physical Review, 1921. **17**(4): p. 475.
5. Von Hippel, A., et al., *High dielectric constant ceramics*. Industrial & Engineering Chemistry, 1946. **38**(11): p. 1097-1109.
6. Yang, T.N., et al., *On the elastically coupled magnetic and ferroelectric domains: A phase-field model*. Applied Physics Letters, 2014. **104**: p. 0-5.
7. Nye, J.F., *Physical Properties of Crystals: Their Representation by Tensors and Matrices* 1985: Clarendon Press.
8. Wadhawan, V.K., *Introduction to Ferroic Materials* 2000, Amsterdam: Gordon & Breach.
9. Ramesh, R., S. Aggarwal, and O. Auciello, *Science and technology of ferroelectric films and heterostructures for non-volatile ferroelectric memories*. Materials Science & Engineering R-Reports, 2001. **32**(6): p. 191-236.
10. Scott, J.F., *Nanoferroelectrics: statics and dynamics*. Journal of Physics-Condensed Matter, 2006. **18**(17): p. R361-R386.
11. Scott, J.F., *Applications of modern ferroelectrics*. Science, 2007. **315**(5814): p. 954-959.
12. Hu, J.-M., et al., *High-density magnetoresistive random access memory operating at ultralow voltage at room temperature*. Nature Communications, 2011. **2**: p. 553.
13. Hu, J.M., et al., *Design of a voltage-controlled magnetic random access memory based on anisotropic magnetoresistance in a single magnetic layer*. Advanced Materials, 2012. **24**(21): p. 2869-2873.
14. Moya, X., S. Kar-Narayan, and N.D. Mathur, *Caloric materials near ferroic phase transitions*. Nature Materials, 2014. **13**(5): p. 439-450.
15. Newnham, R.E., *Composite Electroceramics*. Annual Review of Materials Science, 1986. **16**(1): p. 47-68.
16. Newnham, R.E. and D.P. Skinner, *Connectivity and piezoelectric-pyroelectric composites*. Materials Research Bulletin, 1978. **13**: p. 525-536.
17. Vaz, C.a.F., et al., *Magnetoelectric coupling effects in multiferroic complex oxide composite structures*. Advanced materials, 2010. **22**: p. 2900-18.
18. Kambale, R.C., D.-Y. Jeong, and J. Ryu, *Current status of magnetoelectric composite thin/thick films*. Advances in Condensed Matter Physics, 2012. **2012**.
19. Hu, J.M., L.Q. Chen, and C.W. Nan, *Multiferroic heterostructures integrating ferroelectric and magnetic materials*. Advanced materials, 2016. **28**(1): p. 15-39.
20. Akdogan, E.K., M. Allahverdi, and A. Safari, *Piezoelectric composites for sensor and actuator applications*. IEEE transactions on ultrasonics, ferroelectrics, and frequency control, 2005. **52**(5): p. 746-775.
21. Newnham, R.E., et al., *Composite piezoelectric transducers*. Materials & Design, 1980. **2**(2): p. 93-106.

22. Boettinger, W.J., et al., *Phase-field simulation of solidification*. Annual Review of Materials Research, 2002. **32**(1): p. 163-194.
23. Chen, L.-Q., *Phase-Field Models for Microstructure Evolution*. Annual Review of Materials Research, 2002. **32**: p. 113-140.
24. Chen, L.-Q., *Phase-Field Method of Phase Transitions/Domain Structures in Ferroelectric Thin Films: A Review*. Journal of the American Ceramic Society, 2008. **91**: p. 1835-1844.
25. Ingo, S., *Phase-field models in materials science*. Modelling and Simulation in Materials Science and Engineering, 2009. **17**(7): p. 073001.
26. Chen, L.-Q. and J. Shen, *Applications of semi-implicit Fourier-spectral method to phase field equations*. Computer Physics Communications, 1998. **108**: p. 147-158.
27. Li, Y.L., et al., *Phase-field model of domain structures in ferroelectric thin films*. Applied Physics Letters, 2001. **78**(24): p. 3878-3880.
28. Tagantsev, A.K., *Landau Expansion for Ferroelectrics: Which Variable to Use?* Ferroelectrics, 2008. **375**: p. 19-27.
29. Li, Y., et al., *Effect of electrical boundary conditions on ferroelectric domain structures in thin films*. Applied Physics Letters, 2002. **81**: p. 427.
30. Li, Y., et al., *Effect of substrate constraint on the stability and evolution of ferroelectric domain structures in thin films*. Acta materialia, 2002. **50**: p. 395-411.
31. Song, P., et al., *A Comparison of Fourier Spectral Iterative Perturbation Method and Finite Element Method in Solving Phase-Field Equilibrium Equations*. Communications in Computational Physics, 2017. **21**(5): p. 1325-1349.
32. Wang, J., et al., *Phase transitions and domain structures of ferroelectric nanoparticles: Phase field model incorporating strong elastic and dielectric inhomogeneity*. Acta Materialia, 2013. **61**(20): p. 7591-7603.
33. Fiebig, M., *Revival of the magnetoelectric effect*. Journal of Physics D: Applied Physics, 2005. **38**: p. R123-R152.
34. Eerenstein, W., N.D. Mathur, and J.F. Scott, *Multiferroic and magnetoelectric materials*. Nature, 2006. **442**: p. 759-65.
35. Nan, C.-W., et al., *Multiferroic magnetoelectric composites: Historical perspective, status, and future directions*. Journal of Applied Physics, 2008. **103**: p. 031101.
36. Hu, J.-M., et al., *Magnetoelectric Responses in Multiferroic Composite Thin Films*. Journal of Advanced Dielectrics, 2011. **01**: p. 1.
37. Ma, J., et al., *Recent progress in multiferroic magnetoelectric composites: from bulk to thin films*. Advanced materials, 2011. **23**: p. 1062-87.
38. Nan, C.-W., *Magnetoelectric effect in composites of piezoelectric and piezomagnetic phases*. Physical Review B, 1994. **50**.
39. Israel, C., N.D. Mathur, and J.F. Scott, *A one-cent room-temperature magnetoelectric sensor*. Nature materials, 2008. **7**(2): p. 93-94.
40. Lage, E., et al., *Exchange biasing of magnetoelectric composites*. Nature materials, 2012. **11**: p. 523.
41. Nan, T., et al., *Self-biased 215 MHz magnetoelectric NEMS resonator for ultra-sensitive DC magnetic field detection*. Scientific reports, 2013. **3**: p. 1985.
42. Dong, S., et al., *Circumferential-mode, quasi-ring-type, magnetoelectric laminate composite—a highly sensitive electric current and /or vortex magnetic field sensor*. Applied Physics Letters, 2005. **86**: p. 182506.
43. Zhang, Y., et al., *Demonstration of magnetoelectric read head of multiferroic heterostructures*. Applied Physics Letters, 2008. **92**: p. 152510.

44. Bai, X., et al., *A magnetoelectric energy harvester with the magnetic coupling to enhance the output performance*. Journal of Applied Physics, 2012. **111**(7): p. 07A938.
45. Harshe, G., J. Dougherty, and R. Newnham, *Theoretical modelling of multilayer magnetoelectric composites*. International Journal of Applied Electromagnetics in Materials, 1993. **4**(2): p. 145-145.
46. Nan, C.-W. and D.R. Clarke, *Effective properties of ferroelectric and/or ferromagnetic composites: A unified approach and its application*. Journal of the American Ceramic, 1997. **40**: p. 1333-1340.
47. Nan, C.-W., et al., *Magnetic-Field-Induced Electric Polarization in Multiferroic Nanostructures*. Physical Review Letters, 2005. **94**: p. 1-4.
48. Benveniste, Y., *Magnetoelectric effect in fibrous composites with piezoelectric and piezomagnetic phases*. Physical Review B, 1995. **51**.
49. Huang, J.H. and W.S. Kuo, *The analysis of piezoelectric/piezomagnetic composite materials containing ellipsoidal inclusions*. Journal of Applied Physics, 1997. **81**(3): p. 1378-1386.
50. Li, J.Y., *Magnetoelastoelectric multi-inclusion and inhomogeneity problems and their applications in composite materials*. International Journal of Engineering Science, 2000. **38**(18): p. 1993-2011.
51. Liu, G., et al., *Coupling interaction in multiferroic BaTiO₃-CoFe₂O₄ nanostructures*. Journal of Physics D: Applied Physics, 2005. **38**: p. 2321-2326.
52. Liu, G., C.-W. Nan, and J. Sun, *Coupling interaction in nanostructured piezoelectric/magnetostrictive multiferroic complex films*. Acta Materialia, 2006. **54**: p. 917-925.
53. Wu, T., et al., *Observation of magnetoelectric effect in epitaxial ferroelectric film/manganite crystal heterostructures*. Physical Review B, 2006. **73**: p. 134416.
54. Pertsev, N.A., H. Kohlstedt, and B. Dkhil, *Strong enhancement of the direct magnetoelectric effect in strained ferroelectric-ferromagnetic thin-film heterostructures*. Physical Review B, 2009. **80**: p. 054102.
55. Kukhar, V.G., N.A. Pertsev, and a.L. Kholkin, *Thermodynamic theory of strain-mediated direct magnetoelectric effect in multiferroic film-substrate hybrids*. Nanotechnology, 2010. **21**: p. 265701.
56. Ni, Y. and A.G. Khachaturyan, *Phase field approach for strain-induced magnetoelectric effect in multiferroic composites*. Journal of Applied Physics, 2007. **102**: p. 113506.
57. Zhang, J., et al., *Phase-field model for epitaxial ferroelectric and magnetic nanocomposite thin films*. Applied Physics Letters, 2007. **90**: p. 052909.
58. Ni, Y., L. He, and A.G. Khachaturyan, *Equivalency principle for magnetoelastoelectric multiferroics with arbitrary microstructure: The phase field approach*. Journal of Applied Physics, 2010. **108**: p. 023504.
59. Wu, P.P., et al., *Phase-field model of multiferroic composites: Domain structures of ferroelectric particles embedded in a ferromagnetic matrix*. Philosophical Magazine, 2010. **90**(1-4): p. 125-140.
60. Hu, J.-M., et al., *Phase-field simulation of strain-induced domain switching in magnetic thin films*. Applied Physics Letters, 2011. **98**(11).
61. Hu, J.-M., et al., *Phase-field simulation of electric-field-induced in-plane magnetic domain switching in magnetic/ferroelectric layered heterostructures*. Journal of Applied Physics, 2011. **109**(12).
62. Hellwege, K.-H., *Landolt Börnstein. Numerical Data and Functional Relationship in Science and Technology: New Series (Springer, Berlin, 1978)*, 1978, Springer.
63. Gray, D.E., *American institute of physics handbook 1982*: McGraw-Hill.

64. Nan, C.-W., *Physics of inhomogeneous inorganic materials*. Prog. Mater. Sci., 1993. **37**: p. 1-116.
65. Cahn, J. and S. Allen, *A microscopic theory for domain wall motion and its experimental verification in Fe-Al alloy domain growth kinetics*. Le Journal de Physique Colloques, 1977. **38**(C7): p. C7-51-C7-54.
66. Zhang, J. and L.-Q. Chen, *Phase-field microelasticity theory and micromagnetic simulations of domain structures in giant magnetostrictive materials*. Acta Materialia, 2005. **53**: p. 2845-2855.
67. Hu, S.Y. and L.-Q. Chen, *A phase-field model for evolving microstructures with strong elastic inhomogeneity*. Acta Materialia, 2001. **49**: p. 1879-1890.
68. Yu, P., et al., *An iterative-perturbation scheme for treating inhomogeneous elasticity in phase-field models*. Journal of Computational Physics, 2005. **208**: p. 34-50.
69. Khachaturyan, A.G., *Theory of Structural Transformation in Solids* 1983, New York: Wiley.
70. Zheng, H., et al., *Multiferroic BaTiO₃-CoFe₂O₄ Nanostructures*. Science, 2004. **303**: p. 661-663.
71. Press, W.H., et al., *Numerical Recipes in Fortran 77: The Art of Scientific Computing 2nd Editionn-Volume 1 of Fortran Numerical Recipes* 1992: Cambridge university press.
72. Liu, W. and X. Ren, *Large Piezoelectric Effect in Pb-Free Ceramics*. Physical Review Letters, 2009. **103**: p. 257602.
73. Yang, S., et al., *Large magnetostriction from morphotropic phase boundary in ferromagnets*. Physical Review Letters, 2010. **104**(19): p. 197201.
74. Wang, Y.U., D.Q. Tan, and J. Krahn, *Computational study of dielectric composites with core-shell filler particles*. Journal of Applied Physics, 2011. **110**: p. 044103.
75. Bhattacharyya, S., et al., *A phase-field model of stress effect on grain boundary migration*. Modelling and Simulation in Materials Science and Engineering, 2011. **19**(3).
76. Schilling, A., et al., *Scaling of domain periodicity with thickness measured in BaTiO₃ single crystal lamellae and comparison with other ferroics*. Physical Review B, 2006. **74**(2).
77. Catalan, G., et al., *Wall thickness dependence of the scaling law for ferroic stripe domains*. Journal of Physics-Condensed Matter, 2007. **19**(2).
78. Lahtinen, T.H.E., J.O. Tuomi, and S. van Dijken, *Pattern Transfer and Electric-Field-Induced Magnetic Domain Formation in Multiferroic Heterostructures*. Advanced materials, 2011. **23**(28): p. 3187-+.
79. Chopdekar, R.V., et al., *Spatially resolved strain-imprinted magnetic states in an artificial multiferroic*. Physical Review B, 2012. **86**(1).
80. Geprägs, S., et al., *Giant magnetoelastic effects in BaTiO₃-based extrinsic multiferroic hybrids*. Physical Review B, 2012. **86**: p. 134432.
81. Lahtinen, T.H.E., K.J.A. Franke, and S. van Dijken, *Electric-field control of magnetic domain wall motion and local magnetization reversal*. Scientific reports, 2012. **2**.
82. Lahtinen, T.H.E., et al., *Alternating domains with uniaxial and biaxial magnetic anisotropy in epitaxial Fe films on BaTiO₃*. Applied Physics Letters, 2012. **101**(26).
83. Geprägs, S., et al., *Converse magnetoelectric effects in Fe₃O₄/BaTiO₃ multiferroic hybrids*. Physical Review B, 2013. **88**: p. 054412.
84. Streubel, R., et al., *Strain-mediated elastic coupling in magnetoelectric nickel/barium-titanate heterostructures*. Physical Review B, 2013. **87**: p. 054410.
85. Franke, K.J.a., et al., *Size Dependence of Domain Pattern Transfer in Multiferroic Heterostructures*. Physical Review Letters, 2014. **112**: p. 017201.

86. Franke, K.J.A., T.H.E. Lahtinen, and S. van Dijken, *Field tuning of ferromagnetic domain walls on elastically coupled ferroelectric domain boundaries*. Physical Review B, 2012. **85**(9).
87. Chen, H.T., Y. Ni, and A.K. Soh, *Modeling of ferroelectric control of magnetic domain pattern and domain wall properties*. Journal of Applied Physics, 2013. **113**(13).
88. Kruglyak, V.V., S.O. Demokritov, and D. Grundler, *Magnonics*. Journal of Physics D-Applied Physics, 2010. **43**(26).
89. Hu, J.-M., et al., *High-density magnetoresistive random access memory operating at ultralow voltage at room temperature*. Nature Communications, 2011. **2**.
90. Hu, J.-M., et al., *Design of a voltage-controlled magnetic random access memory based on anisotropic magnetoresistance in a single magnetic layer*. Advanced materials (Deerfield Beach, Fla.), 2012. **24**: p. 2869-73.
91. Dean, J., et al., *Stress-based control of magnetic nanowire domain walls in artificial multiferroic systems*. Journal of Applied Physics, 2011. **109**(2).
92. Lei, N., et al., *Strain-controlled magnetic domain wall propagation in hybrid piezoelectric/ferromagnetic structures*. Nature Communications, 2013. **4**.
93. Hlinka, J., *Mobility of ferroelastic domain walls in barium titanate*. Ferroelectrics, 2007. **349**: p. 49-54.
94. Devonshire, A.F., *CIX. Theory of barium titanate—Part II*. Philosophical Magazine, 1951.
95. Berlincourt, D. and H. Jaffe, *Elastic and piezoelectric coefficients of single-crystal barium titanate*. Physical Review (US) Superseded in part by Phys. ..., 1958. **III**: p. 143-148.
96. Wang, J.J., et al., *Temperature-pressure phase diagram and ferroelectric properties of BaTiO₃ single crystal based on a modified Landau potential*. Journal of Applied Physics, 2010. **108**: p. 114105.
97. Hu, J.-M., et al., *Voltage-driven perpendicular magnetic domain switching in multiferroic nanoislands*. Journal of Applied Physics, 2013. **113**(19).
98. Kim, J.-Y., L. Yao, and S. van Dijken, *Coherent piezoelectric strain transfer to thick epitaxial ferromagnetic films with large lattice mismatch*. Journal of physics. Condensed matter : an Institute of Physics journal, 2013. **25**: p. 082205.
99. Lahtinen, T.H.E. and S. van Dijken, *Temperature control of local magnetic anisotropy in multiferroic CoFe/BaTiO₃*. Applied Physics Letters, 2013. **102**(11).
100. Hu, J.-M., et al., *Engineering domain structures in nanoscale magnetic thin films via strain*. Journal of Applied Physics, 2013. **114**: p. 164303.
101. Wang, X.-P., C.J. García-Cervera, and W. E, *A Gauss–Seidel Projection Method for Micromagnetics Simulations*. Journal of Computational Physics, 2001. **171**: p. 357-372.
102. Hall, R.C., *Magnetic Anisotropy and Magnetostriction of Ordered and Disordered Cobalt-Iron Alloys*. Journal of Applied Physics, 1960. **31**: p. S157.
103. Maruyama, T. and Y. Shiota, *Large voltage-induced magnetic anisotropy change in a few atomic layers of iron*. Nature nanotechnology, 2009. **4**: p. 158-161.
104. Hu, J.-M., et al., *Electric-field control of strain-mediated magnetoelectric random access memory*. Journal of Applied Physics, 2010. **107**(9).
105. Cochran, W., *Crystal stability and the theory of ferroelectricity*. Advances in Physics, 1960.
106. Scott, J., *Electrocaloric materials*. Annual Review of Materials Research, 2011. **41**: p. 229-240.
107. Moya, X., S. Kar-Narayan, and N.D. Mathur, *Caloric materials near ferroic phase transitions*. Nature materials, 2014. **13**(5): p. nmat3951.

108. Scott, J., *Applications of modern ferroelectrics*. Science, 2007. **315**(5814): p. 954-959.
109. Lines, M.E. and A.M. Glass, *Principles and applications of ferroelectrics and related materials* 1977: Oxford university press.
110. Neese, B., et al., *Large Electrocaloric Effect in Ferroelectric Polymers Near Room Temperature*. Science, 2008. **321**: p. 821-823.
111. Mischenko, a.S., et al., *Giant electrocaloric effect in thin-film $PbZr(0.95)Ti(0.05)O_3$* . Science (New York, N.Y.), 2006. **311**: p. 1270-1.
112. Chen, X.-z., et al., *Enhanced electrocaloric effect in poly (vinylidene fluoride-trifluoroethylene) -based terpolymer / copolymer blends*. Applied Physics Letters, 2012. **100**: p. 1-5.
113. Chen, X.-Z., et al., *A nanocomposite approach to tailor electrocaloric effect in ferroelectric polymer*. Polymer, 2013. **54**(20): p. 5299-5302.
114. Qian, X., et al., *Internal Biasing in Relaxor Ferroelectric Polymer to Enhance the Electrocaloric Effect*. Advanced Functional Materials, 2015. **25**: p. 5134-5139.
115. Geng, W., et al., *Giant Negative Electrocaloric Effect in Antiferroelectric La - Doped Pb ($ZrTi$) O_3 Thin Films Near Room Temperature*. Advanced materials, 2015. **27**(20): p. 3165-3169.
116. Ponomareva, I. and S. Lisenkov, *Bridging the macroscopic and atomistic descriptions of the electrocaloric effect*. Physical Review Letters, 2012. **108**(16): p. 167604.
117. Bai, Y., G.-P. Zheng, and S.-Q. Shi, *Abnormal electrocaloric effect of $Na_{0.5}Bi_{0.5}TiO_3$ - $BaTiO_3$ lead-free ferroelectric ceramics above room temperature*. Materials Research Bulletin, 2011. **46**(11): p. 1866-1869.
118. Qian, X., et al., *Anomalous negative electrocaloric effect in a relaxor/normal ferroelectric polymer blend with controlled nano- and meso-dipolar couplings*. Applied Physics Letters, 2016. **108**: p. 142902.
119. Hong, L., et al., *Minimum tetragonality in $PbTiO_3/BaTiO_3$ ferroelectric superlattices*. Journal of Applied Physics, 2013. **114**(14): p. 144103.
120. Xue, F., et al., *Phase field simulations of ferroelectrics domain structures in $PbZr_xTi_{1-x}O_3$ bilayers*. Acta Materialia, 2013. **61**(8): p. 2909-2918.
121. Daranciang, D., et al., *Ultrafast Photovoltaic Response in Ferroelectric Nanolayers*. Physical Review Letters, 2012. **108**(8): p. 087601.
122. Takahashi, K., N. Kida, and M. Tonouchi, *Terahertz radiation by an ultrafast spontaneous polarization modulation of multiferroic $BiFeO_3$ thin films*. Physical review letters, 2006. **96**(11): p. 117402.
123. Schmising, C.v.K., et al., *Coupled ultrafast lattice and polarization dynamics in ferroelectric nanolayers*. Physical review letters, 2007. **98**(25): p. 257601.
124. Jang, K.-J., et al., *Strong spin-lattice coupling in multiferroic hexagonal manganite $YMnO_3$ probed by ultrafast optical spectroscopy*. Applied Physics Letters, 2010. **97**(3): p. 031914.
125. Chen, L.Y., et al., *Ultrafast photoinduced mechanical strain in epitaxial $BiFeO_3$ thin films*. Applied Physics Letters, 2012. **101**(4): p. 041902.
126. Lejman, M., et al., *Giant ultrafast photo-induced shear strain in ferroelectric $BiFeO_3$* . Nature communications, 2014. **5**.
127. Sheu, Y.M., et al., *Using ultrashort optical pulses to couple ferroelectric and ferromagnetic order in an oxide heterostructure*. Nature Communications, 2014. **5**: p. 5832.
128. Grigoriev, A., et al., *Nanosecond Domain Wall Dynamics in Ferroelectric $PbTiO_3$ Thin Films*. Physical Review Letters, 2006. **96**(18): p. 187601.

129. Wen, H., et al., *Electronic Origin of Ultrafast Photoinduced Strain in BiFeO₃*. Physical Review Letters, 2013. **110**(3): p. 037601.
130. Akamatsu, H., et al., *Light-activated gigahertz ferroelectric domain dynamics*. Physical Review Letters, 2018. **120**(09): p. 096101.
131. Stoica, V., et al., *The ultrafast response of polar vortices under optical excitation*. unpublished 2017.
132. Qi, Y., et al., *Ultra-fast electric field control of giant electrocaloric effect in ferroelectrics*. arXiv, 2017.
133. Kundys, B., *Photostrictive materials*. Applied Physics Reviews, 2015. **2**(1): p. 011301.
134. Kittel, C., *Domain Boundary Motion in Ferroelectric Crystals and the Dielectric Constant at High Frequency*. Physical Review, 1951. **83**(2): p. 458-458.
135. Arlt, G. and N.A. Pertsev, *Force constant and effective mass of 90° domain walls in ferroelectric ceramics*. Journal of Applied Physics, 1991. **70**(4): p. 2283-2289.
136. Li, S., W. Cao, and L.E. Cross, *The extrinsic nature of nonlinear behavior observed in lead zirconate titanate ferroelectric ceramic*. Journal of Applied Physics, 1991. **69**(10): p. 7219-7224.
137. Pertsev, N.A. and G. Arlt, *Forced translational vibrations of 90° domain walls and the dielectric dispersion in ferroelectric ceramics*. Journal of Applied Physics, 1993. **74**(6): p. 4105-4112.
138. Arlt, G., U. Böttger, and S. Witte, *Emission of GHz shear waves by ferroelastic domain walls in ferroelectrics*. Applied Physics Letters, 1993. **63**(5): p. 602-604.
139. Sidorkin, A.S., *Translational vibrations of domain structure in ferroelectrics*. Journal of Applied Physics, 1998. **83**(7): p. 3762-3768.
140. Glinchuk, M.D., et al., *Static and dynamic properties of ferroelectric thin film multilayers*. arXiv:cond-mat, 2000.
141. Glinchuk, M.D., E.A. Eliseev, and V.A. Stephanovich, *Dynamical dielectric susceptibility of ferroelectric thin films and multilayers*. Physics of the Solid State, 2002. **44**(5): p. 953-963.
142. Wang, B., et al., *Dynamic process of domain switching in ferroelectric films*. Journal of Applied Physics, 2003. **94**(5): p. 3384-3389.
143. Wang, Y.-L., et al., *Simulation of the initial polarization curves and hysteresis loops for ferroelectric films by an extensive time-dependent Ginzburg–Landau model*. Journal of Materials Science, 2011. **46**(8): p. 2695-2699.
144. Caputo, J.G., et al., *High-frequency polarization switching of a thin ferroelectric film*. Physical Review B, 2010. **82**(9): p. 094113.
145. Fousek, J. and B. Burezina, *Relaxation of 90° Domain Walls of BaTiO₃ and Their Equation of Motion*. Journal of the Physical Society of Japan, 1964. **19**(6): p. 830-838.
146. McGilly, L. and J. Gregg, *Polarization closure in PbZr_{0.42}Ti_{0.58}O₃ nanodots*. Nano letters, 2011. **11**(10): p. 4490-4495.
147. Yadav, A., et al., *Observation of polar vortices in oxide superlattices*. Nature, 2016.
148. Hong, Z., et al., *Stability of Polar Vortex Lattice in Ferroelectric Superlattices*. Nano Letters, 2017. **17**: p. 2246-2252.
149. Jia, C.-L., et al., *Direct Observation of Continuous Electric Dipole Rotation in Flux-Closure Domains in Ferroelectric Pb(Zr,Ti)O₃*. Science, 2011. **331**(6023): p. 1420-1423.
150. Nelson, C.T., et al., *Spontaneous vortex nanodomain arrays at ferroelectric heterointerfaces*. Nano Lett, 2011. **11**(2): p. 828-34.
151. Tang, Y.L., et al., *Observation of a periodic array of flux-closure quadrants in strained ferroelectric PbTiO₃ films*. Science, 2015.

152. Ruff, E., et al., *Multiferroicity and skyrmions carrying electric polarization in GaV₄S₈*. Science advances, 2015. **1**(10): p. e1500916.
153. Nahas, Y., et al., *Discovery of stable skyrmionic state in ferroelectric nanocomposites*. Nature Communications, 2015. **6**.
154. Khachaturyan, A.G., *Theory of Structural Transformations in Solids* 1983, New York: John Wiley & Sons.
155. *Application Note 1217-1, Basics of measuring the dielectric properties of materials*. Hewlett Packard literature number 5091-3300E, 1992.
156. Li, Y., L. Cross, and L. Chen, *A phenomenological thermodynamic potential for Ba Ti O₃ single crystals*. Journal of Applied Physics, 2005. **98**(6): p. 064101.
157. Chen, L.Q. and J. Shen, *Applications of semi-implicit Fourier-spectral method to phase field equations*. Computer Physics Communications, 1998. **108**(2): p. 147-158.
158. Hu, S.Y. and L.Q. Chen, *A phase-field model for evolving microstructures with strong elastic inhomogeneity*. Acta Materialia, 2001. **49**(11): p. 1879-1890.
159. Wang, J.J., et al., *Phase transitions and domain structures of ferroelectric nanoparticles: Phase field model incorporating strong elastic and dielectric inhomogeneity*. Acta Materialia, 2013. **61**(20): p. 7591-7603.
160. Strauss, W. and L. Vazquez, *Numerical solution of a nonlinear Klein-Gordon equation*. Journal of Computational Physics, 1978. **28**(2): p. 271-278.
161. Donninger, R. and W. Schlag, *Numerical study of the blowup/global existence dichotomy for the focusing cubic nonlinear Klein-Gordon equation*. Nonlinearity, 2011. **24**(9): p. 2547.
162. Nakanishi, K. and W. Schlag, *Global dynamics above the ground state energy for the focusing nonlinear Klein-Gordon equation*. Journal of Differential Equations, 2011. **250**(5): p. 2299-2333.
163. Karma, A., D.A. Kessler, and H. Levine, *Phase-Field Model of Mode III Dynamic Fracture*. Physical Review Letters, 2001. **87**(4): p. 045501.
164. Spatschek, R., E. Brener, and A. Karma, *Phase field modeling of crack propagation*. Philosophical Magazine, 2011. **91**(1): p. 75-95.
165. Henry, H. and H. Levine, *Dynamic Instabilities of Fracture under Biaxial Strain Using a Phase Field Model*. Physical Review Letters, 2004. **93**(10): p. 105504.
166. Bouchbinder, E., J. Fineberg, and M. Marder, *Dynamics of Simple Cracks*. Annual Review of Condensed Matter Physics, 2010. **1**(1): p. 371-395.
167. Hughes, T., T. Caughey, and W. Liu, *Finite-element methods for nonlinear elastodynamics which conserve energy*. Journal of Applied Mechanics, 1978. **45**(2): p. 366-370.
168. Yang, Z.J. and A.J. Deeks, *A frequency-domain approach for modelling transient elastodynamics using scaled boundary finite element method*. Computational Mechanics, 2007. **40**(4): p. 725-738.
169. Geubelle, P.H. and J.R. Rice, *A spectral method for three-dimensional elastodynamic fracture problems*. Journal of the Mechanics and Physics of Solids, 1995. **43**(11): p. 1791-1824.
170. Rubio-Marcos, F., et al., *Ferroelectric domain wall motion induced by polarized light*. Nature Communications, 2015. **6**.
171. Känzig, W., *Space charge layer near the surface of a ferroelectric*. Physical Review, 1955. **98**(2): p. 549.
172. Fatuzzo, E. and W.J. Merz, *Surface layer in BaTiO₃ single crystals*. Journal of Applied Physics, 1961. **32**(9): p. 1685-1687.

173. Motegi, H., *X-Ray Study of the Surface Layer on Barium Titanate Single Crystal*. Journal of the Physical Society of Japan, 1972. **32**(1): p. 202-209.
174. Merz, W.J., *Switching time in ferroelectric BaTiO₃ and its dependence on crystal thickness*. Journal of Applied Physics, 1956. **27**(8): p. 938-943.
175. Klicker, K., J. Biggers, and R. Newnham, *Composites of PZT and epoxy for hydrostatic transducer applications*. Journal of the American Ceramic Society, 1981. **64**(1): p. 5-9.
176. Smith, W.A. and B.A. Auld, *Modeling 1-3 composite piezoelectrics: thickness-mode oscillations*. IEEE transactions on ultrasonics, ferroelectrics, and frequency control, 1991. **38**(1): p. 40-47.
177. Temnov, V.V., et al., *Femtosecond nonlinear ultrasonics in gold probed with ultrashort surface plasmons*. Nature Communications, 2013. **4**: p. 1468.
178. Kovalenko, O., T. Pezeril, and V.V. Temnov, *New Concept for Magnetization Switching by Ultrafast Acoustic Pulses*. Physical Review Letters, 2013. **110**(26): p. 266602.
179. Thevenard, L., et al., *Irreversible magnetization switching using surface acoustic waves*. Physical Review B, 2013. **87**(14): p. 144402.
180. Mott, N., *Metal-insulator transition*. Reviews of Modern Physics, 1968. **40**(4): p. 677.
181. Imada, M., A. Fujimori, and Y. Tokura, *Metal-insulator transitions*. Reviews of Modern Physics, 1998. **70**(4): p. 1039.
182. Yang, Z., C. Ko, and S. Ramanathan, *Oxide Electronics Utilizing Ultrafast Metal-Insulator Transitions*. Annual Review of Materials Research, 2011. **41**(1): p. 337-367.

VITA

Tiannan Yang

Tiannan Yang was born in Zhengzhou, China on September 7th, 1989. He got his B.E. in Materials Science and Engineering at Tsinghua University, China, in 2011. He was enrolled in the Ph.D. program in the Department of Materials Science and Engineering at Penn State in 2011. He received the Graduate Excellence in Materials Science Award by the American Ceramic Society in 2017. He authored and co-authored 26 papers at Penn State. Following is part of the publication list.

1. **T. N. Yang**, J.-M. Hu, C.-W. Nan, and L.-Q. Chen, “Predicting effective magnetoelectric response in magnetic-ferroelectric composites via phase-field modeling”, *Appl. Phys. Lett.* 104 (2014) 052904
2. **T. N. Yang**, J.-M. Hu, C.-W. Nan, and L.-Q. Chen, “On the elastically coupled magnetic and ferroelectric domains: A phase-field model”, *Appl. Phys. Lett.* 104 (2014) 202402
3. J.-M. Hu, **T. N. Yang (co-first-author)**, J. Wang, H. Huang, J. Zhang, L.-Q. Chen, and C.-W. Nan, “Purely electric-field-driven perpendicular magnetization reversal”, *Nano Lett.* 15 (2015) 616-622
4. X. Qian, H.-J. Ye, **T. N. Yang**, W.-Z. Shao, L. Zhen, E. Furman, L.-Q. Chen, and Q. Zhang, “Internal biasing in relaxor ferroelectric polymer to enhance the electrocaloric effect”, *Adv. Funct. Mater.* 25 (2015) 5134-5139
5. G. Zhang, X. Zhang, **T. N. Yang**, Q. Li, L.-Q. Chen, S. Jiang, and Q. Wang, “Colossal room-temperature electrocaloric effect in ferroelectric polymer nanocomposites using nanostructured barium strontium titanates”, *ACS Nano* 9 (2015) 7164-7174
6. J.-M. Hu, **T. N. Yang (co-first-author)**, K. Momeni, X. Cheng, L. Chen, S. Lei, S. Zhang, S. Trolier-McKinstry, V. Gopalan, G. Carman, C.-W. Nan, and L.-Q. Chen, “Fast magnetic domain-wall motion in a ring-shaped nanowire driven by a voltage”, *Nano Lett.* 16 (2016) 2341-2348
7. Q. Li, F. Liu, **T. N. Yang**, M. R. Gadinski, G. Zhang, L.-Q. Chen, and Q. Wang, “Sandwich-structured polymer nanocomposites with high energy density and great charge-discharge efficiency at elevated temperatures”, *Proc. Natl. Acad. Sci. U.S.A.* 113 (2016) 9995-10000
8. T. Amrillah, Y. Bitla, K. Shin, **T. N. Yang**, Y. H. Hsieh, Y. Y. Chiou, H. J. Liu, T. H. Do, D. Su, Y. C. Chen, S. U. Jen, L.-Q. Chen, K. H. Kim, J. Y. Juang, and Y. H. Chu, “Flexible multiferroic bulk heterojunction with giant magnetoelectric coupling via van der Waals epitaxy”, *ACS Nano*, 11 (2017) 6122–6130